

THE VOLCANOLOGY, GEOCHEMISTRY AND METALLOGENIC
POTENTIAL OF THE GOREN VOLCANO-SEDIMENTARY BELT,
NORTHEAST BURKINA FASO,
WEST AFRICA

A Dissertation submitted to the Faculty of Science, University of Witwatersrand in the
fulfilment of the requirements for the degree of Master of Science



Luke Fred Horst Peters
Person Number 0704730N

Johannesburg
December 2013

DECLARATION

I declare that this Dissertation is my own, unaided work. It is being submitted for the Degree of Master of Science at the University of Witwatersrand, Johannesburg. It has not been submitted before for any degree or examination at any other University.

.....
14th day of February 2014 in Johannesburg

ABSTRACT

The Palaeoproterozoic southern Goren volcano-sedimentary belt of northeast Burkina Faso represents a sequence/package of rocks formed in a back-arc basin environment. Evidence is based on a conformable sequence of basalts that have geochemical affinities of normal mid-oceanic ridge style basalts (N-MORB) as well as arc-related magmas. Tholeiitic compositions, determined by major and trace element geochemistry, are exclusive to the study area, which is unique to northeast Burkina Faso. Flat, chondrite-normalised REE patterns suggest dominantly N-MORB compositions, with the occasional elevated Th and Al₂O₃ values, suggestive of arc basalts. Depleted chondrite-normalised concentrations of phosphorus (0.5-0.03 times lower than chondrite) and Ti (1-5 times chondrite) as well as anomalous concentrations of N-MORB-normalised Ta (80-120 times greater) are characteristic of the tholeiitic basalts of the Goren belt.

The volcanic rocks are intercalated with a succession of volcanogenic manganese deposits, siltstone, volcaniclastite, volcanogenic greywacke and a discrete pyroclastic breccia deposit composed of lapilli- to bomb-sized volcanic debris, indicative of bimodal volcanism. The volcanic facies were established through field and petrographic interpretations. The subaqueous facies architecture consists of proximal, coherent and autoclastic basaltic flow units containing porphyritic, aphyric, amygdaloidal and hyaloclastic textures as well as pillowd, jointed and flow-banded basaltic lithofacies. Proximal to distal volcanogenic manganese deposits intercalated with basalt flows indicate a syn-volcanic genesis. A discrete pyroclastic interbed (~300 m thick) within a volcanogenic, marginal marine to offshore greywacke succession occupies a distal facies relative to the volcanic source and indicates a bimodal source of volcanism, i.e., mafic and intermediate.

Volcanogenic manganese deposits are characterized by quartz-ankerite stockwork breccia, a braunite-ilmenite-magnetite-chalcopyrite-pyrite-(gold) mineral assemblage and increased Ba concentrations, indicating syn-volcanic seafloor-related hydrothermal activity. The Goren volcano-sedimentary belt presents potential for economic mineralisation in volcanogenic primary manganese and base metal deposits.

ACKNOWLEDGMENTS

First and foremost, I would like to thank Prof. K.A.A Hein for supervising and overseeing this project, for her excellent knowledge of West Africa, countless debates on subject matter and always making the work exciting. Huge thanks are owed to Prof. J. McPhie of the ARC Centre of Excellence in Ore Deposits at the University of Tasmania for her co-supervision, expertise in the field of volcanology and providing me with the tools I needed to complete this research. A special thanks to Mr Asinne Tshibubudze for his guidance, patience and time when approached with obscure theories and questions.

I would like to thank the technical staff at the Earth Lab at the University of the Witwatersrand Johannesburg for preparing the thin sections and running geochemical analyses, in particular Joe Aphane, Jacqueline Pienaar who conducted the XRF analyses, Marlin Patchappa who carried out the ICP-MS analyses, and Musa Cebekhulu. Sample preparation and analyses were overseen by Prof. Allan Wilson.

Dr. Lenka Baratoux allowed me to use published data from her field area.

I owe gratitude to my colleagues in Burkina Faso and South Africa:-

Burkina Faso: Mr Alassane Traore and Salif for providing transportation during fieldwork.

The staff at Hotel Kaziende for making field work as comfortable as possible.

Mr Koné for acting as my liaison/translator in Burkina Faso and for organising the safe transportation of rock samples to South Africa.

South Africa: Prof. Lew Ashwal, Prof. Grant Cawthorn, Dr. Zubair Jinnah, Dr. Musa Manzi, Dr. Grant Bybee, Dr Lorenzo Milani, Dr. Kalin Naydenov, Dr. Jeremie Lehmann for all your insight and advice.

Russell Johnson, Grace Coetzee, William Rankin, Cameron Penn-Clarke, Trishya Owen-Smith, Sello Mashabela and Natalie Deseta for all the support and advice over the course of this project.

Most importantly, I wish to thank WAXI (West African Exploration Initiative), the AMIRA and its sponsors, without whom this research would not have been possible.

I wish to gratefully acknowledge AMIRA International and the industry sponsors, including AusAid and the ARC Linkage Project LP110100667, for their support of the WAXI Project (P934A). I am also appreciative of the contribution of the various Geological Surveys/Department of Mines in West Africa as sponsors in-kind of WAXI. Finally, I wish to recognize our WAXI research colleagues from the various Institutions from around the world.



I would like to thank the National Research Foundation for providing funding for this research in 2012.



TABLE OF CONTENTS

<i>Declaration</i>	2
<i>Abstract</i>	3
<i>Acknowledgements</i>	4
<i>Table of Contents</i>	6
<i>List of Figures</i>	8
<i>List of Tables</i>	15

1.0. INTRODUCTION

1.1. Preamble.....	16
1.2. Location and physiography.....	19
1.3. Project aims.....	19
1.4. Conventions and acronyms.....	20
1.5. Thesis Organisation.....	20
1.6. Limitations of this study.....	21

2.0 REVIEW OF WEST AFRICAN GEOLOGY

2.1. Stratigraphy.....	22
2.2. Granitoid emplacement.....	23
2.3. Metamorphism and deformation.....	23
2.4. Metallogenesis.....	24
2.5. The Goren volcano-sedimentary belt.....	25

3.0 METHODOLOGY

3.1. Field Methods.....	27
3.2. Laboratory Methods.....	30
3.2.1. Summary of XRF analyses.....	31
3.2.2. Summary of ICP-MS analyses.....	32
3.3. Petrography.....	33
3.4. Maps and Images.....	33

4.0 LITHOLOGIES OF THE GOREN BELT

4.1. Introduction.....	35
4.2. Basaltic rocks.....	35
4.3. Meta-sedimentary rocks.....	41
4.3.1. Siltstone	41
4.3.2. Volcaniclastite.....	41
4.3.3. Greywacke	41
4.3.4. Pyroclastic breccia	41
4.3.5. Mn-Fe-rich carbonaceous chemical sedimentary rocks.....	43
4.4. Intrusions.....	43
4.4.1. Mafic dykes and sills.....	43
4.4.2. Aplite dykes	44
4.4.3. Loudo Granodiorite.....	44

5.0 PETROGRAPHIC OBSERVATIONS OF SELECTED SAMPLES FROM THE GOREN BELT

5.1. Basaltic rocks.....	45
5.2. Meta-sedimentary rocks.....	48
5.2.1. Volcanogenic greywacke.....	48
5.2.2. Pyroclastic agglomerate.....	49
5.2.3. Mn-Fe-rich carbonaceous chemical sedimentary rocks.....	50
5.3. Intrusions.....	50
5.3.1. Mafic dykes and sills.....	50
5.3.2. Aplite dykes.....	52

6.0 GEOCHEMICAL ANALYSIS OF THE GOREN BELT

6.1. Geochemistry of the volcanic rocks	54
6.1.1. Major element geochemistry.....	54
6.1.2. Trace element geochemistry.....	59
6.2. Geochemistry of the Mn-Fe-rich chemical sedimentary rocks.....	70

7.0 INTERPRETATIONS AND DISCUSSION

7.1. Depositional Environment and Interpretations.....	72
7.1.1. Volcanic rocks of the south Goren belt	72
7.1.2. Sedimentary rocks of the south Goren belt.....	76
7.2. Tectonic setting of the Goren belt and geochemical interpretations.....	77
7.3. The Goren belt in a regional context.....	81
7.4. The Goren belt and the West African craton in a global context.....	82

8.0. CONCLUSIONS	85
-------------------------	----

REFERENCES.....	87
APPENDIX A.....	98
APPENDIX B.....	116
APPENDIX C.....	120
APPENDIX D.....	139

LIST OF FIGURES

Figure 1.1. Volcano-sedimentary belts of southeast and northeast Burkina Faso and northwestern Ghana. Volcano-sedimentary belts from the northeast Burkina Faso are modified after Hein et al. (2004); the study area is located in the Goren belt and expanded in Inset A. Location of Tiebélé dome of southern Burkina Faso with Zn anomalies as defined by Ilboudo (2010) is presented in Inset B. The Perkoa and Gaoua deposits are located in the Boromo belt in Burkina Faso, southwest of Ouagadougou. The Essakane, Falagountou, Taparko and Inata goldfields are represented in north-northeast of Burkina Faso. The Billiata and Tambão Mn deposits and the Tin Edia Mn-Fe-V deposit are located on the western margin of the Oudalan-Gorouol belt. The Barsalogo diamond fields are located north of the Goren belt.

Figure 2.1. The Goren volcano-sedimentary belt is presented showing the locations of Kaya, Mané, Guilla, Korsimoro, Sirgui artisanal mine and Tangapella hill. Northwest and northeast trending shears and thrusts are represented as well as WNW trending shears of the Wabo-Tampelse Event. A variety of granodiorite intrusions are shown including the Pissila batholith and Loudo granodiorite that crop out to the east of the Goren belt. The Silimidougou megacrystic granite crops out to the west of the Goren belt. This image is modified after Hein et al. (2004) and Hein (2010).

Figure 3.1. Geological map of the southern Goren belt presenting rock types, major structures, infrastructure and geochemical sample points.

Figure 3.2. Volcanic facies map of the southern Goren belt representing the location of various facies and major structures. Two schematic section lines, A-B and C-D, are drawn.

Figure 4.1. Photograph of plagioclase crystals in porphyritic basalt (rare) demonstrating preferential weathering. Crystals measure 1.5 cm in length.

Figure 4.2. (a) Photograph of pillows in a hyaloclastic breccia (Pi = Pillow; Hy = Hyaloclastite) where the hyaloclastic breccia is observed in the inter-pillow domains (Sample G12-02-110, UTM 30P 694964; 1440271). Pillows are 20-30 cm with chill margins less than 1 cm thick. **(b)** Photograph of amygdaloidal pillowed basalt with amygdales concentrated on the pillow margins compared to the centre of the pillow (Sample G12-008, UTM 30P 694317; 1443450). The amygdales are elongate toward the margin of the pillow and measure 2 cm in length. **(c)** Photograph of hyaloclastic pillow basalt displaying an ~10 cm pillow with well-defined amygdale accumulation on the margin of the pillow, with hyaloclastic breccia enclosing it.

Figure 4.3. (a) Photograph of pillowed basalt that has undergone flattening (Station point G12-02-083; UTM 30P 703920; 1446075). Re-entrants and rinds are still visible. Stratigraphic facing is to the north. **(b)** Photograph of a basalt with vertical fractures that are interpreted to be the result of cooling (Station point G12-02-004; UTM 30P 703585; 1426248). **(c)** Photograph of tortoise

shell jointing in basalt that is interpreted to be the result of cooling (Sample G12-02-095; UTM 30P 695421; 1443258). Polygonal jointing is fairly well-defined.

Figure 4.4. (a) Photograph of flow banding in a basalt (Station point G12-02-098; UTM 30P 693240; 1443462). The flow bands were identified by light and dark banding that is interpreted to be caused by differential mineral accumulation. (b, c) Photographs of hyaloclastic basalt interstitial to loosely packed pillow basalts (Station point G12-02-099; UTM 30P 696917; 1441719). Various shapes result from fragmentation of the basalt and stand proud due to differential weathering.

Figure 4.5. (a) Photographs of siltstone showing well-defined Fe-rich and Fe-poor laminations (G12-02014; UTM 30P 711294; 1431532). Bed thicknesses range from 1 mm to 5 cm. Micro-faults crosscut the siltstone. The siltstone exhibits well developed cleavage planes, particularly prominent in the Fe-rich layers. (b) Photograph of a fining upward greywacke succession with thin monomictic conglomerate interbeds making up the basal unit of Bouma sequences (G12-02-119; UTM 30P 708845; 1431001). The basal layer of Unit 2 is composed of coarse-grained gritstone compared to the conglomerate layer of Unit 1. The depositional environment is interpreted as a marginal marine-offshore setting. (c) Photograph of a poorly sorted volcanogenic greywacke deposit with angular fragments. The greywacke is composed of rounded chert clasts and is matrix-supported (Station point G12-02-010; UTM 30P 696828; 1443986). (d) Photograph of a polyolithic, poorly sorted, massive volcanogenic greywacke (Sample G12-02-093, UTM 30P 709616; 1429270). The angular fragments measure up to 3 cm in size.

Figure 4.6. (a-b) Photograph of a polyolithic, non-bedded, lapilli-bomb dominated pyroclastic breccia deposit with angular to sub-angular crystals of ilmenite, magnetite, plagioclase, quartz and hornblende, ranging in size from 2 mm to 7 cm (Sample G12-02-126, UTM 30P 709365; 1424791).

Figure 5.1. (a) Photomicrograph of basalt exhibiting subhedral plagioclase microlites, a largely replaced groundmass, and an amygdale containing chlorite and subhedral zeolite crystals (Sample G12-009; plane polarized light). (b) Photomicrograph of a microlitic basalt containing < 1.5 mm euhedral plagioclase microlites, anhedral ilmenite (opaque), interstitial quartz and a high proportion of chlorite (Sample G12-009; UTM 30P 693302; 1444147; plane polarized light). (c) Photomicrograph of a porphyritic basalt with 0.5-1.0 mm partly altered plagioclase crystals. The groundmass is composed of chlorite and epidote, which is interpreted to be the result of plagioclase and clinopyroxene microlite alteration (G12-018; UTM 30P 695652; 1466804). (d) Photomicrograph of an amygdale in amygdaloidal basalt. The amygdale is interpreted to form due to passive degassing of the basaltic liquid and these are filled with various minerals at a later stage. In this case, the infill is with epidote and zeolite group minerals. The amygdale exhibits a sub-rounded shape in which the zeolite crystals radiate

inward from the amygdale boundary toward a fine-grained aggregate of epidote (Sample G12-02-057; UTM 30P 699990; 1435556; cross polarized light).

Figure 5.2. (a) Photomicrograph of a medium grained, amygdaloidal basalt that displays a partly chloritised amygdale filled with devitrified glass. The amygdale is rimmed by zeolites. Smaller amygdales in the image are also filled with chlorite and zeolite (G12-02-096; plane polarized light. (b, c) Photomicrographs of hyaloclastic basalt (1:1 scale) that is altered to chlorite-actinolite. The hyaloclastite is brecciated in a jigsaw of basalt fragments. The breccia matrix is composed of chloritised volcanic glass. Late stage epidote veins crosscut the hyaloclastic breccia (G12-02-099; UTM 30P 696917; 1441719 and G12-02-057; UTM 30P 699990; 1435556; plane polarized light).

Figure 5.3. (a) Photomicrograph of a medium-grained basalt composed of metamorphic mineralogy. The image exhibits well-formed, < 3.5 mm epidote crystals surrounded by a fine-grained epidote and chlorite (Sample G12-02-096; UTM 30P 694686; 1443104; cross polarized light). (b) Photomicrograph of a basalt that displays plagioclase with an overprint of epidote and chlorite. Plagioclase is partly replaced by chlorite, but retains its lath-like shape, is randomly oriented and exhibits albite twinning (Sample G12-02-095; UTM 30P 695421; 1443258). (c) Photomicrograph of basalt that is crosscut by a quartz-calcite vein. The basalt is altered to chlorite-epidote but retains minor primary plagioclase microlites. The vein crosscuts both primary and secondary mineralogies indicating it formed syn- or post-alteration. (Sample G12-02-095; cross polarized light). (d) Photomicrograph of pyrite and chalcopyrite in a vein that crosscuts basalt (Sample G12-02-096; UTM 30P 694686; 1443104; Reflected-light). The texture indicates that sulphide mineralisation is synchronous to, or postdates emplacement of the basalt sequence.

Figure 5.4. (a) Photomicrographs of a coarse-grained, poorly sorted, chlorite-rich volcanogenic greywacke. The sample is composed of quartz, plagioclase (> 2mm), lithic chert clasts, and biotite (Sample G12-007; 696828; 1443986). (b, c) Photomicrographs of pyroclastic breccia containing euhedral, coarse-grained (> 1mm) plagioclase, chert, quartz and fine-grained (< 0.5mm) epidote replacing clinopyroxene and hornblende. The matrix is interpreted to be composed of ash-lapilli sized fragments that are altered to epidote and chlorite (Sample G12-02-126; UTM 30P 709365; 1424791, cross polarized light). (d) Photomicrograph of pyroclastic breccia that is composed of euhedral, coarse-grained (> 1 mm), zoned, volcanic hornblende, with well-defined cleavage, and 1> 2 mm sub-rounded chert clasts and sub-angular quartz grains (Sample G12-02-126; UTM 30P 709365; 1424791, plane polarized light).

Figure 5.5. (a) Photomicrograph of tabular, colloform and brecciated braunite from a Mn-Fe-rich unit (Sample G12-004; UTM 30P 702744; 1446079, reflected light). The three textures of braunite suggest different growth phases. Late stage fractures cross-cut brecciated braunite and terminate against the tabular braunite indicating that tabular braunite developed after the colloform texture

braunite. (b) Photomicrograph of a Mn-Fe-rich, carbonaceous unit which is crosscut by anastomosing hematite veins (Sample G12-02-080; UTM 30P 703512; 1444037, reflected light). (c) Photomicrograph of a Mn-Fe-rich unit that are crosscut by ilmenite-bearing veins. The ilmenite, in this case, is interpreted as a secondary phase because it is vein-hosted in the rocks (Sample G12-02-35; UTM 30P 707346; 1425026, reflected light). (d) Photomicrograph of a Mn-Fe carbonaceous unit that is crosscut by stockwork quartz ± ankerite veins. The rock is altered to hematite, ilmenite, magnetite and secondary quartz (sample G12-017; UTM 30P 677996; 1466647, plane polarized light).

Figure 5.6. (a) Photomicrograph of a chalcostibite in dolerite. Chalcostibite forms large, disseminated crystals. The chalcostibite crystals are soft (shown by scratches), contain triangular pits, and have a moderate reflection (Sample G12-02-122; UTM 30P 709363; 1425384, reflected light). (b) Photomicrograph of an aplite dyke, which is composed of medium to coarse microcline and quartz, with subordinate muscovite. The mineralogy is unaltered (Sample G12-02-114; UTM 30P 711540; 1432977, cross polarized light).

Figure 6.1. (a) Streckeisen classification diagram for volcanic rocks plots the rocks from the GB as basalts, basalt-andesite to dacite in composition. The samples that indicate dacitic composition contain increased secondary silica, interpreted to be a result of silicification. (b) Nb/Y versus $Zr/TiO_2 \times 0.0001$ diagram (after Winchester and Floyd, 1976). The GB volcanic rocks generally plot in the basalt field. (c) Le Maitre's classification for volcanic rocks. The GB rocks plot within the basalt, basaltic-andesite and andesite fields. Samples from the Boromo-Houndé belts are distributed throughout the basalt, basaltic-andesite and andesite fields. The Tiebélé samples have a smaller SiO_2 range but some samples contain increased alkali concentrations and plot as trachyandesite and tephrite. The Oudalan-Gorouol belt samples plot between basalt and basaltic-andesite. (d) SiO_2 versus K_2O (wt%) demonstrates that the GB volcanic rocks plot within the Low-K series for the most part. One sample plots in the Medium-K series with a K_2O value of ~1 wt%. Samples from the Boromo-Houndé belts plot within the Low-K series as well as the calc-alkaline fields (Medium-K, High-K series and the Shoshonite series. The Tiebélé samples vary between the different fields. (e) The AFM diagram plots samples from various locations. The GB volcanic rocks plot in the tholeiitic phase whereas the Boromo-Houndé samples are split between tholeiitic and calc-alkaline compositions which agrees with classifications made by Baratoux et al. (2011). The Tiebélé samples are also distributed between calc-alkaline and tholeiitic compositions.

Figure 6.2. Harker diagrams exhibiting crystallization trends of major elements for the GB volcanic rocks. Red dots=more deformed samples; blue dots=less deformed samples (a) The $MgO-NiO$ plot resolved a trend line in which NiO decreased with MgO . This suggests the crystallization of clinopyroxene occurred, which consumed Ni thus removing it from the melt to the crystal structure. The slight shallowing of the $NiO-MgO$ trend line is due to the closure of

clinopyroxene crystallization (**b**) The MgO-Cr₂O₃ plot resolved a similar trend in which Cr₂O₃ decreased in wt% as MgO decreased. The decrease of Cr₂O₃ was credited to the crystallization of spinel and clinopyroxene. The trend shallowed, indicating less Cr was used up, caused by a decrease or halt in spinel and clinopyroxene crystallization (**c, d**) The MgO-CaO and MgO-Al₂O₃ plots exhibited directly proportional trends. As MgO decreased, it was interpreted that CaO and Al₂O₃ decrease as plagioclase crystallised (**e, f**) MgO-SiO₂ and MgO-TiO₂ plots resolved similar trends. At high MgO values, there are low concentrations of SiO₂ and TiO₂. As the melt began to evolve and fractionate, the concentration of SiO₂ and TiO₂ increased. TiO₂ will crystallise and form oxide minerals such as rutile and ilmenite (**g**) The MgO-Na₂O plot displayed the Na₂O concentration increasing slowly as MgO concentration remained high. As the MgO concentration began to decrease, the Na₂O concentration rapidly increased. This can be explained by the crystallization of the Na-rich end-members of plagioclase, towards the end of crystallization (**h**) The MgO-P₂O₅ plot also resolved an increasing trend as MgO decreased, suggesting phosphorus did not crystallise (**i**) The MgO-FeO plot resolved an increasing FeO trend. It would be expected at some point in the fractionation process for Fe to partition into Fe-oxide minerals, explaining the decrease in FeO concentrations. (**j**) K₂O versus MgO shows a poor correlation.

Figure 6.3 (**a**) Chondrite-normalised multi-element diagram comparing the tholeiitic basalts from the GB, Boromo-Houndé belts and the Tiebélé region. The sample suites contain similar trace element affinities indicated by similar patterns. Rb exhibits a negative anomaly ranging from 0.1 to 5 times the chondritic value. Similarly, Ti displays a negative anomaly ranging from 0.5 to times that of chondrite. (**b**) Chondrite-normalised multi-element diagram comparing the tholeiitic basalts of the GB with the calc-alkaline volcanic rocks of the Boromo-Houndé belts. The Boromo-Houndé data present enrichment in Rb, Ba, Th, U, La, Ce, Pr, Sr and Nd relative to the GB samples. This indicates that calc-alkaline rocks are more enriched in LIL elements relative to tholeiitic compositions. Both sample suites have similar concentrations for the remaining elements.

Figure 6.4. (**a**) Chondrite-normalised multi-element diagram comparing the tholeiitic basalts from the GB, Boromo-Houndé belts and the Tiebélé region. Similar patterns indicate similar trace element properties for the tholeiitic basalt samples from three regions. On this element array, Rb and Ti display negative anomalies. P exhibits a large, negative anomaly (~twice the size of Ti) with values ranging from ~0.03-0.5 that of chondrite. (**b**) Chondrite-normalised multi-element diagram comparing the tholeiitic basalts from the GB with the calc-alkaline volcanic rocks from the Boromo-Houndé belts. An enrichment in the calc-alkaline rocks is presented for Ba to P relative to the GB samples. Ba, Rb and Th show a relative enrichment of one order of magnitude indicating significantly different trace element chemistry for the sample suites. Although the sample suites are compositionally different, the P anomaly is present throughout

both plots, albeit the anomaly is smaller for the calc-alkaline volcanic rocks. (c) Primitive mantle normalised multi-element diagram with a chemical array used in McCuaig et al. (1994) that presents negative P and Ti anomalies. These anomalies are interpreted to form because of phosphorus and titanium retention in silicate minerals in the magma source region.

Figure 6.5. (a) N-MORB normalised multi-element (after Tarney et al., 1981) diagram presenting the data from the GB. The elemental array increases in incompatibility from left to right. Ta and P are removed from the x-axis. The data represents a similarity between the GB rocks and the average N-type MORB concentrations. A range in concentrations exists but they do not deviate significantly from the N-MORB values. Rb and Cr have the widest range of concentrations (~1-20 and ~1-0.05 the value of N-MORB) and Y portrays a negative anomaly, consistent with each sample. (b) N-MORB normalised multi-element diagram (after Tarney et al., 1981) comparing the GB tholeiitic basalts to the Boromo-Houndé calc-alkaline volcanic rocks. Ta and P are added to the x-axis. The GB tholeiitic basalts present large Ta and P anomalies, positive and negative, respectively. The calc-alkaline rocks present negative Ti and P anomalies.

Figure 6.6. (a) Chondrite-normalised REE patterns for the GB tholeiitic basalts. The data presents a flat overall pattern from LREE to HREE and are considered typical of tholeiitic MORB. The average range in concentrations for LREE is from ~8-25 times the chondritic value, whereas the HREE range between ~9 and 20 times chondrite. Some samples present slight depletions, while others present slight enrichments from LREE to HREE. (b) Chondrite-normalised REE diagram comparing the GB, Boromo-Houndé and Tiebélé tholeiitic basalts. The REE patterns of each sample suite present parallel patterns of similar magnitudes. The Tiebélé samples present a slightly decreasing trend from LREE to HREE. (c) Chondrite-normalised REE diagram comparing tholeiitic basalts from the GB to the Boromo-Houndé calc-alkaline volcanic rocks. The calc-alkaline rocks present enrichment in LREE relative to HREE compared to the tholeiitic compositions, resulting in a decreasing trend. Boromo-Houndé calc-alkaline volcanic rocks have La values range from ~30-80 time chondrite and Lu between ~6 and 12 times chondrite. Negative Eu anomalies are present.

Figure 6.7. (a) Ternary discrimination diagram ($Ti/100$, Zr and $Yx3$). The data is clustered within field B and A, indicating most of the GB volcanic rocks are MORB, island arc tholeiite or calc-alkaline basalt. Two outliers, although clustered with the data, do not plot in a tectonic field. (b) Binary discrimination diagram that plots Zr versus Ti (ppm). A good correlation between the data is presented. The GB volcanic rocks plot in fields B and D, representing MORB, calc-alkali basalts and island arc tholeiites; therefore no definitive tectonic setting can be established from this graph. (c) A ternary discrimination diagram ($2Nb$, Y and $Zr/4$) that follows from Figure 6.7 b. The GB samples plot well within field D. Field D categorizes the data either as N-type MORB or volcanic-arc basalts. The data represents a linear trend, becoming more enriched in Zr and Nb or Y .

Figure 7.1. Schematic diagram depicting the lateral volcanic facies variation of the Goren volcano-sedimentary belt at the time of deposition. Volcanic lithofacies represented are pillow and massive basalts.

Figure 7.2. Schematic diagram depicting Ta, Ti and Nb signatures relative to MORB values in a volcanic-arc environment. These values present the similarities between back-arc and intra-arc terranes as well as the differences between retro-arc and volcanic arc trace element geochemistry. The dotted line indicates the concentrations that are expected across the tectonic setting based on literature and the red line represents observed concentrations using data from the Goren belt and the Boromo-Houndé belts (interpreted back-arc/intra-arc and arc environments respectively).

Figure 7.3. Schematic diagram illustrating the tectonic setting, depositional environment and facies distribution for the Goren belt.

LIST OF TABLES

Table 3.1. Major element calibration instrument parameters.

Table 6.1. Ranges and averages of important trace elements that can help classify the tectonic domain according to geochemical differences.

1. INTRODUCTION

1.1. Preamble

Volcano-sedimentary belts make up a large part of the stratigraphy of the Palaeoproterozoic Baoulé-Mossi domain (West Africa) in northeast Burkina Faso (Figure 1.1). The belts are composed of dominantly lower to middle greenschist metamorphosed volcanic, pyroclastic and sedimentary rocks with extensive units of basalt-andesite, dacite and less substantial amounts of pyroclastite (Milési et al., 1989, 1991; Leube et al., 1990; Ledru et al., 1991). Carbonaceous and Mn-Fe bearing chemical sedimentary units are intercalated with the volcanic rocks (Blanchot et al., 1972; Béssoles, 1977; Wright, 1985; Leube et al., 1990; Melcher, 1995; Kříbek et al., 2008).

The volcanic sequences of the Baoulé-Mossi domain were first described in the Birim Valley in Ghana (Kitson, 1918) and were classified as tholeiitic basalts and calc-alkaline lavas. This bimodal volcanic suite was also described by Abouchami et al. (1990) in craton-wide studies that concluded that tholeiitic suites were more abundant than calc-alkaline suites (Abouchami et al., 1990; Boher et al., 1992; Pouclet et al., 1996; Arndt et al., 1997; Lombo, 2009). Mg-rich tholeiites and calc-alkaline lavas were also described by Dia et al. (1997) from the Kénieba-Kédougou Inlier of western Mali. Blanchot et al. (1972), Béssoles (1977), Wright (1985), Abouchami et al. (1990), Leube et al. (1990) and others established that a volcanic sequence defined a basal succession to an overlying sedimentary sequence in volcano-sedimentary belts throughout the WAC.

Additionally, studies of the volcano-sedimentary belts by Dia (1988), Lüdtke et al. (1998), Béziat et al. (2000) and Dampare et al. (2008) concluded that tholeiitic and calc-alkaline volcanic rocks are characteristic of juvenile volcanic arcs. The tholeiitic basalts were interpreted as stratigraphically younger than the calc-alkaline sequences (Dia, 1988; Lüdtke et al., 1998; Béziat et al., 2000; Dampare et al., 2008; Baratoux et al., 2011). Pouclet et al. (1996), Arndt et al. (1997) and Lombo (2009) proposed that the basaltic sequences were represent oceanic plateaus that were derived from mantle plume activity, but Leube et al. (1990) and Pouclet et al. (1996) concluded that they formed in an intra-continental rift setting that evolved into an accretionary arc. Vidal and Alric (1994) interpreted that the basaltic sequences were the product of back-arc basin volcanism.

Pouclet et al. (1996) and Hirdes et al. (1996) described two major periods of volcanism for the WAC from two discrete but juxtaposed volcano-(sedimentary) belts in northeast Côte d'Ivoire; (1) an eastern belt is composed of basaltic and pyroclastic-dominated volcanic rocks that were emplaced at approximately 2185-2150 Ma (U-Pb zircon). The volcanic rocks are widespread in Ghana, eastern Côte d'Ivoire and eastern Burkina Faso (WAXI, 2013).

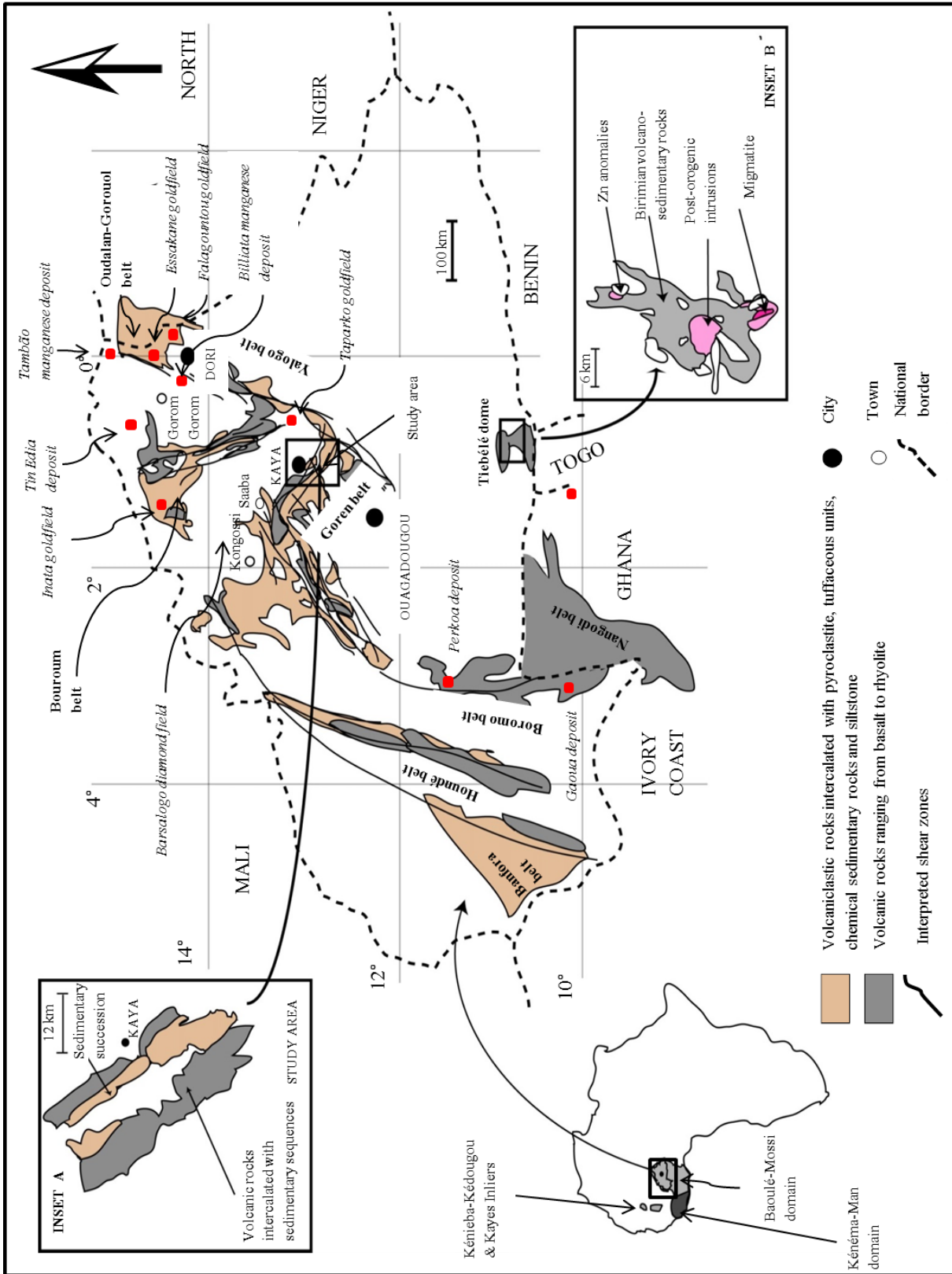


Figure 1.1. Volcano-sedimentary belts of southeast and northeast Burkina Faso and northwestern Ghana. Volcano-sedimentary belts from the northeast Burkina Faso are modified after Hein et al. (2004); the study area is located in the Goren belt and expanded in Inset A. Location of Tiebélé dome of southern Burkina Faso with Zn anomalies as defined by Ilboudo (2010) is presented in Inset B. The Perkoa and Gaoua deposits are located in the Boromo belt in Burkina Faso, southwest of Ouagadougou. The Essakane, Falagountou, Taparko and Inata goldfields are represented in north-northeast of Burkina Faso. The Billiata and Tambão Mn deposits and the Tin Edia Mn-Fe-V deposit are located on the western margin of the Oudalan-Gorouol belt. The Barsalogo diamond fields are located north of the Goren belt.

(2) a western belt in central Cote d'Ivoire, western Mali and Guinea, essentially composed of the equivalent volcanic products but geochronologically younger at approximately 2105 Ma (U-Pb zircon) (Hirdes et al., 1996).

Despite these investigations, surprisingly little research has been conducted on the volcanic sequences at the scale of one or several belts in West Africa. Few studies have been conducted on volcanic facies and metal potential in terms of base metals and Mn mineralisation, but delineating the volcanic facies and alteration zones of volcanic belts can help in identifying and targeting volcanic-related mineral deposits. For example, the Mount Reid volcanics in western Tasmania and the Abitibi greenstone belt of central Canada are both regions where volcanogenic massive sulphide mineralization has been found. Their volcanic facies and alteration zones are well understood, providing spatial constraints to economic mineralization (McPhie et al., 1993; Piché and Jébrak 2006).

Delineating facies is also important in developing tectonic models for volcanic terranes. Distal versus proximal facies and coherent versus volcanoclastic facies can be interpreted using lithological relationships, volcanic textures and rock composition. For example, in the Tiebélé Dome in southern Burkina Faso (Figure 1.1), chert and manganese horizons act as marker units in local volcano-sedimentary belts (Melcher, 1995; Ilboudo, 2010). The chert and manganese units are intercalated with Zn-rich volcanic-hosted massive sulphide (VHMS) mineralization, and manganese and silica were leached from the volcanic rocks during hydrothermal activity, synchronous to volcanism, and concomitant to precipitation at the water-rock interface (Melcher, 1995), i.e., syn-volcanic exhalative processes took place during eruption.

Volcanic terranes are often complicated because volcanic and sedimentary processes work at the same time (Cas and Wright, 1987; Lajoie and Stix, 1992) and volcanic and sedimentary rocks may be juxtaposed in a complicated manner. However, a comprehensive study of the volcanology, sedimentology and geochemistry of volcano-sedimentary belts can accurately reconstruct the volcanic environment.

This has been the focus of research in the southern Goren volcano-sedimentary belt (Figure 1.1) where the stratigraphy is characterised by a conformable sequence of meta-sedimentary rocks that are intercalated with basalt, andesite, dacite, pyroclastite and volcanic tuff, and carbonaceous and Mn-Fe bearing shale (Hein et al., 2004; Hein, 2010). The belt is weakly to moderately metamorphosed, giving a unique opportunity to study relatively pristine volcanic textures and establish volcanic facies. The volcano-sedimentary units have been mapped, sampled in detail and analysed both petrographically and geochemically. From field studies, geological and volcanic facies maps were created. This information has been used to interpret volcanic setting. The metallogenetic potential of the southern Goren volcano-sedimentary belt has also been assessed in this study.

1.2. Location and physiography

Burkina Faso is situated in West Africa and is bordered by Ghana, Benin, Togo, Mali, Niger and Côte d'Ivoire. It is a landlocked country that covers an area of 274 300 km². It lies mostly in the Sahel climatic zone.

The Sahelian zone is characterized by hot and arid conditions. Burkina Faso has an average daily temperature of 32° C and less than 25 cm of rainfall annually, particularly in the northern and northeastern regions (McFarland et al., 1998). Two seasons are predominant in Burkina Faso, namely the wet and dry seasons. The dry season occurs from October to May, which is followed by the wet season from June until September (Bierschenk, 1968; McFarland et al., 1998).

Geographically, the capital city of Ouagadougou is situated at the centre of the country. The Goren volcano-sedimentary belt is located in the Sanmatenga district. The belt is elongate and northwest-trending and extends from the towns of Kaya to Kongossi (Figure 1.1). The town of Kaya is approximately 90 km northeast of Ouagadougou and lies at the southeastern end of the belt. Kongossi is 60 km from Kaya and lies at the northeastern end of the belt. The belt is composed of two 100 km parallel branches that are characterized by topographic highs; the branches are separated by a relatively flat lying region up to 20 km wide.

An extensive ferricrete profile covers the GB as is typical for the West African craton in general (Brown et al., 1994; Beauvais et al., 2008). The ferricrete formed during the Cretaceous Period but was remobilised during the Palaeogene-Neogene in discrete erosion events, with ⁴⁰Ar/³⁹Ar dates of 59-45 Ma, 29-18 Ma, 18-11 Ma, 6 Ma and 3 Ma (Brown et al., 1994; Beauvais et al., 2008). The last three erosional periods were responsible for the formation of distinct three-level sediment surfaces seen throughout the GB (WAXI, 2013).

1.3. Project aims

The aims of this project include:

- (1) To map the southern Goren volcano-sedimentary belt and to create both lithological and volcanic facies maps.
- (2) To identify and classify the volcanic rocks within the field area according to volcanic texture, volcanic facies, mineralogy and chemistry.
- (3) To determine an original volcanic/tectonic setting using the composition, volcanic textures and volcanic facies of volcanic and associated sedimentary rocks.
- (4) To assess the exploration potential for mineralisation within the volcanic or meta-sedimentary rocks, specifically base metal sulphides and manganese.

1.4. Conventions and Acronyms

The referencing style adopted in this thesis is the Harvard style, used by the South African Journal of Geology (SAJG).

The conventions and acronyms used in this thesis include:

CIPW - Cross, Iddings, Pirsson, Washington
GB - Goren volcano-sedimentary belt
GPS - Global Positioning System
HFSE - High Field Strength Elements
HREE - Heavy Rare Earth Element
IAT – Intra-Arc Tholeiites
ICPMS - Inductively Coupled Plasma Mass Spectrometry
LILE - Large Ion Lithophile Elements
LREE - Light Rare Earth Element
MORB - Mid-Ocean Ridge Basalts
N-MORB - Normal MORB
OFB - Oceanic Flood Basalts
OGB - Oudalan-Gorouol belt
REE - Rare Earth Element
TTG -Trondjemite, Tonalite, Granodiorite
VHMS – Volcanic Hosted Massive Sulphide
WAC - West African Craton
XRF - X-Ray Fluorescence

1.5. Thesis Organisation

This thesis is organisation into eight chapters including the Introduction as follows:-

- (1) Chapter Two provides a review of the geology of West Africa, volcanology and volcanic-related ore deposits. Specific focus is given to the volcanic rocks of Burkina Faso.
- (2) Chapter Three provides a detailed description of the methodologies used in this thesis. It includes field work techniques, laboratory processes, data procurement and data analyses. Some of these processes include petrography, geochemical analyses and interpretations, and the use of ArcGIS®, Google Earth® and CorelDraw®.

- (3) Chapter Four presents field results including volcanic and sedimentary textures, rock types, field relationships and characteristic features of the rocks and images.
- (4) Chapter Five presents the results of petrographic studies of selected samples of volcanic rocks, including their mineralogy and modal abundances, metamorphic mineralogies, alteration mineralogies, and primary and secondary textures.
- (5) Chapter Six presents geochemical data, from major to trace element graphs, results, interpretations and a brief comparative study with geochemical work from the Boromo and Houndé belts of western Burkina Faso (Baratoux et al., 2011), the Tiebélé dome in southern Burkina Faso (Ilboudo, 2010) and the Oudalan-Gorouol belt in northeast Burkina Faso (Tshibubudze et al., 2013).
- (6) Chapter Seven presents the Discussion. The GB, and several belts from northeastern and western Burkina Faso, is contextualized within a regional and global framework.
- (7) Chapter Eight presents a summation in a Conclusion.

1.6. Limitations of the study

A major limitation to this study was the inability to continue fieldwork as a result of political instability and war in the neighbouring country of Mali from February to April 2013; foreigners were restricted from access to Burkina Faso north of the 13 Parallel (Figure 1.1), or advised against unnecessary travel. The result was a smaller sample suite and smaller mapping area. However, a comparative geochemical study was undertaken using data for volcanic samples from various volcano-sedimentary belts in Burkina Faso as an expanded study.

2. REVIEW OF WEST AFRICAN GEOLOGY

2.1. Stratigraphy

The West African Craton (WAC) is made up of Archaean and Palaeoproterozoic rocks and is divided into the Reguibat Rise in the north and the Leo-Man Rise in the south (Thiéblemont et al., 2004) (Figure 1.1). The Leo-Man consists of two domains, namely the Archaean Kénema-Man domain (3.54 Ga) in the southwest and the Palaeoproterozoic Baoulé-Mossi domain (2.3-1.8 Ga) in the east (Feybesse et al., 2006), with the exception of the Kénieba- Kédougou and Kayes Inliers, located between Mali and Senegal (Figure 1.1). The Birimian Supergroup makes up part of the Baoulé-Mossi domain and was deposited ca. 2.3 Ga (Feybesse et al., 2006; Pawlig et al., 2006). Deposition was followed by local micro-plate accretion during the Tangaean Event at 2.17-2.15 Ga (Tshibubudze et al., 2009; Hein, 2010; Baratoux et al., 2011; Tshibubudze and Hein, 2013; WAXI, 2013) and the polycyclic Eburnean Orogeny at approximately 2.14-2.05 Ga (Milési et al., 1991, 1992; Boher et al., 1992; Taylor et al., 1992; WAXI, 2013). The Tarkwa Group unconformably overlies the Birimian Supergroup and is characterized by conglomerate, quartzite and shale units, but does not crop out in the study area. The Tarkwa Group is interpreted to be the erosional product of the Birimian Supergroup and was intruded by various TTG suite plutons and deformed by the Eburnean Orogeny (Hastings, 1982; Leube et al., 1990; Milési et al., 1992; Castaing et al., 2003).

The stratigraphy of the WAC was originally established by Junner (1935), who identified dacitic/rhyodacitic volcaniclastic, greywacke, shale and chemical sedimentary units in what was termed the lower Birimian. Leube et al. (1990) identified tholeiitic basalts (intercalated with volcaniclastic sequences) as the upper Birimian. The tholeiitic basalt and volcaniclastic sequences formed at the same time in local sedimentary basins. Junner (1935; 1940), Ledru et al. (1991), and Milési et al. (1989, 1991) interpreted that the volcanic sequences were younger than the sedimentary basins. However, Hein et al. (2004) and Hein (2010) concluded that the volcanic and meta-sedimentary rocks formed part of an intercalated sequence. Baratoux et al. (2011) argued that the sedimentary basins in western Burkina Faso exhibited complicated strato-structural relationships, making it difficult to establish local stratigraphy. However, recent studies by WAXI (2013) concluded that the stratigraphy of the WAC is dependent on the spatial and temporal distribution of belts relative to accretionary terranes.

Importantly, a detailed stratigraphic study was conducted by Baratoux et al. (2011) across three greenstone belts in western Burkina Faso (namely the Boromo, Houndé and Banfora belts) (Figure 1.1). Their study confirmed that the belts are composed of calc-alkaline andesite and dacite, intercalated tuff layers, pyroclastic flows, Mn-Fe rich chert layers and volcaniclastic sedimentary rocks that overlie basal units of tholeiitic basalt. The study clearly showed that tholeiitic basalts are

older than the calc-alkaline series of lavas for the Boromo, Houndé and Banfora belts. However, craton-wide studies by WAXI (2013) indicated that the stratigraphic order of volcanic rocks cannot be generalised (some belts do not host tholeiitic and/or calc-alkaline volcanic rocks) and thus the stratigraphy of each greenstone belt must be established independently.

2.2. Granitoid and dolerite emplacement

The emplacement of tonalite-trondjemite-granodiorite (TTG) plutons and granites in the WAC is restricted to 2200, 2160-2130 and 2100-2070 Ma according to Pawlig et al. (2006) and Gueye et al. (2008). The Palaeoproterozoic Birimian Supergroup was systematically intruded by a suite of TTG granitoids, diorite and leucogranite plutons (Pons et al., 1995; Naba et al., 2004; Pawlig et al., 2006; Vidal et al., 2009). TTG and diorite emplacement at 2200 Ma and 2160-2130 Ma preceded the Eburnean Orogeny, while granite-leucogranite emplacement at 2100-2070 Ma was concurrent with the Eburnean Orogeny (Leube et al., 1990; Cheillett et al., 1994; Pons et al., 1995; Hirdes and Davis, 2002; Pawlig et al., 2006; Gueye et al., 2008; WAXI, 2013). The presence of TTG suite plutons in West Africa is interpreted as (indirect) evidence for subduction in the Precambrian (Martin, 1994; Martin et al., 2005) because TTG have some similarities to modern slab melts and arc magmatic rocks. (Drummond and Defant, 1990).

In Burkina Faso, two granitoid emplacement events are recognized (Castaing et al., 2003; Naba et al., 2004): (1) a suite of granodiorite, tonalite and diorite plutons intruded the Birimian Supergroup (2210-2160 Ma), and (2) a granite suite intruded the Birimian Supergroup and TTG suite granitoids (2150-2130 Ma) (Castaing et al., 2003). A suite of granodiorite and granite plutons (2255-2253 Ma) in the Oudalan-Gorouol belt (OGB) of northeast Burkina Faso may represent basement to the Birimian Supergroup in the WAC (Tshibubudze et al., 2013).

A swarm of WNW and NW-trending dolerite dykes crosscut the WAC including the GB. They are generally composed of plagioclase, clinopyroxene and magnetite and are currently dated at 215 ± 15 Ma (K-Ar whole-rock age) (Hottin and Ouedraogo, 1992).

2.3. Metamorphism and deformation

The Birimian Supergroup in northern Burkina Faso underwent deformation during the Tangaean Event (2170-2150 Ma) (Tshibubudze et al., 2009; Hein, 2010; Tshibubudze and Hein, 2013) as well as craton-wide deformation associated with regional metamorphism during the Eburnean Orogeny (2145-2100 Ma) (Hein et al., 2004; Feybesse et al., 2006; Hein, 2010; Baratoux et al., 2011; Tshibubudze and Hein, 2013; WAXI, 2013), and deformation during the Wabo-Tampelse Event (undated) (Hein et al., 2004; Hein, 2010; Baratoux et al., 2011). Metamorphic grades during the Tangaean reached lower

greenschist facies at most (WAXI, 2013). Regional metamorphism in the Eburnean Orogeny attained greenschist facies (Milési et al., 1989, 1991; Bossière et al., 1996; Hirde et al., 1996) with the development of chlorite, muscovite, epidote and actinolite mineral assemblages, and low to medium grade amphibolite facies with the introduction of hornblende (Bossière et al., 1996; Béziat et al., 2000; Debat et al., 2003; Naba et al., 2004). Granulite facies metamorphic rocks crop out in the Oudalan-Gorouol belt on the margin of the Dori batholith in the Gorom Gorom region (Tshibubudze and Hein, 2013), and in the Pissila batholith in the Saaba region (Simoko, 2012).

Three deformation events are recognised in northeast Burkina Faso:

- (1) D1 (Tangaean Event) resulted in NW-trending dextral reverse shear zones, folds and an S1 foliation. The shortening direction was SW-directed (Tshibubudze et al., 2009; Hein, 2010; Tshibubudze and Hein, 2013). D1 is recognised in northern Ghana by de Kock et al. (2011) and southern Ghana by Perrouty et al. (2012) as the Eoeburnean (WAXI, 2013).
- (2) D2 is characterized by NNE-NE trending shears, folds and an S2 foliation parallel to axial planes of the folds, caused by NW-SE compression which is defined by the Eburnean Orogeny (Milési et al., 1989; Feybesse et al., 2006; Hein, 2010; Baratoux et al., 2011).
- (3) D3 is characterized by WNW trending shears and folds. An associated S3 foliation formed during N-S compression. This event is termed the Wabo-Tampelse Event (Hein et al., 2004; Hein, 2010; Baratoux et al., 2011).

2.4. Metallogenesis

Metallogenesis in the northeast of Burkina Faso includes gold, diamonds, Mn-Fe, silver, lead, molybdenum, copper and zinc (Hastings, 1982; Milési et al., 1989, 1992; Hein et al., 2004; Tshibubudze et al., 2009). In the Oudalan-Gorouol belt, manganese deposits occur at Tambão and Billiata (Figure 1.1) and Fe-Ti-V mineralization occurs in the Tin Edia deposit. Gold occurrences include commercially mined goldfields such as Essakane, Inata and Taparko goldfields, as well as artisanally mined deposits such as Falagountou artisanal mine. They occur as shear and quartz vein-hosted deposits. Diamondiferous lamproite and lamprophyre plugs and dykes crop out NNW of Kaya in the Pissila batholith in the Barsalogo diamond field, with rare kimberlite pipes (WAXI, 2013).

In other parts of the WAC, nickel, chromium and platinum group elements (PGEs) occur in ultramafic layered intrusions (Mickus, 2008). Schwartz and Melcher (2003) described (1) Zn-Ag-Ba mineralisation at Perkoa (Figure 1.1), which they classified as a volcanic-hosted massive sulphide (VHMS) deposit, and (2) Cu-Au mineralisation at the Gaoua deposit, which they interpreted as porphyry copper in style. Such mineralisation styles are known to form in compressional tectonic environments and support the idea that one or many arcs existed (Baratoux et al., 2011). The syn-

volcanic VHMS deposit of the Tiebélé Dome in the south of Burkina Faso is a sphalerite bearing, zinc-rich exhalative deposit (Ilboudo, 2010).

2.5. The Goren volcano-sedimentary belt

The Goren volcano-sedimentary belt was deposited approximately 2400-2300 Ma and is characterized by a conformable sequence of sedimentary rocks, interbedded with volcaniclastic and pyroclastic deposits. Intercalated with this succession are mafic to intermediate volcanic rocks (Hein et al., 2004; Hein, 2010). The belt has subsequently been subjected to three deformation events as well as intruded by various intrusive bodies and is metamorphosed to sub-greenschist to middle greenschist facies (Hein et al., 2004; Kříbek et al., 2008).

Hein et al. (2004) established the stratigraphy of the GB which comprises a succession of siltstone and volcaniclastic units that stratigraphically young into a mafic-intermediate volcanic succession. The volcanic rocks are made up of an intercalated sequence of hyaloclastic basalt, pillowd basalt, massive-variolitic basalt, andesite and dacite. The upper section of the stratigraphy is made up of a second volcano-sedimentary succession containing siltstone-shale beds, pebble-boulder conglomerates, greywacke-turbidite, felsic pyroclastic deposits, with thin intercalations of basalt and andesite (Figure 2.1).

Immediately west of the GB, volcanic, pyroclastic and sedimentary sequences are intruded by several tonalite and granodiorite plutons, and a megacrystic granite, as well as a number of greenschist facies meta-gabbro and meta-diorite intrusions. The Loudo and Pissila batholith crops out east of the GB. The Pissila batholith is made up of biotite and hornblende granodiorites (Figure 2.1.) (Simoko, 2012; WAXI, 2013) and is cross-cut by tonalite dykes and pegmatite veins. WNW-NW trending dolerite dykes (215 ± 15 Ma; K-Ar whole-rock age; Hottin and Ouedraogo, 1992) cross-cut the GB (Hein et al., 2004; Hein, 2010).

The supracrustal successions, Pissila batholith and various mafic intrusions of the GB were deformed during the Tangaean Event at 2170-2150 Ma (Hein, 2010). This was followed by a second deformation in which the supracrustal rocks were progressively subjected to NW-SE shortening during the Eburnean Orogeny (2145-2100 Ma; WAXI, 2013) as well as the emplacement of granodiorite and tonalite plutons. D1 and D2 structures were crosscut by the Wabo-Tampelse Event (undated) in a period of north-south shortening.

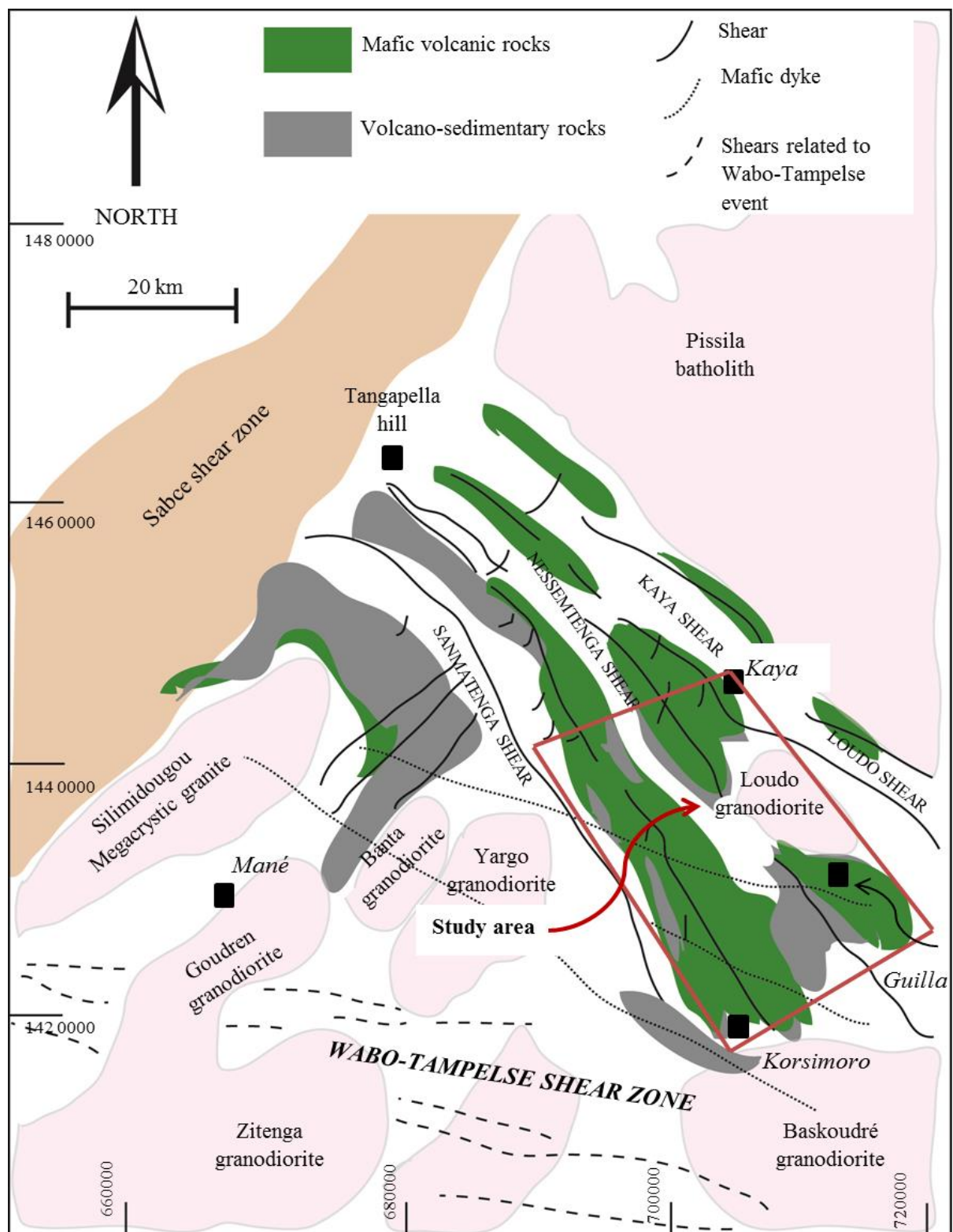


Figure 2.1. The Goren volcano-sedimentary belt is presented showing the locations of Kaya, Mané, Guilla, Korsimoro, Sirgui artisanal mine and Tangapella hill. Northwest and northeast trending shears and thrusts are represented as well as WNW trending shears of the Wabo-Tampelse Event. A variety of granodiorite intrusions are shown including the Pissila batholith and Loudo granodiorite that crop out to the east of the Goren belt. The Silimidougou megacrystic granite crops out to the west of the Goren belt. This image is modified after Hein et al. (2004) and Hein (2010).

3. METHODOLOGY

3.1. Field Methods

A desktop study of the field area was completed using high resolution satellite imagery from Google Earth® prior to fieldwork. The images were studied in order to determine the most efficient way to undertake mapping, reconnaissance work, identifying possible sample location sites and possible traverse lines. Geological mapping focused on contacts, structures, facies delineation and volcanic textures. The purpose was to create geological and facies maps (Figure 3.1 and 3.2) with relevant cross sections (Figure 3.2) and graphic logs of field traverses (Figure B1 and B2, Appendix B). Wherever possible, lithologies were correlated from outcrop to outcrop. Outcrop was limited to the ridges.

Field mapping was conducted with the essential tools. These included a compass clinometer to measure bedding and structural orientations, and a GPS that recorded the co-ordinates of the station points. The coordinates recorded on the GPS correspond to the UTM WGS 84 grid system (Zone 30P). Photographs were taken at every station point to provide evidence of observations and textures.

Three field seasons were planned for between January 2012 and December 2013; however, only two were completed. The field area was officially declared unsafe in January 2013 because of civil war in the neighbouring country of Mali, and access to the GB was restricted to foreigners. Due to the restricted access, a comparative study was undertaken using geochemical data by Ilboudo (2010) for the Tiebélé Dome in southern Burkina Faso, and Baratoux et al. (2011) for the Boromo, Houndé and Banfora belts, in order to investigate similarities and differences with the samples from the GB.

The January 2012 field season was a reconnaissance season intended to gain insight into the size of the field area and ideal locations for sampling. Limited sampling and mapping was completed during this time. The March-April 2012 field season focused on detailed geological mapping and sampling.

The spacing between traverses varied, depending on accessibility, but never exceeded 3 km. Sampling was completed along each traverse in such a way as to ensure acquisition of a broad sample suite with specific focus on weakly deformed zones of low metamorphic grade. Permissions were gained from the Bureau des Mines et de la Géologie du Burkina (BUMIGEB) to remove samples from Burkina Faso. The samples were transported to the University of the Witwatersrand Johannesburg for preparation and geochemical analyses, as well as petrographic study.

A unique aspect of this study was the identification of volcanic facies in the field, in conjunction with an analysis of sedimentary rocks, both of which required considerable time and focus. Hein et al. (2004) attempted to classify sequences of volcanic rock on volcanic textures in the GB; however, a careful facies study, coupled with geochemistry and petrography provided insight into the volcanic

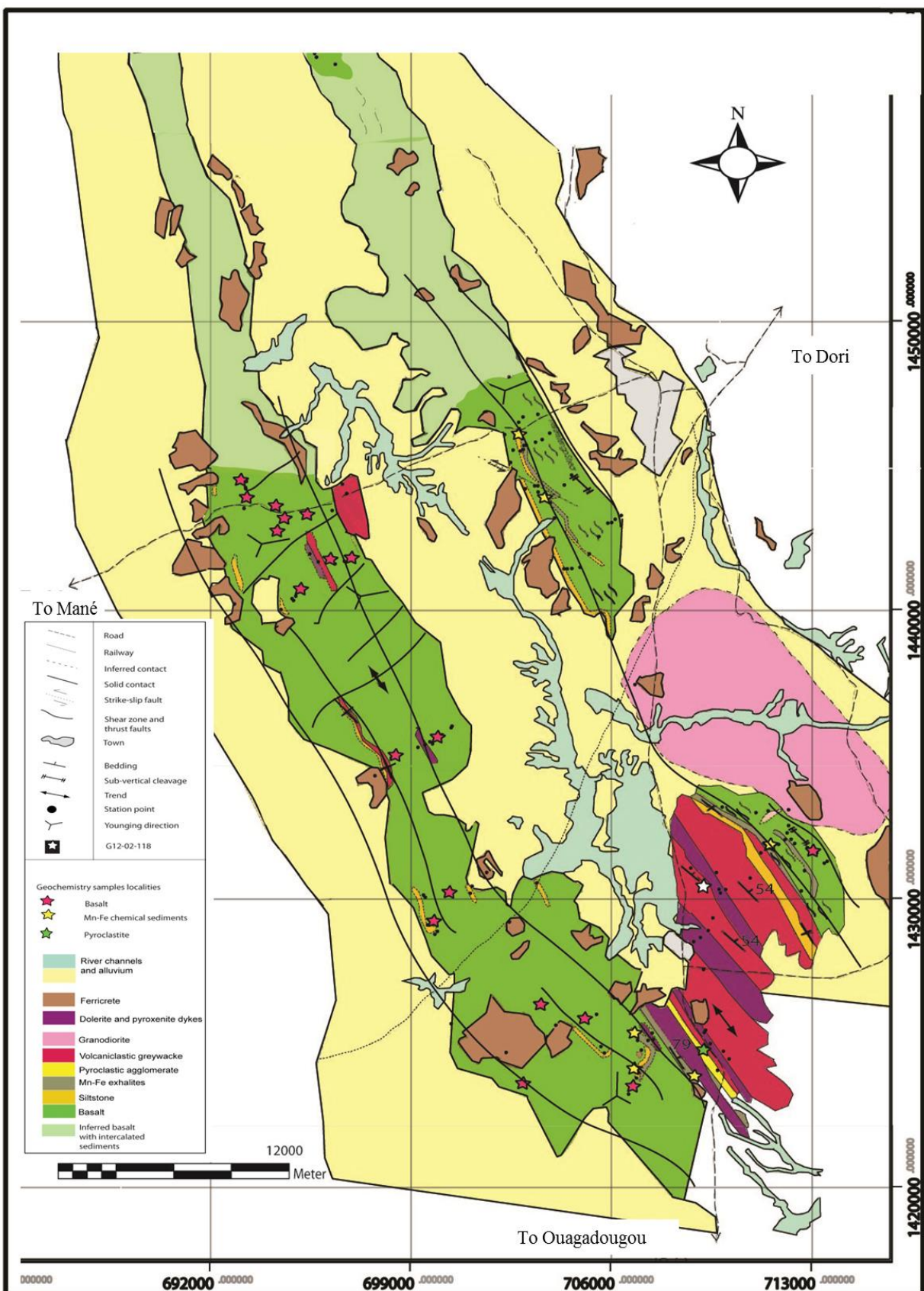


Figure 3.1. Geological map of the southern Goren belt presenting rock types, major structures, infrastructure and geochemical sample points.

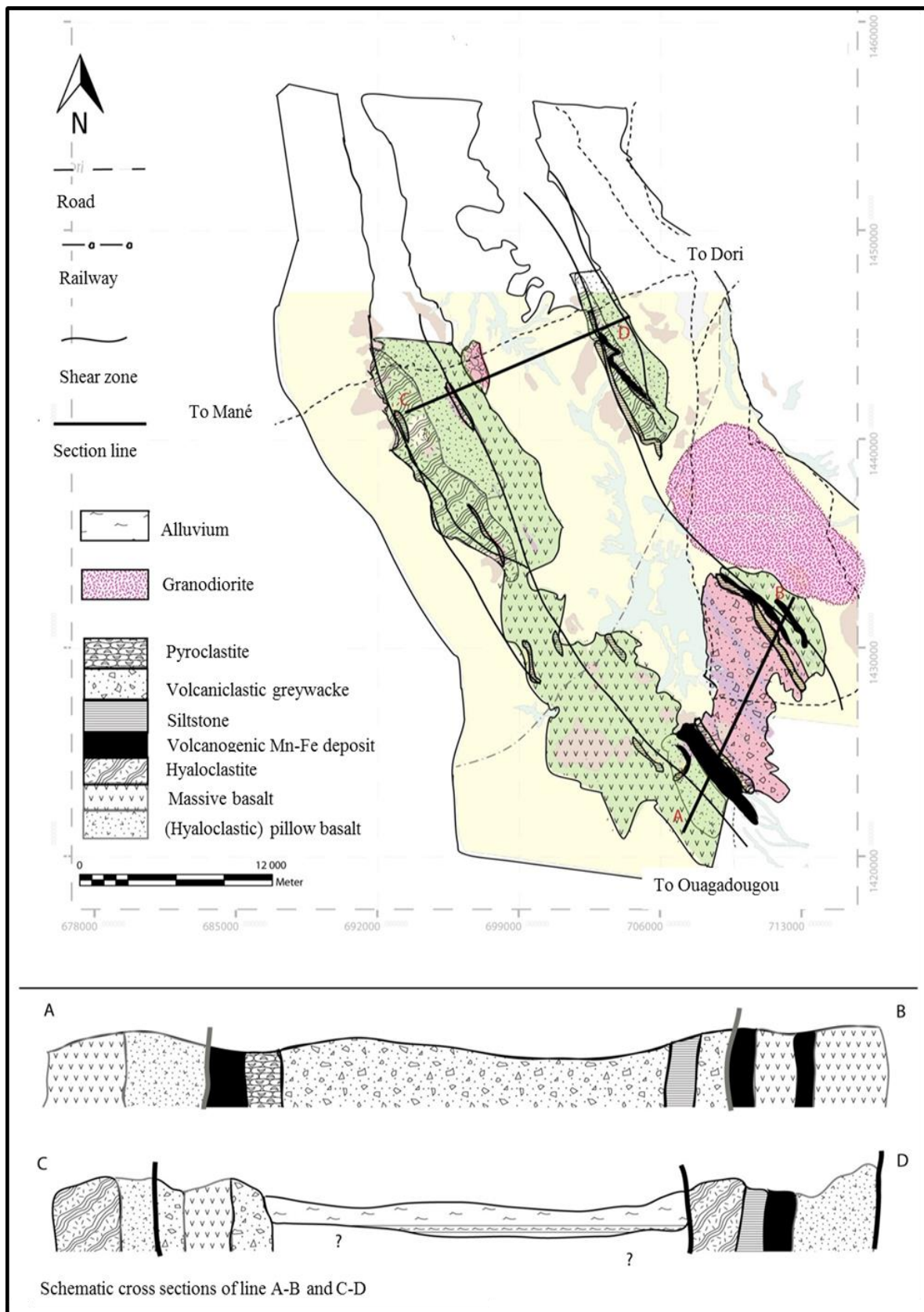


Figure 3.2. Volcanic facies map of the southern Goren belt representing the location of various facies and major structures. Two schematic section lines, A-B and C-D, are drawn.

environment at the time of deposition, in a similar way that sedimentary rocks have yielded information about provenance and crustal evolution (e.g., McLennan et al., 1990, 1995).

In ancient terranes, such as the WAC, metamorphism, deformation and erosion limit the preservation of volcanic textures (McPhie et al., 1993). However, in regions where metamorphism and deformation are less intense, textural preservation of samples may exist.

The study of volcanic textures is an effective way of delineating volcanic facies. It enables the identification of both coherent and volcaniclastic facies (Cas and Wright, 1987; McPhie et al., 1993). The term *volcaniclastic* in this context includes rocks from autoclastic, pyroclastic and reworked volcano-sedimentary facies (Lajoie, 1984; Lajoie and Stix, 1992; McPhie et al., 1993). Hyaloclastites and flow breccias indicate autoclastic facies, which often occur near coherent lavas (Lajoie and Stix, 1992). Lavas can develop numerous textures, most because of cooling, such as those observed in the GB (e.g., hyaloclastites, jointing and volcanic glass).

For example, the greenschist facies Mt Reid volcanics of western Tasmania yield fairly well preserved volcanic textures where the rocks are not strongly altered by hydrothermal processes and/or deformed (McPhie and Allen, 2003). An example of this is the devitrification of volcanic glass, as described by McPhie and Allen (op cit., 2003); crystal boundaries remain intact and the glass recrystallises as zeolites with a minor proportion of clay minerals.

As a further example, metamorphosed Triassic basalt lavas in NW Croatia were interpreted as proximal to intermediate facies by Palinkaš et al. (2008) based on volcanic textures such as closely packed pillows, hyaloclastite, pepperite and tortoise-shell jointing. These textures unequivocally evidenced subaqueous rift-related extrusion.

It is without doubt that determining individual flow units or the original geometries of volcanic centres can be difficult, especially in old terranes. However, facies relationships are important as they provide strong evidence of environments of deposition. They are useful for palaeo-environment reconstruction and establishing metallogenic potential. Thus the approach of Cas and Wright (1987), McPhie et al. (1993), Allen et al. (1996), and McPhie and Allen (2003) in analysing volcanic facies in detail to establish the environments of deposition, have been used in this research.

3.2. Laboratory Methods

X-ray fluorescence (XRF) and inductively coupled plasma mass spectrometry (ICPMS) analyses were completed at the Earth Lab at the University of the Witwatersrand, Johannesburg. Twenty-nine (29) samples were analysed. The XRF analyses were able to determine the composition of each sample in terms of major and minor elements. ICP-MS analyses were completed to specifically measure the composition of minor and trace elements. Also, by using two different methods of analysis, potential discrepancies could be detected, e.g., similar Zr values (in ppm) from both analyses indicated consistent results and improved confidence.

Samples were initially crushed into smaller pieces using an automated crusher manufactured by Dickie and Stockler (Pty) Ltd. These fragments were then ground to a fine powder in a pneumatic milling machine, TS-250 MILL manufactured by Dickie and Stockler (Pty) Ltd. All crushing and milling was done with extreme care as to avoid contamination. Thorough cleaning, good packaging and correct labelling was ensured to provide a high level of quality control (QA/QC) during sample preparation. Many of the samples were analysed twice to ensure that no erroneous errors were produced, thus assuring QA/QC during sample analyses.

3.2.1. Summary of XRF Analyses

Analysis for all major elements was completed on a fused disk. Preparation of the fused disk included:

- (1) All samples were ignited at 1000°C for 40 minutes and the LOI (Loss of Ignition) was calculated.
- (2) The ignited sample was mixed with a pre-ignited flux (with composition Li₂B₄O₇ = 47%, Li₂CO₃ = 36.7%, La₂O₃ = 16%) in the ratio of 1:5 and fired for 40 minutes at 1000°C.
- (3) This was then poured and pressed by a mechanical press into a fused disk.

All data collection was performed on a PANalytical PW2404 WD XRF manufactured by Axios® at the EarthLab at the University of the Witwatersrand, Johannesburg with a Rh tube set at 50kV and 50mA, an analysis time of 40 sec per element, and 20 sec per background (backgrounds were measured for Si, Al, Mg, Na and P only). The specific elemental data is presented in Table 3.1:

Element	Analysis Line	Crystal	Collimator	Detector
Ti	Ka	LiF200	150 µm	Flow
Ca	Ka	LiF200	150 µm	Flow
K	Ka	PE 002-C	550 µm	Flow
Si	Ka	PE 002-C	550 µm	Flow
Al	Ka	PE 002-C	550 µm	Flow
Mg	Ka	PX1	550 µm	Flow
Na	Ka	PX1	550 µm	Flow
P	Ka	Ge 111-C	550 µm	Flow
Ni	Ka	LiF 220	150 µm	Duplex
Fe	Kb	LiF 220	150 µm	Flow
Mn	Ka	LiF 220	150 µm	Duplex
Cr	Ka	LiF 220	150 µm	Duplex

Table 3.1. Major element calibration instrument parameters.

The elemental concentrations were obtained by comparison to 13 known standards. The standards used included W2, GSP1, BHVO2, AGV2, G2, DTS1, PCC1, BCR2, NIM N, NIM P, NIM S, NIM D, NIM G (Govindaraju, 1994). A synthetic internal standard was run after every 5 analyses to monitor and compensate for instrumental drift. Agreement to recommended values was better than 0·7% for all major elements and 5% for trace elements.

All trace elements were analysed for pressed pellet. The preparation of the pressed pellet was achieved by mixing approximately 6g of sample with three drops of 4% commercially purchased Mowiol (polyvinyl alcohol). This mixture was then pressed under 10 ton pressure into an aluminium cup using a 40 ton press. The pressed pellet was allowed to dry for 24 hours prior to analysis.

PANalytical software Protrace® was used to process the raw data. The standards used for the calibration were the standards supplied by PANalytical. Protrace® drift standards were also run after every five analyses to compensate for instrument drift. Internal checks were performed by analysing known standards as unknowns and comparing them to reported concentrations. The known standards used were AGV2, BHVO2, GSP2, NIM D and NIM S (Govindaraju, 1994).

3.2.2. Summary of ICP-MS analyses

The methodology for ICP data is taken from the Earth Lab at the University of the Witwatersrand, Johannesburg. The samples were prepared in a clean laboratory, which had special HEPA filters, along with other filters that remove all airborne contaminants. Samples were dissolved in a MARS microwave digester.

50mg of sample was added to 6ml HF/HNO₃ (3:2) and placed into the microwave digester at 235°C and 450 PSI, for 40 minutes. Samples were then evaporated on a hot plate at 70°C until all liquid was evaporated. 2ml of HNO₃ was added, the beakers capped and placed on a hot plate at 60°C for 24 hours. The cap was removed and beakers placed on a hot plate at 70°C until all liquid was evaporated. 2ml of HNO₃ was then added and left to evaporate. Once all the liquid was evaporated 100µl of HNO₃ was added and the sample was ready for the ELAN DRC-e ICP-MS, manufactured by PerkinElmer Sciex®

The samples were diluted with an internal standard and introduced into the ICP-MS through a nebulizer where they were mixed with argon gas. They then passed through plasma which was at 75 000°C. The elements in the sample were ionized by the plasma and became positively charged by losing their loosely bound electrons. These positively charged ions then moved into the quadrupole where they were sorted based on their mass to charge ratio, after which, they moved to a detector which received the ion signal that was proportional to the concentration. The concentration of the sample could be determined through calibration with certified reference material, such as single or multi-element reference standards. Every ICP-MS determination was accompanied by control standards BCR-1, BHVO-1 and BIR-1 and for all elements the deviation was less than 10% from recommended values.

3.3. Petrography

Polished thin sections and ore blocks were made for various pre-selected basalt and sedimentary samples. This included thin sections of 28 basalt samples, 9 dykes, 3 Mn-Fe-rich carbonaceous sedimentary rocks, 1 pyroclastic breccia and 1 volcanoclastic greywacke sample. The ore blocks included 2 basalt samples and 3 Mn-Fe-rich carbonaceous sedimentary samples.

Petrographic analyses using transmitted light microscopy included:

- (1) Mineral identification.
- (2) Determination of modal abundances for each mineral.
- (3) Classification of the sample according to its mineralogy and alteration.
- (4) Identification of textures, including primary volcanic and sedimentary textures as well as secondary metamorphic and alteration textures.
- (5) Determination of the metamorphic grade using the mineralogy.

Reflected light microscopy was used to identify oxide and sulphide minerals, their relationship to silicate minerals and how they were hosted (e.g. disseminated, vein-hosted). Their modal abundances, sizes and occurrences were described.

Photomicrographs were taken of selected samples in order to emphasise certain textures. These images were captured using an Olympus DP26 camera which was attached to an Olympus BX51 petrographic microscope. Reflected light petrography was operated by an Olympus TH4-200 light box. The software used in conjunction with the Olympus microscope and camera was Olympus Stream Essentials® version 1.7. Images were taken, after which the appropriate scale bar was burned onto the image.

3.4. Maps and images

Google Earth®, ArcGIS® 10, Corel Draw® 9 and Adobe Illustrator® CS 2 were used to create maps and images. Station points were imported from a Garmin Etrex-high sensitivity hand-held GPS device to Google Earth®. This process was done during field work as it assisted with daily field planning. A mosaic of the field area was created using Google Earth® satellite imagery. The mosaic was imported into ArcGIS®, then geo-referenced to the WGS84 UTM co-ordinate system for UTM Zone 30. Grid lines were added in ArcGIS®. The image was exported to CorelDraw® where polygons and lines were overlain. The polygons and lines represented the lithologies, structure and infrastructure (Figure 3.1). Adobe Illustrator® was used to create the facies map (Figure 3.2), facies model (Figure 7.1), and other schematic diagrams.

Microsoft Publisher® 2010 was used to edit and format all geochemical graphs (refer to Figures 6.1-6.18), after they were created in Sigma Plot® version 11.0 and Microsoft Excel® 2010. All calculations concerning the geochemical data were completed in Excel®. The calculated data were

then copied into Sigma Plot® in order to produce scientific graphs that Excel cannot do, such as ternary diagrams.

4. ROCK TYPES OF THE GOREN BELT

4.1. Introduction

The rock types of the southern Goren Belt (GB) consist primarily of basalt units that are intercalated with a succession of sedimentary rocks and pyroclastic breccia. These rocks were intruded by TTG suite plutons including the Pissila Batholith and the Loudo granodiorite (Figure 2.1), and pyroxenite, dolerite and aplite dykes. The basalt, sedimentary rocks and pyroclastic breccias are metamorphosed to sub-greenschist (Kříbek et al., 2008), or middle greenschist facies (Hein et al., 2004), with amphibolite facies adjacent to plutons and dykes. This research was focused in areas of the southern GB, where primary volcanic and sedimentary textures were only affected by sub-greenschist and lower-middle greenschist facies metamorphism.

4.2. Basaltic rocks

The basalts of the southern GB exhibit limited, but distinctive volcanic textures, typical of basaltic rocks. They are homogenous, fine-grained, and brownish-green in colour on fresh broken surfaces. Textures such as vesicles and amygdales, pillows and hyaloclastic brecciation are common. Less common features include tortoise-shell jointing, varioles and flow bands. Quartz-calcite-epidote veins commonly crosscut the basalts.

Aphyric to aphanitic textures dominate the study area. They are typically composed of plagioclase-clinopyroxene microlites (approximately 2:1). The modal abundances ranged from 5-20 % plagioclase and 2-10 % clinopyroxene.

Porphyritic basalts crop out south of the Mané Road (Figure 4.1); they are predominantly plagioclase-phyric with plagioclase crystals ranging from 0.1-1.5 mm, with rare occurrences in which plagioclase crystals measure 1.2 cm in length (station point G12-02-099; UTM 30P 696917; 1441719). These porphyritic basalts are thus like the megacrystic tholeiitic basalt units described by Baratoux et al. (2011) from the Houndé and Boromo belts (Figure 1.1).

Amygdales are present in most outcrops and increase in concentration near the margin of individual flow units. It was difficult to identify multiple flow units in the field because of poor outcrop continuity, but some evidence suggested that more than one flow unit existed. Such evidence included the upper boundary of a flow unit continuing into the lower boundary of another, separated by a thin chill margin. Pipe amygdales are preserved in some outcrops (co-ordinates UTM 30P 0713145; 1431643 and UTM 30P 713245; 1431519) and are oriented towards the upper margin of individual flow units.



Figure 4.1. Photograph of plagioclase crystals in porphyritic basalt (rare) demonstrating preferential weathering. Crystals measure 1.5 cm in length (Station point G12-02-098; UTM 30P 693240; 1443462).

Hyaloclastic basalt breccias crop out throughout the southern GB as discrete units and as inter-pillow detritus in pillow basalts. Commonly pillow basalt grades into hyaloclastite breccia units. Breccia fragments are surrounded by a fine crystalline matrix and/or altered volcanic glass. Hyaloclastite breccia dominates in units of loosely packed pillows (Figure 4.2a).

Pillow lavas are abundant throughout the study area, particularly in the western arm of the GB between the Mané road and the Kaya-Ouagadougou national highway. The pillows range in size from 10 to 100 cm across.

Several outcrops present well defined re-entrants, with vesicle accumulation on the pillow margins, and chilled margins (Figure 4.2b, c). Stratigraphic facing was established from the orientation of the pillow re-entrant, the direction of pillow inflation, and the direction in which amygdales increased in concentration. These textures indicated that the overall stratigraphic facing direction was north-northeast with only one facing west-southwest locality (Station point G12-02-131). The pillow forms decrease in stratigraphically upward, which is a texture described by McPhie et al. (1993), who observed that pillows tended to decrease in size as they stratigraphically young during a period of continuous volcanism. In the study area a decrease in pillow size was observed over a distance of 5 m.

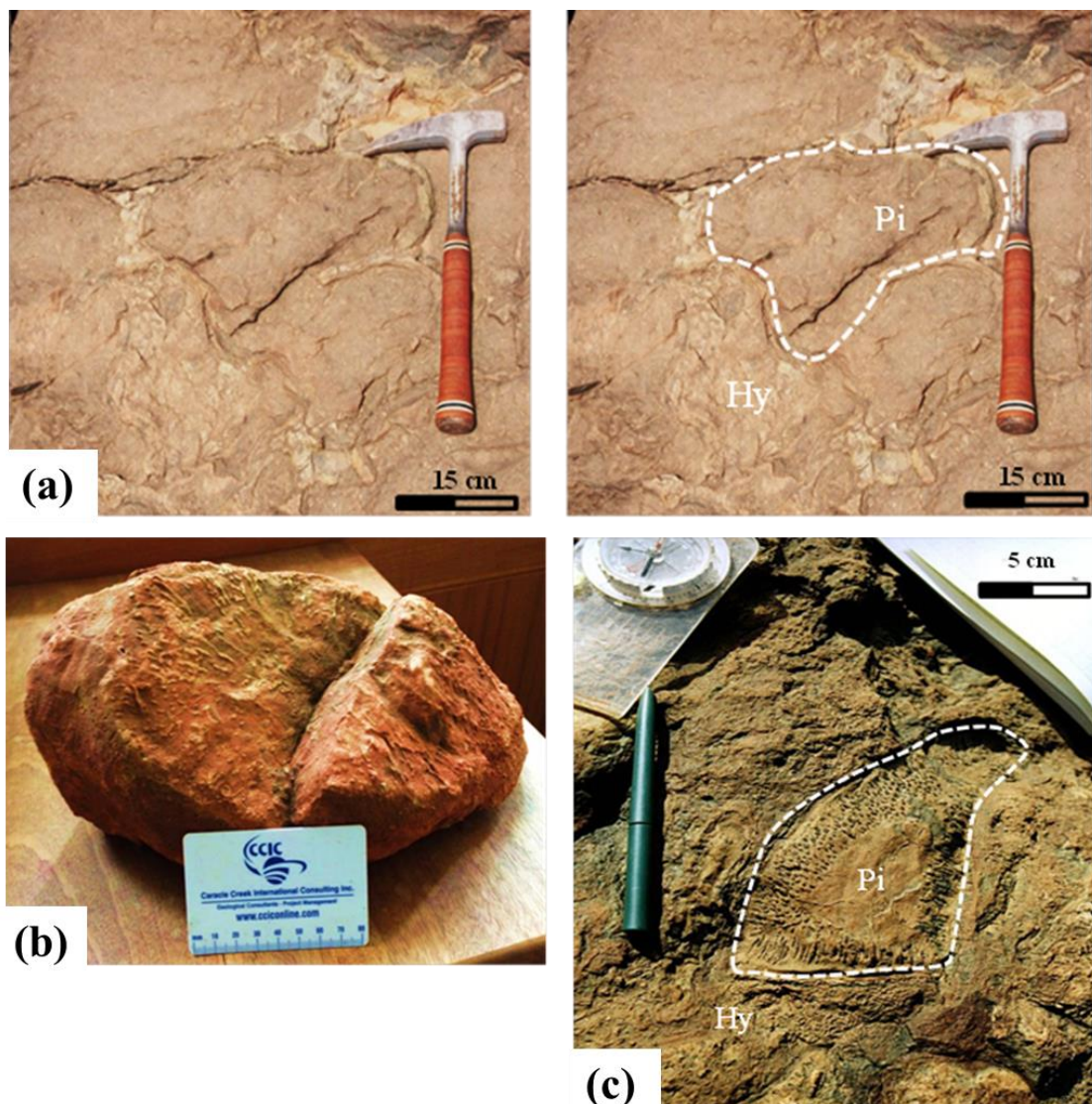


Figure 4.2. (a) Photograph of pillows in a hyaloclastic breccia (*Pi* = Pillow; *Hy* = Hyaloclastite) where the hyaloclastic breccia is observed in the inter-pillow domains (Sample G12-02-110, UTM 30P 694964; 1440271). Pillows are 20-30 cm with chill margins less than 1 cm thick. (b) Photograph of amygdaloidal pillowed basalt with amygdales concentrated on the pillow margins compared to the centre of the pillow (Sample G12-008, UTM 30P 694317; 1443450). The amygdales are elongate toward the margin of the pillow and measure 2 cm in length. (c) Photograph of hyaloclastic pillow basalt displaying an ~10 cm pillow with well-defined amygdale accumulation on the margin of the pillow, with hyaloclastic breccia enclosing it.

In some locations, pillows are flattened (Figure 4.3a). Furthermore, a range of syn-volcanic deformation textures are present and these relate to cooling of the basalt units after extrusion. The deformation textures included:-

- (1) Pseudo-pillows representing a texture derived from cooling of massive basalt (c.f., McPhie et al., op cit.).
- (2) Syn-volcanic tensile fractures (Figure 4.3b). These fractures are approximately 5 cm in length and are caused by differential cooling of the basalt pile.
- (3) Tortoise-shell joints, which are interpreted to be the result of the interaction of lava with cold fluid, water or air during extrusion (Figure 4.3c).

Flow banding occurs. The bands measure ~1 cm in thickness (Figure 4.4a). The bands are mineralogically controlled, as observed by the colour of each band. Leucocratic bands are plagioclase-rich whereas melanocratic bands are epidote-chlorite rich.

The basalt units south-east of the Mané Road and adjacent to the Sirgui artisanal mine (Figure 2.1) are texturally well-preserved. They not only show well-defined pillow basalts, but a variety of features related to flow and cooling. This includes hyaloclastite (Figure 4.4b), jointing and flow banding. Differential weathering exposed large plagioclase crystals (0.5-1.2 cm) which stand out outcrop (Figure 4.1).

Variolitic basalts crop out between Mané and the Silimidougou megacrystic granite and in isolated outcrops in the Tangapella region, in the central northern GB (Figure 2.1). The varioles are approximately 0.5-2.0 cm in diameter and composed of plagioclase feldspar crystals.

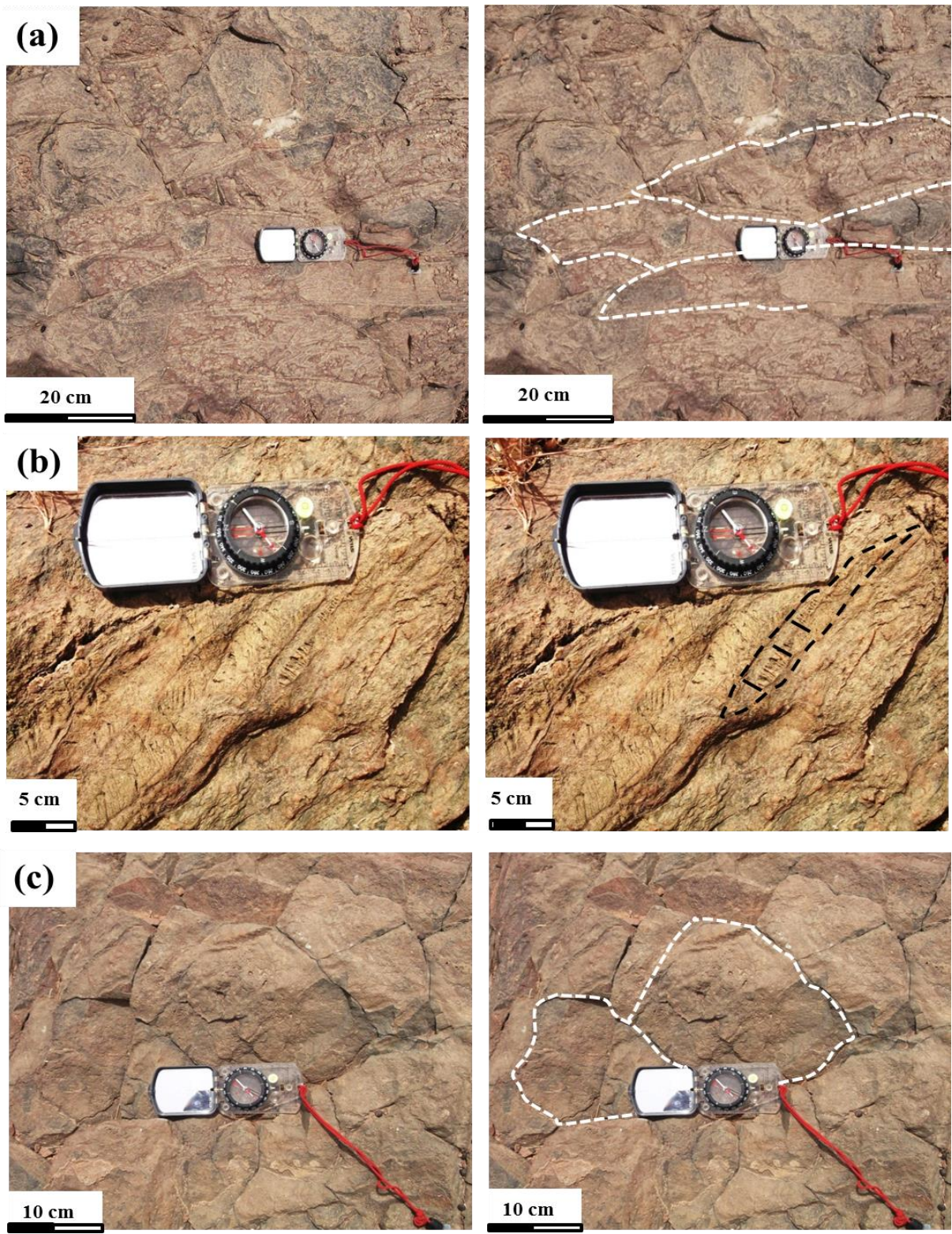


Figure 4.3. (a) Photograph of pillowed basalt that has undergone flattening (Station point G12-02-083; UTM 30P 703920; 1446075). Re-entrants and rinds are still visible. Stratigraphic facing is to the north (top of the photograph). (b) Photograph of a basalt with vertical fractures that are interpreted to be the result of cooling (Station point G12-02-004; UTM 30P 703585; 1426248). (c) Photograph of tortoise shell jointing in basalt that is interpreted to be the result of cooling (Sample G12-02-095; UTM 30P 695421; 1443258). Polygonal jointing is fairly well-defined.

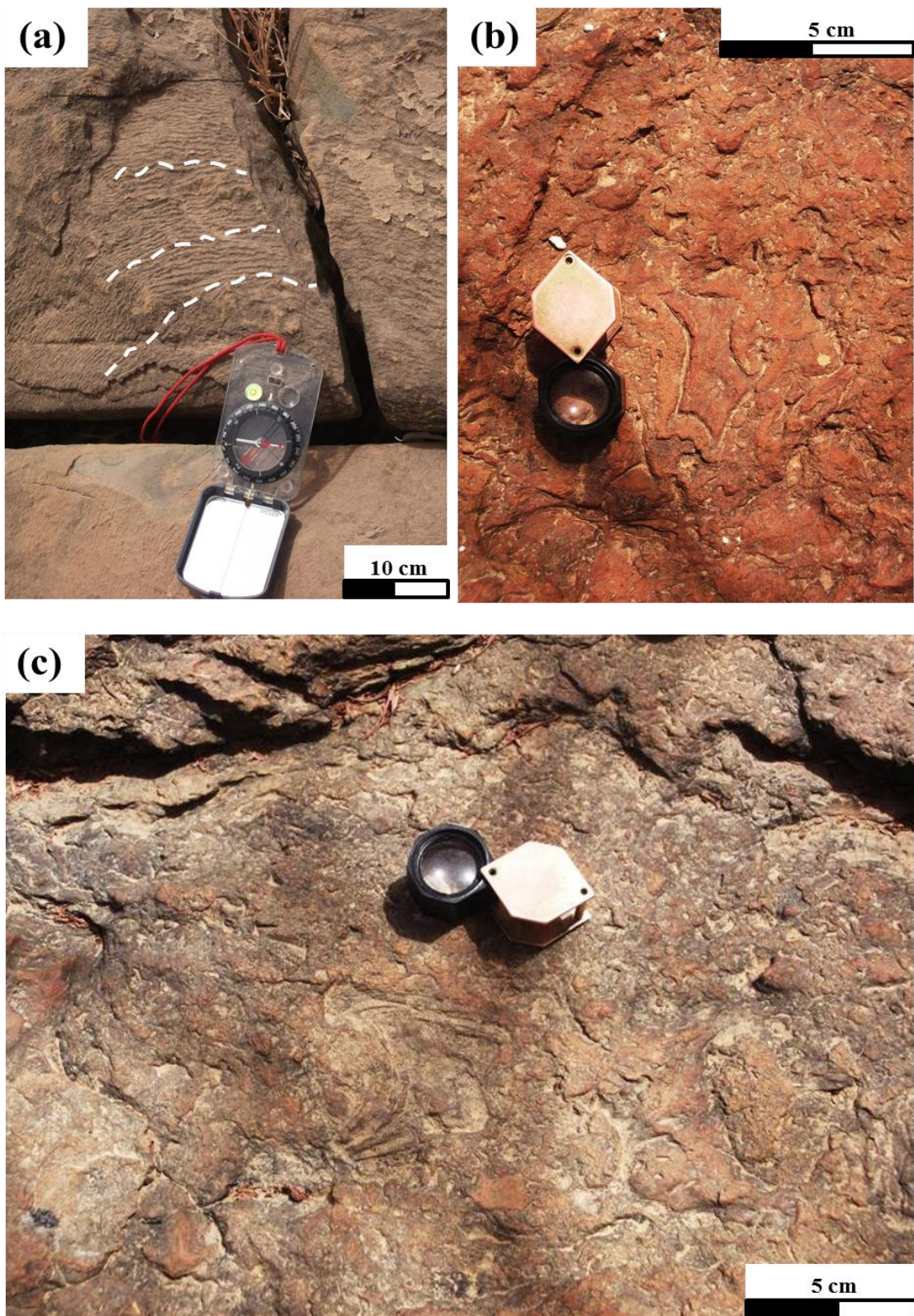


Figure 4.4. (a) Photograph of flow banding in a basalt (Station point G12-02-098; UTM 30P 693240; 1443462). The flow bands were identified by light and dark banding that is interpreted to be caused by differential mineral accumulation. (b, c) Photographs of hyaloclastic basalt interstitial to loosely packed pillow basalts (Station point G12-02-099; UTM 30P 696917; 1441719). Various shapes result from fragmentation of the basalt and stand out due to differential weathering.

4.3. Metasedimentary rocks

Siltstone, volcaniclastite, greywacke and exhalative Mn-Fe-rich carbonaceous sedimentary rocks constitute an interbedded sequence of sedimentary rocks in the GB. Individual lithologies are between 2 and 50 metres in stratigraphic thickness.

4.3.1. Siltstone

The laterally extensive siltstone units in the GB are noticeably deformed and tightly folded. Structurally, they have well-defined cleavage planes, micro-faults and outcrop-sized isoclinal folds. They are made up of alternating Fe-rich and Fe-poor beds of fine-grained, silt-sized detritus (Figure 4.5a). Beds range in size from 5 mm to 6 cm. Planar laminations are well preserved.

4.3.2. Volcaniclastite

A poorly sorted, medium to coarse-grained volcaniclastite unit crops out along both arms of the southern GB, particularly, along the western arm. The volcaniclastite unit consists of fine to medium-grained plagioclase, chlorite and fine lithic fragments. It is commonly interbedded with the siltstone and basalt but the unit is poorly exposed across the study area and is poorly preserved.

4.3.3. Greywacke

The greywacke succession is volcaniclastic. In outcrop, primary bedding features such as planar cross bedding, flame structures, mud drapes, chert interbeds, conglomerate beds (~20 cm thick) and scour marks are present. The greywacke is typically coarse-grained and poorly sorted and is composed of quartz, plagioclase, hornblende, clinopyroxene and chert clasts. The succession is pyritised in part, with visible pyrite in some beds (e.g. Station point G12-02-118; Figure 3.1). The succession trends northwest and dips northeast with a mean strike and dip of 145° 54° NE.

Interbedded conglomerate horizons also present as basal units of a fining-upwards succession. They are characterized as rounded to sub-rounded pebble quartzite (0.5-4.0 cm), with minor chert pebbles (Figure 4.5b) that grade into gritstone, sandstone and siltstone, representing an overall fining upwards sequence (Figure 4.5c, d). Mud balls are also seen throughout the greywacke succession.

4.3.4. Pyroclastic breccia

A northwest-trending pyroclastic breccia deposit crops out along the western branch of the GB (Figure 3.1) as an interbed within the greywacke succession, and over a strike length of approximately 5 km. The unit has been dated at 2192 ± 9 Ma (U-Pb zircon, WAXI, 2013) and is reported by Hein et al. (2004) as the upper volcano-sedimentary sequence for the GB. The pyroclastic breccia is generally polylithic, ungraded and poorly-sorted. It is made up of euhedral to subhedral crystals of quartz, plagioclase, hornblende and minor clinopyroxene. Crystals of ilmenite and magnetite are visible in hand specimen. Sub-rounded blocks and bombs (5-20 cm in diameter) are accidental lithic fragments

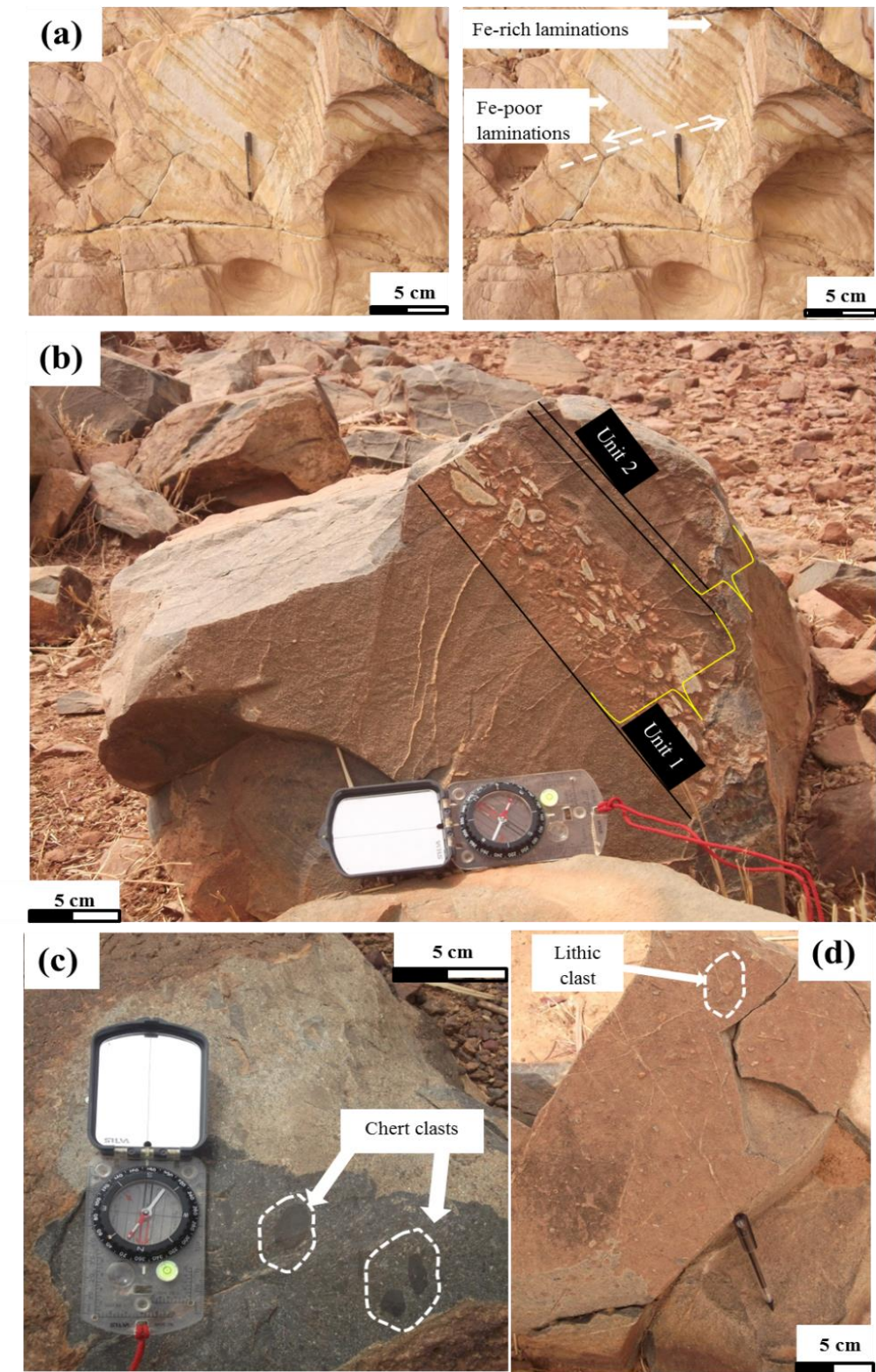


Figure 4.5. (a) Photographs of siltstone showing well-defined Fe-rich and Fe-poor laminations (G12-02014; UTM 30P 711294; 1431532). Bed thicknesses range from 1 mm to 5 cm. Micro-faults crosscut the siltstone. The siltstone exhibits well developed cleavage planes, particularly prominent in the Fe-rich layers. (b) Photograph of a fining upward greywacke succession with thin monomictic conglomerate interbeds making up the basal unit of Bouma sequences (G12-02-119; UTM 30P 708845; 1431001). The basal layer of Unit 2 is composed of coarse-grained gritstone compared to the conglomerate layer of Unit 1. The depositional environment is interpreted as a marginal marine-offshore setting. (c) Photograph of a poorly sorted volcanogenic greywacke deposit with angular fragments. The greywacke is composed of rounded chert clasts and is matrix-supported (Station point G12-02-010; UTM 30P 696828; 1443986). (d) Photograph of a polylithic, poorly sorted, massive volcanogenic greywacke (Sample G12-02-093, UTM 30P 709616; 1429270). The angular fragments measure up to 3 cm in size.

interpreted to have been incorporated in the breccia during volcanic eruption(s). Ash and lapilli-sized detritus in the breccia varies in size from 1 mm to 5 cm (Figure 4.6 a, b).

4.3.5. Mn-Fe-rich carbonaceous sedimentary rocks

Northwest-trending Mn-Fe-rich, carbonaceous sedimentary rocks crop out throughout the study area, parallel to the overall lithological trend of the GB. These rocks are characterized by fine-grained, carbon-bearing massive units, or finely laminated units with a variable amount of carbon. They commonly exhibit soft-sediment deformation textures such as randomly orientated, metre-sized isoclinal slump folds. They are interpreted to have formed during gravity sliding prior to lithification.

The Mn-Fe-rich sedimentary units are often interbedded with thin (1.0 cm thick) chert beds. They are dominated by ankerite, hematite, magnetite, and braunite. Centimetre-scale botryoidal textures are present and are common supergene alteration features of Fe and Mn minerals in the WAC. Light-coloured dolomite beds (5 to 30 cm thick) occur as interbeds within the Mn-Fe-carbon-rich beds. The Mn-Fe-rich carbonaceous sedimentary rocks are crosscut by bedding-parallel and stockwork-brecciated quartz-carbonate veins.

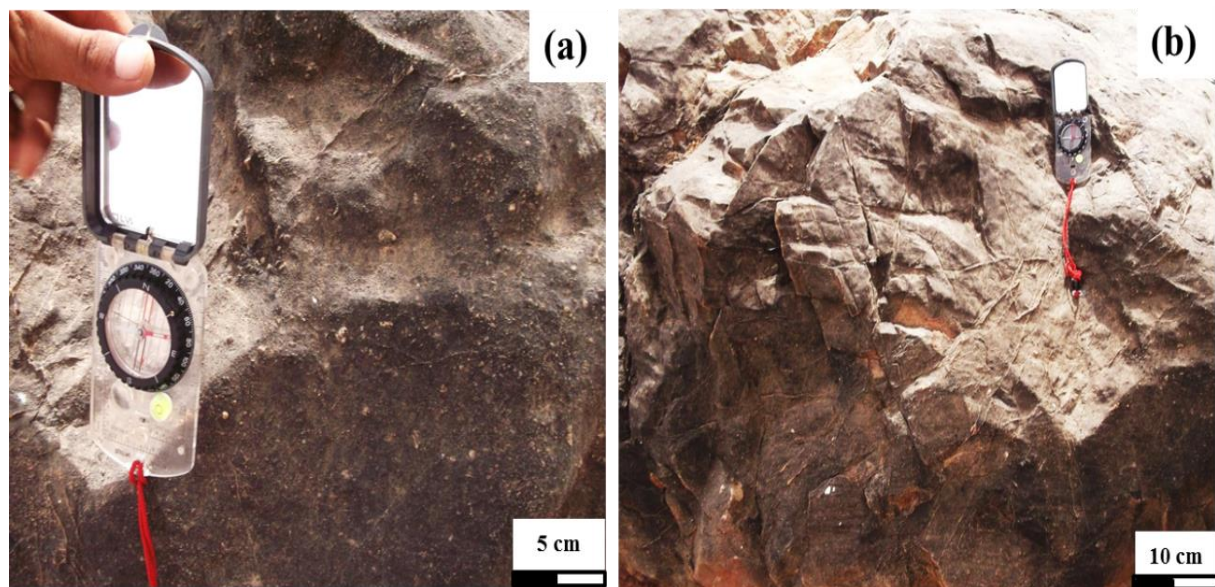


Figure 4.6. (a-b) Photograph of a polyolithic, non-bedded, lapilli-bomb dominated pyroclastic breccia deposit with angular to sub-angular crystals of ilmenite, magnetite, plagioclase, quartz and hornblende, ranging in size from 2 mm to 7 cm (Sample G12-02-126, UTM 30P 709365; 1424791).

4.4. Intrusions

4.4.1. Mafic dykes and sills

Undated pyroxenite and dolerite dykes and sills (20 m to several hundreds of metres) crosscut the supracrustal rocks of the field area. The dykes and sills trend northwest, parallel to sub-parallel to

bedding, and crop out throughout the southern GB. They are medium to coarse crystalline (0.4-2 cm) and composed of plagioclase, clinopyroxene, hornblende and minor orthopyroxene.

Variations in composition and modal abundances are measured. Dolerite dykes and sills were characterized by average modal abundances of 45 % plagioclase and 40-45 % clinopyroxene. The remaining mineralogy is identified as Fe-oxides. Hornblende usually makes up approximately 10 % of the modal abundance when present. In Sample G12-02-017, the proportion of hornblende attained 30 %; hornblende-rich dolerite has a proportionally lower percentage of clinopyroxene.

The pyroxenite dykes and sills were classified according to their higher proportion of clinopyroxene relative to plagioclase. This is typically 70-80 % clinopyroxene with less than 15 % plagioclase.

4.4.2. Aplite dykes

Northeast-trending aplite dykes occur in the GB. They are medium-grained (3 mm crystal size) with visible quartz, plagioclase and K-feldspar.

4.4.3. Loudo granodiorite

The Loudo granodiorite crops out south of Kaya in the study area. It was described by Hein et al. (2004) as hornblende granodiorite with a plagioclase, quartz, hornblende, K-feldspar, biotite groundmass. It hosts mafic xenoliths that vary in size and shape. The southern contact crops out south of the town of Loudo where it intrudes basalt. A discrete contact aureole is defined.

5. PETROGRAPHIC OBSERVATIONS OF SELECTED SAMPLES FROM THE GOREN BELT

5.1. Basaltic rocks

A petrographic study of 28 basalt samples was completed at the University of the Witwatersrand Johannesburg. The petrography shows that the basaltic rocks are dominantly aphyric and compositionally similar. The primary mineralogy of the samples is composed of clinopyroxene and plagioclase. Plagioclase and clinopyroxene made up between 5 and 15 % of the samples as variably altered microlites (Figure 5.1a). Disseminated Fe-oxides, ilmenite and magnetite, comprise a large modal abundance, approximately 20-40% of the samples (Figure 5.1b). They occur interstitially as subhedral and euhedral crystals and range in size between 0.2-2.0 mm. Disseminated, fine-grained (< 0.1 mm), subhedral to euhedral sulphides such as pyrite and chalcopyrite constitute an approximate 0.5-2.0% of the modal abundance. For the porphyritic plagioclase-phyric basalts described in Section 4.2, the phenocryst abundance is approximately 5 % (Figure 5.1c).

Plagioclase crystals in the basalt samples are generally < 0.4 mm in size except for porphyritic samples in which plagioclase phenocrysts are 0.5-1.5 mm. The crystal shapes vary from anhedral to subhedral, and euhedral forms are rare. Euhedral plagioclase crystals are typically tabular, occasionally elongate (lath-like), and display clearly defined albite twinning. Intensely altered plagioclase is identifiable from relict albite twinning.

Clinopyroxene crystals range from < 0.1 mm to 0.4 mm in size. They are generally anhedral to subhedral in shape. Twinning, supposedly rare (c.f., Nesse, 2000) is present in some of the clinopyroxene crystals.

The 28 basalt samples present a range of volcanic textures as described in Chapter 4. The textures include amygdales, basaltic hyaloclastic breccia, varioles, as well as porphyritic and aphyric texture. Petrographically, circular to irregular shaped amygdales are commonly filled with quartz, calcite, epidote and zeolite group minerals (Figure 5.1d). Crystal growth within amygdales commonly radiates inward from the margins. The amygdales vary in diameter from 0.5 mm to greater than 5 mm. In some instances, amygdales are composed of a micron-scale fill of chlorite (Figure 5.2).

Petrographically, the hyaloclastic breccia samples are composed of finely crystalline, aphanitic basalt fragments. They contain a matrix of fine-grained polycrystalline quartz, calcite, zeolite group minerals, needle-shaped actinolite, epidote and chloritised volcanic glass (Figure 5.2 b, c). Quartz-carbonate veins crosscut the hyaloclastite breccia, suggesting vein infill occurred after cooling and fragmentation took place. Epidote veins also crosscut hyaloclastic breccia fragments.

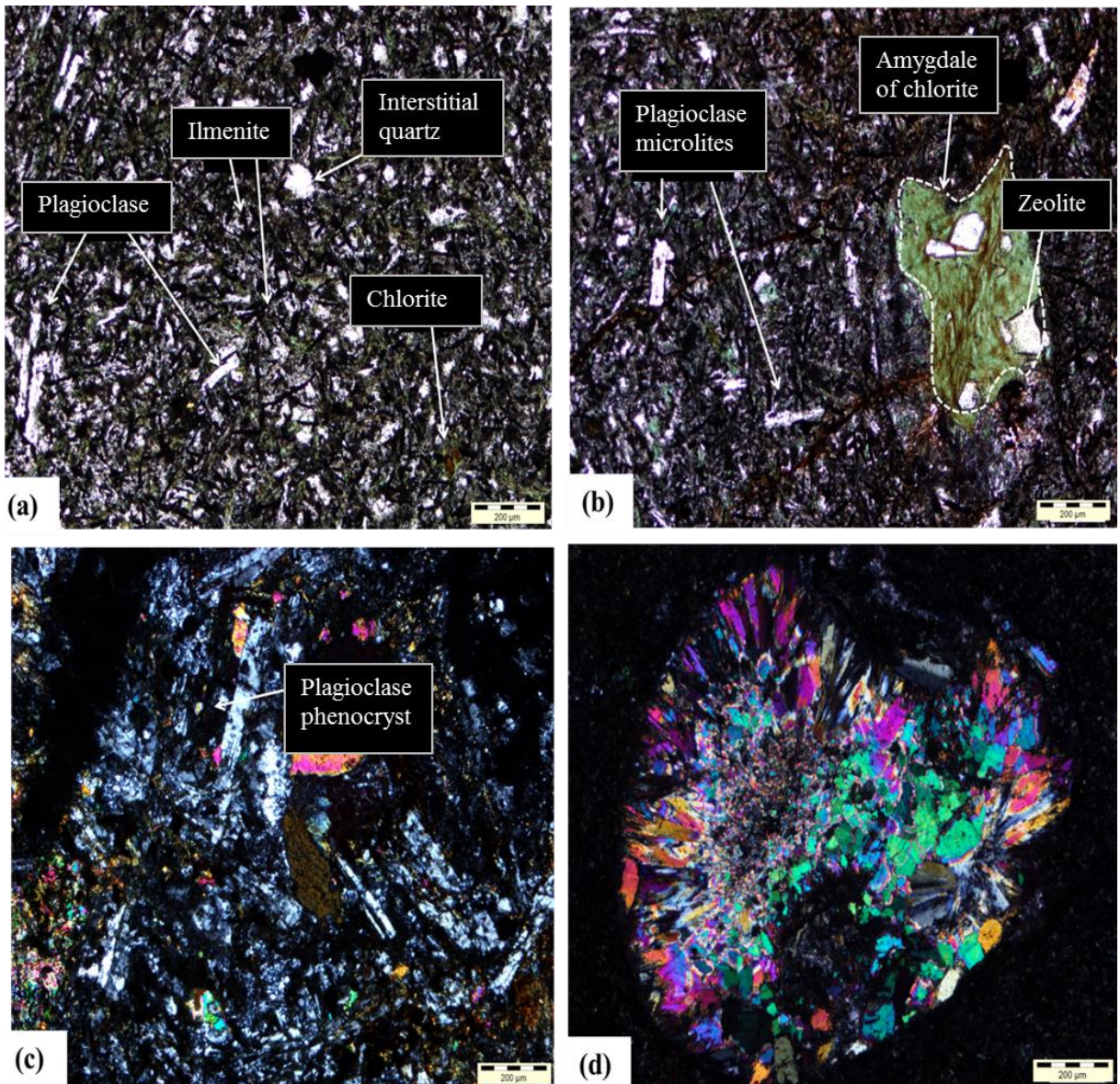


Figure 5.1. (a) Photomicrograph of basalt exhibiting subhedral plagioclase microlites, a largely chlorite-epidote replaced groundmass, and an amygdale containing chlorite and subhedral zeolite crystals (Sample G12-009; plane polarized light). (b) Photomicrograph of a microlitic basalt containing < 1.5 mm euhedral plagioclase microlites, anhedral ilmenite (opaque), interstitial quartz and a high proportion of chlorite (Sample G12-009; UTM 30P 693302; 1444147; plane polarized light). (c) Photomicrograph of a porphyritic basalt with 0.5-1.0 mm partly altered plagioclase crystals. The groundmass is composed of chlorite and epidote, which is interpreted to be the result of plagioclase and clinopyroxene microlite alteration (G12-018; UTM 30P 695652; 1466804). (d) Photomicrograph of an amygdale in amygdaloidal basalt. The amygdale is interpreted to form due to passive degassing of the basaltic liquid and these are filled with various minerals at a later stage. In this case, the infill is with epidote and zeolite group minerals. The amygdale exhibits a sub-rounded shape in which the zeolite crystals radiate inward from the amygdale boundary toward a fine-grained aggregate of epidote (Sample G12-02-057; UTM 30P 699990; 1435556; cross polarized light).

Microscopically, variolitic basalts are composed of altered, skeletal plagioclase. The plagioclase crystals radiate outward from a central nucleus. Varioles measure 0.5 mm in diameter.

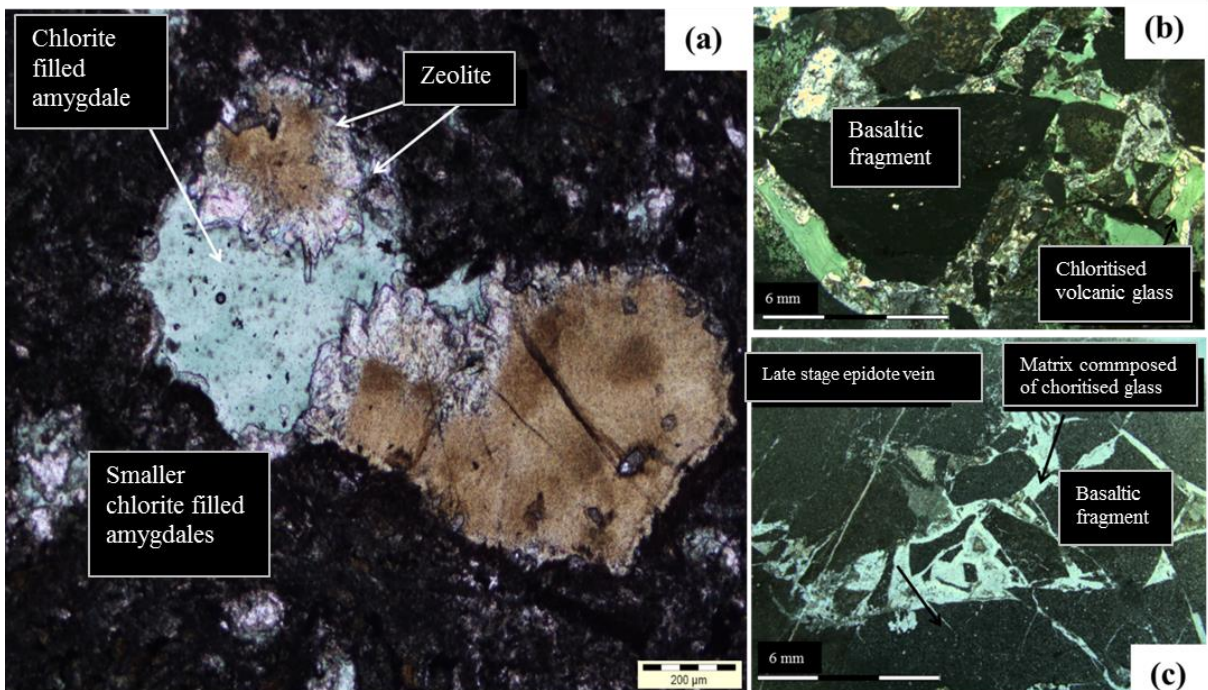


Figure 5.2. (a) Photomicrograph of a medium grained, amygdaloidal basalt that displays a partly chloritised amygdale filled with devitrified glass. The amygdale is rimmed by zeolites. Smaller amygdales in the image are also filled with chlorite and zeolite (G12-02-096; plane polarized light). (b, c) Photomicrographs of hyaloclastic basalt (1:1 scale) that is altered to chlorite-actinolite. The hyaloclastite is brecciated in a jigsaw of basalt fragments. The breccia matrix is composed of chloritised volcanic glass. Late stage epidote veins crosscut the hyaloclastic breccia (G12-02-099; UTM 30P 696917; 1441719 and G12-02-057; UTM 30P 699990; 1435556; plane polarized light).

With regard to alteration mineralogies, the 28 basalt samples were, in general altered to a fine-grained assemblage of epidote, chlorite, and actinolite with accessory calcite, zeolite and quartz (Figure 5.3a, b). Epidote and chlorite replaced pyroxene as reaction rims, crystal core replacement and overgrowths. In turn, hematite-goethite overprints epidote and chlorite. Plagioclase is partially to completely replaced by chlorite leaving ghost relict twins and taking the form of the plagioclase crystal. Some basalt samples present a non-pervasive mineral foliation defined by chlorite, actinolite and quartz. Calcite and quartz occur primarily in veins, indicating that quartz-carbonate alteration postdates metamorphism (Figure 5.3c.). Interstitial, polycrystalline quartz was also abundant as part of the metamorphic alteration assemblage.

Pyrite and chalcopyrite occur in veins or fractures (Figure 5.3d) and on the margin of primary, disseminated sulphide and oxide crystals. The presence of vein-hosted sulphides and sulphide rims around disseminated oxide-sulphides is interpreted to be primary and/or secondary sulphide precipitation.

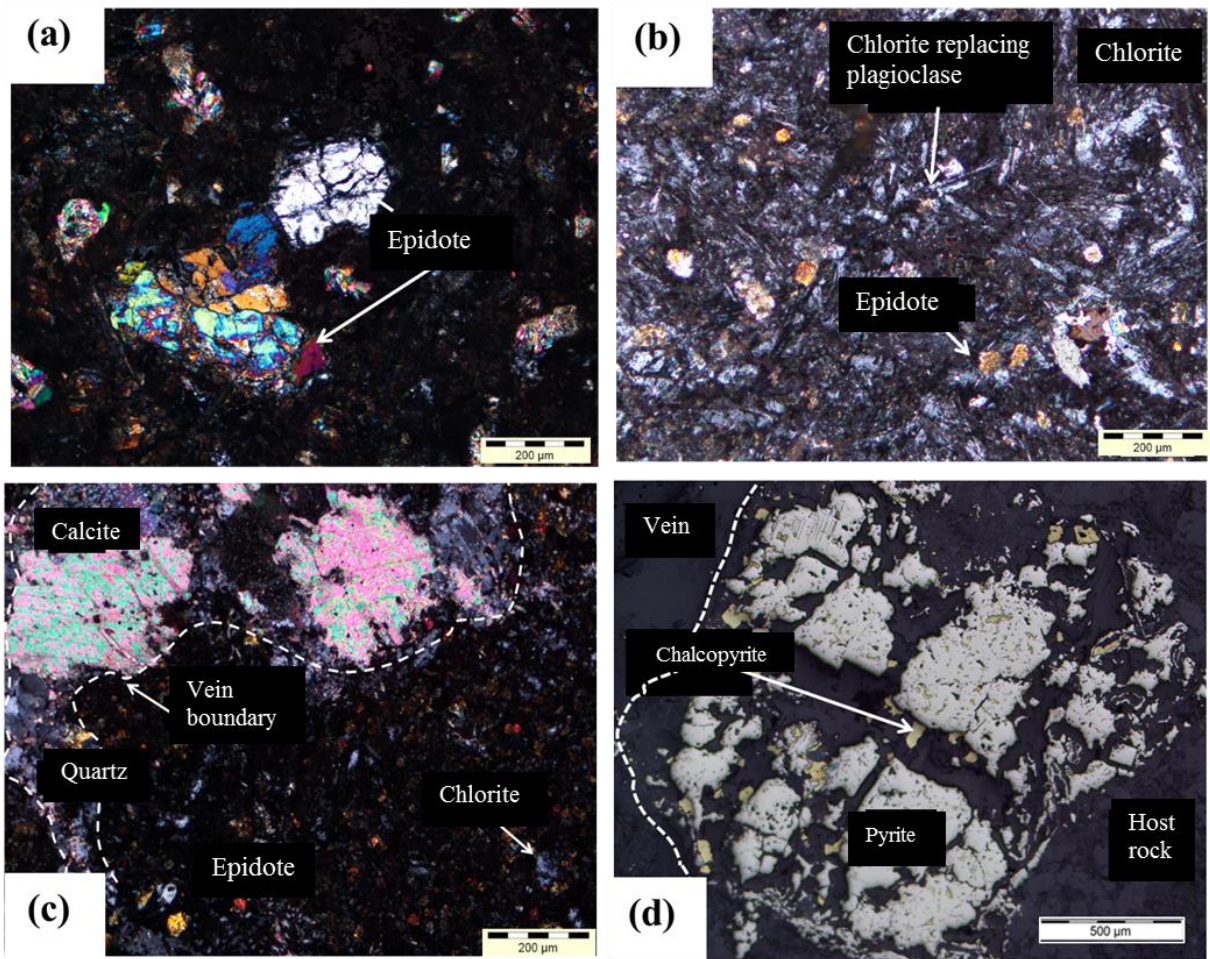


Figure 5.3. (a) Photomicrograph of a medium-grained basalt composed of metamorphic mineralogy. The image exhibits well-formed, < 3.5 mm epidote crystals surrounded by a fine-grained epidote and chlorite (Sample G12-02-096; UTM 30P 694686; 1443104; cross polarized light). (b) Photomicrograph of a basalt that displays plagioclase with an overprint of epidote and chlorite. Plagioclase is partly replaced by chlorite, but retains its lath-like shape, is randomly oriented and exhibits albite twinning (Sample G12-02-095; UTM 30P 695421; 1443258). (c) Photomicrograph of basalt that is crosscut by a quartz-calcite vein. The basalt is altered to chlorite-epidote but retains minor primary plagioclase microlites. The vein crosscuts both primary and secondary mineralogies indicating it formed syn- or post-alteration. (Sample G12-02-095; cross polarized light). (d) Photomicrograph of pyrite and chalcopyrite in a vein that crosscuts basalt (Sample G12-02-096; UTM 30P 694686; 1443104; Reflected-light). The texture indicates that sulphide mineralization is synchronous to, or postdates emplacement of the basalt sequence.

5.2. Metasedimentary rocks

5.2.1. Volcanogenic greywacke

Polylithic, poorly sorted greywacke exhibits a range of grain sizes from 0.1-4.0 mm. It contains angular to sub-rounded clasts and fragments. The dominant mineralogy includes angular to sub-angular clinopyroxene, quartz and plagioclase grains as well as rounded to sub-rounded chert clasts. The clinopyroxene grains occasionally display twinning, which has also been reported for clinopyroxene grains in greywacke sequences of the Oudalan-Gorouol volcano-sedimentary belt (Peters, 2011).

Plagioclase grains in the greywackes of the study area vary in size between 2 and 4 mm, are elongate and display albite twinning. Relic twins were noted in the larger grains as the plagioclase has

undergone deuterian alteration. The matrix makes up approximately 25 % of the rock. The matrix is composed of fine to medium-grained polycrystalline quartz and chert (Figure 5.4a). The presence of non-detrital chlorite and epidote in the matrix, associated with epidote replacement of clinopyroxene grains, indicates greenschist facies metamorphism, post-deposition (Nesse, 2000). Sericite and polycrystalline quartz occur as an alteration texture. Approximately 15% of the quartz observed is secondary, as shown by quartz veins and interstitial grains with poorly to non-visible grain boundaries. The secondary quartz constitutes a high proportion of the quartz observed in the matrix. Approximately 5% of the modal abundance of the greywacke is composed of fine-grained, disseminated pyrite, chalcopyrite, ilmenite and magnetite.

5.2.2. *Pyroclastic breccia*

Petrographic study of the pyroclastic breccia confirm that it is a polyolithic, coarse-grained unit dominated by a mineral assemblage of angular to sub-angular quartz, euhedral plagioclase, hornblende, anhedral clinopyroxene, ilmenite and magnetite, with disseminated iron sulphides. Rounded to sub-rounded chert clasts are also present in the breccia.

The quartz clasts range in size from 0.5-4.0 mm (Figure 5.4b, c). Chert clasts are wholly composed of microcrystalline aggregates of quartz. Plagioclase exhibits a range of sizes from 2-4 mm and is deuterically altered, but exhibits relict albite twinning. Crystals of volcanic hornblende (2-4 mm in length) are brown, euhedral and zoned (Figure 5.4d), and present well-developed cleavage planes. The hornblende constitutes approximately 15 % of the modal abundance of the breccia.

The matrix of the pyroclastic breccia is composed of sericite, chlorite, epidote and carbonate and fine-grained quartz and plagioclase crystals. Approximately 25-30 % of the modal abundance of the pyroclastic breccia is composed of matrix. Polycrystalline aggregates of secondary quartz are also observed within the matrix and make up approximately 35% of the fine-grained, interstitial mineralogy.

5.2.3. *Mn-Fe-rich carbonaceous sedimentary rocks*

Mn-Fe-rich carbonaceous sedimentary rocks are composed of braunite, magnetite, ilmenite hematite, graphite, disseminated pyrite and chalcopyrite, and 0.01-0.2 mm interstitial quartz grains. Braunite occurs as breccia, tablets and colloform textures (Figure 5.5a). Braunite is also vein-hosted.

Hematite is observed as anastomosing veins that crosscut the host rock (Figure 5.5b) and ilmenite and magnetite occur as veins and disseminations (Figure 5.5c). In reflected light, disseminated pyrite and chalcopyrite makes up approximately 2 % of the modal abundance of the Mn-Fe-rich carbonaceous samples. Micron-scale grains of gold are disseminated through the rocks. Quartz-carbonate veins and stockwork breccias crosscut these mineralogies (Figure 5.5d). A second phase of quartz veining crosscuts the pre-existing textures.

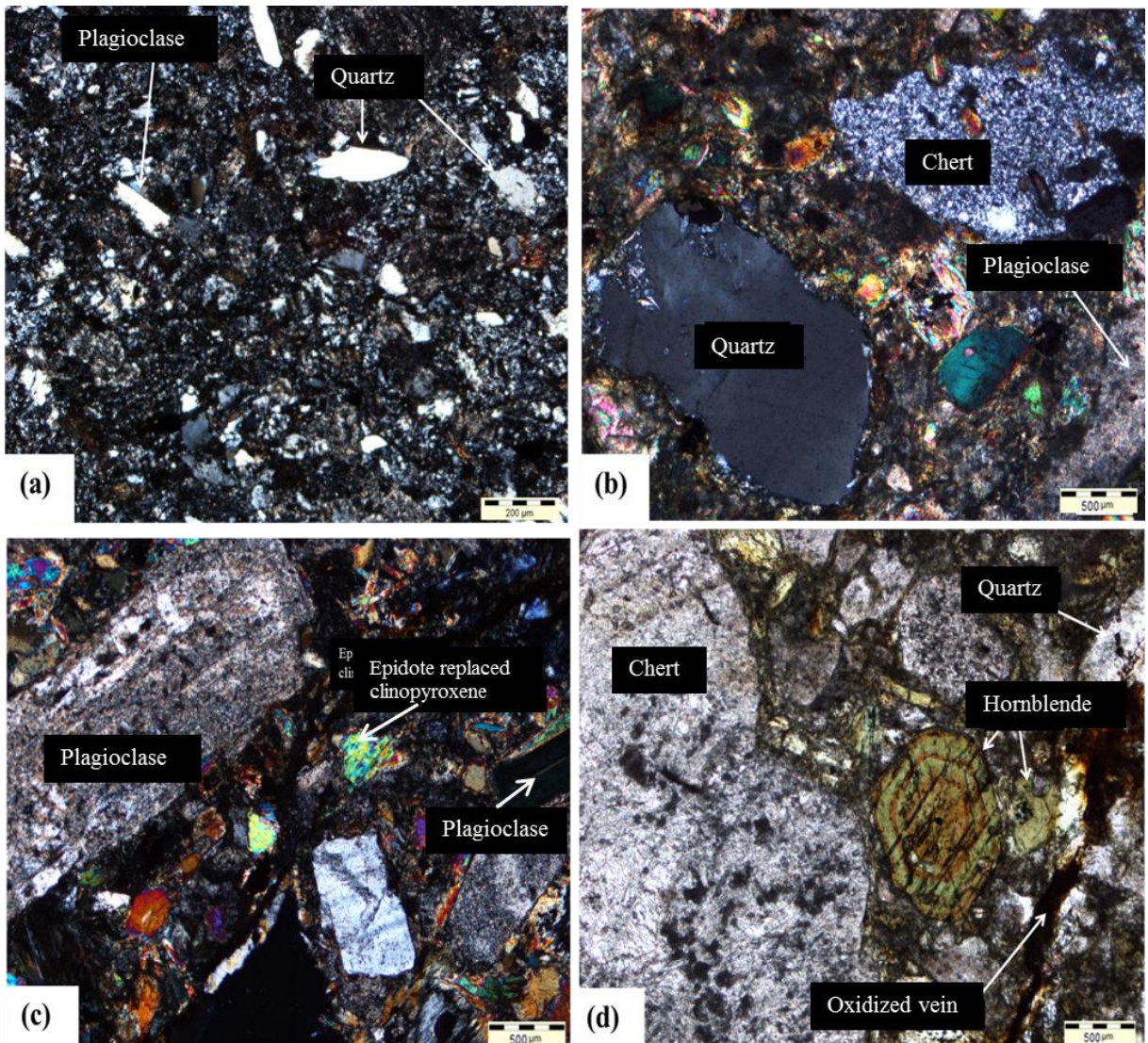


Figure 5.4. (a) Photomicrographs of a coarse-grained, poorly sorted, chlorite-rich volcanogenic greywacke. The sample is composed of quartz, plagioclase (> 2mm), lithic chert clasts, and biotite (Sample G12-007; 696828; 1443986). (b, c) Photomicrographs of pyroclastic breccia containing euhedral, coarse-grained (> 1mm) plagioclase, chert, quartz and fine-grained (< 0.5mm) epidote replacing clinopyroxene and hornblende. The matrix is interpreted to be composed of ash-lapilli sized fragments that are altered to epidote and chlorite (Sample G12-02-126; UTM 30P 709365; 1424791, cross polarized light). (d) Photomicrograph of pyroclastic breccia that is composed of euhedral, coarse-grained (> 1 mm), zoned, volcanic hornblende, with well-defined cleavage, and l> 2 mm sub-rounded chert clasts and sub-angular quartz grains (Sample G12-02-126; UTM 30P 709365; 1424791, plane polarized light).

5.3. Intrusions

5.3.1. Mafic dykes and sills

Seven samples of mafic dykes or sills were examined petrographically in this study. Based on their mineralogy they were grouped into:-

- (1) Dolerite - composition was determined for four samples; on average, the dolerite intrusions are composed of 45% clinopyroxene and 45% plagioclase. Accessory minerals include biotite and muscovite, comprising approximately 5-10% of the modal abundance. Sample G12-02-036, which is

composed of plagioclase-clinopyroxene-hornblende-orthopyroxene, is composed of 15-20% hornblende. It can (effectively) be classified as a hornblende-rich dyke similar in composition to dolerite. The sample exhibits intrusive textures such as K-feldspar exsolution lamellae within euhedral plagioclase crystals and exsolution between clinopyroxene and orthopyroxene crystals, as shown by orthopyroxene lamellae.

(2) Feldspathic pyroxenite - composition was determined for two samples. The samples have higher proportions of clinopyroxene (approximately 60-65 %) and less plagioclase than the dolerite samples. Accessory minerals include biotite and muscovite comprising approximately 5-10% of the modal abundance.

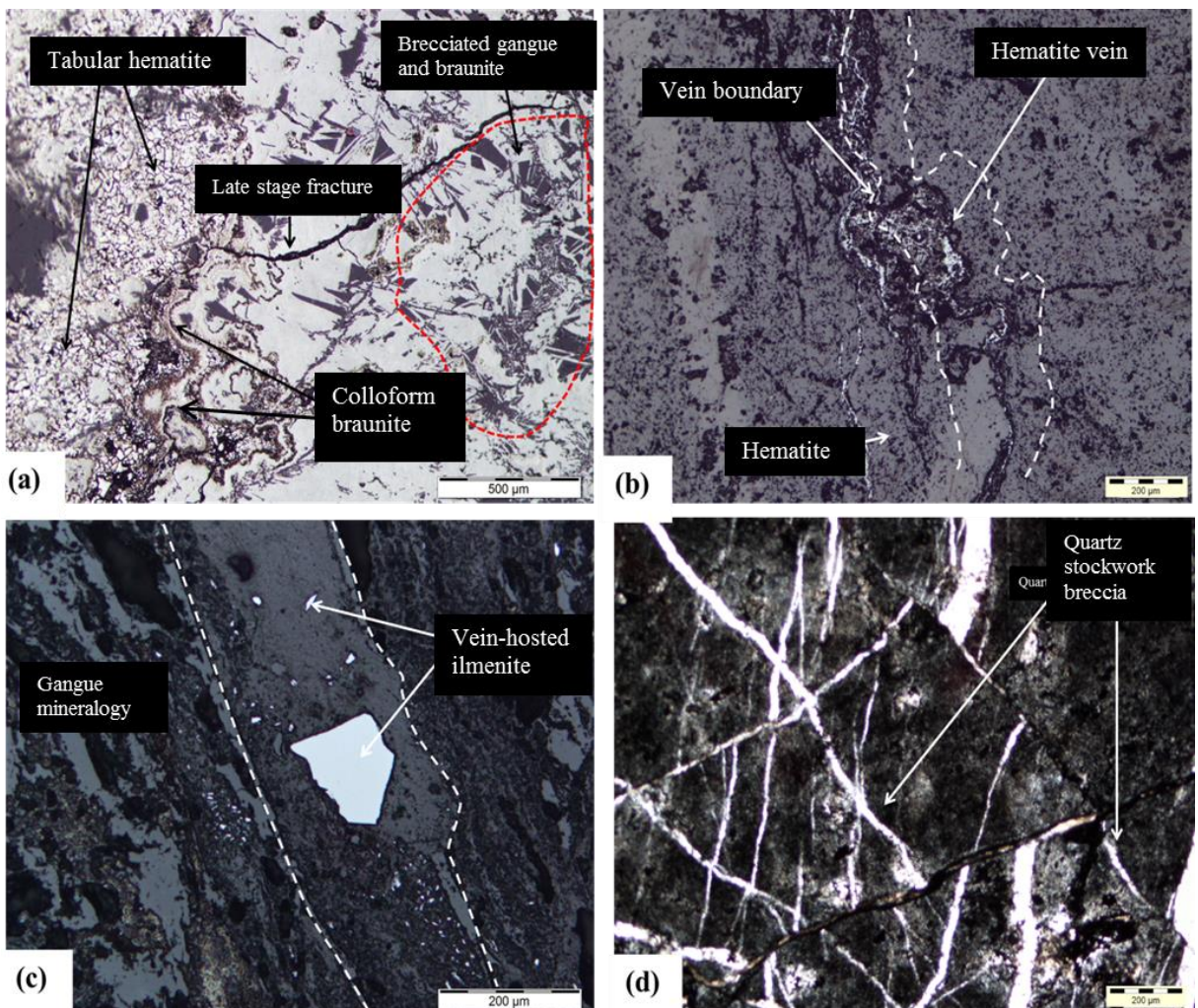


Figure 5.5. (a) Photomicrograph of tabular, colloform and brecciated braunite from a Mn-Fe-rich unit (Sample G12-004; UTM 30P 702744; 1446079, reflected light). The three textures of braunite suggest different growth phases. Late stage fractures cross-cut brecciated braunite and terminate against the tabular braunite indicating that tabular braunite developed after the colloform texture braunite. (b) Photomicrograph of a Mn-Fe-rich, carbonaceous unit which is crosscut by anastomosing hematite veins (Sample G12-02-080; UTM 30P 703512; 1444037, reflected light). (c) Photomicrograph of a Mn-Fe-rich unit that are crosscut by ilmenite-bearing veins. The ilmenite, in this case, is interpreted as a secondary phase because it is vein-hosted in the rocks (Sample G12-02-35; UTM 30P 707346; 1425026, reflected light). (d) Photomicrograph of a Mn-Fe carbonaceous unit that is crosscut by stockwork quartz ± ankerite veins. The rock is altered to hematite, ilmenite, magnetite and secondary quartz (sample G12-017; UTM 30P 677996; 1466647, plane polarized light).

(3) Pyroxenite - composition is determined for one sample. The dyke\sill is dominated by clinopyroxene (greater than 75%) with minor orthopyroxene. The plagioclase modal proportion for this sample is between 15 and 20%.

Clinopyroxene is the dominant mineral in the mafic suite; it exhibits twinning and low to moderate alteration. The clinopyroxene crystals are subhedral in shape and range in size from 1.0-3.5 mm.

Sulphides are present in all samples. Pyrite, chalcopyrite and bornite are disseminated throughout the rocks and typically constitute an approximately 1 % modal abundance. However, chalcostibite occurs with chalcopyrite intergrowths within Sample G12-02-122 (Figure 5.6a). The chalcostibite has a modal abundance of 10 % and measures between 2 and 5 mm in size. The sulphide is characterized by triangular pits, a moderate reflection and a soft texture as shown by scratch and pit marks on the polished surface.

5.3.2. Aplitic dykes

Aplitic dykes in the study area contain plagioclase, quartz, orthoclase and microcline, with accessory biotite and muscovite (Figure. 5.6b). Carlsbad twinning is present in the orthoclase crystals, but is not present in all grains. Cu-bearing sulphides occur on the margins and within biotite crystals, indicating a preferential relationship between the sulphides and biotite. They make up approximately 0.5-1.0 % of the modal abundance of the rocks.

Textures included (1) exsolution between orthoclase and plagioclase, evident as globular lamellae, (2) myrmekitic texture which is represented as intergrowths between quartz and plagioclase, and (3) poikilitic texture, is observed as fine-grained muscovite and biotite enclosed within larger quartz and orthoclase crystals.

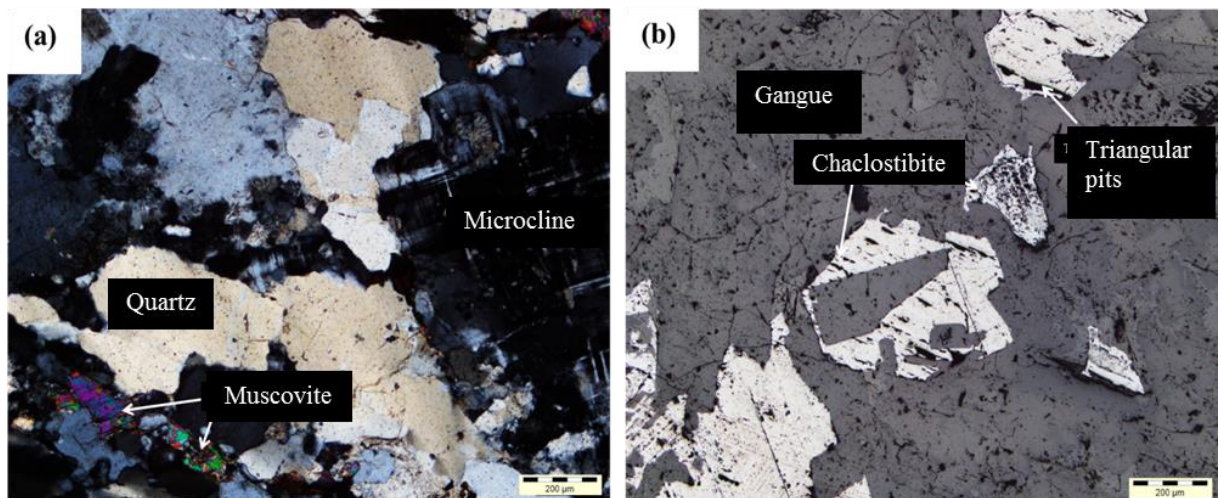


Figure 5.6. (a) Photomicrograph of an aplite dyke, which is composed of medium to coarse microcline and quartz, with subordinate muscovite. The mineralogy is unaltered (Sample G12-02-114; UTM 30P 711540; 1432977, cross polarized light). (b) Photomicrograph of a chalcostibite in dolerite. Chalcostibite forms large, disseminated crystals. The chalcostibite crystals are soft (shown by scratches), contain triangular pits, and have a moderate reflectivity (Sample G12-02-122; UTM 30P 709363; 1425384, reflected light).

6. GEOCHEMICAL ANALYSIS OF THE GOREN BELT

6.1. Geochemistry of the volcanic rocks

Whole-rock analyses were completed on 20 volcanic and 6 sedimentary samples using XRF and ICP-MS. Both major elements and trace elements were measured using XRF spectrometry. The data were calculated in wt% for the major elements and parts per million (ppm) for the trace elements. The ICP-MS analyses are reported in ppm. A variety of geochemical methods was used in attempt to classify the samples in order to characterize the tectonic setting for volcanic rocks of the GB.

Geochemical data for volcanic rocks from the Boromo and Houndé belts, Oudalan-Gorouol belt and Tiebélé belt were used in a comparative study of volcanic units across several different belts in Burkina Faso. Data from Baratoux et al. (2011) include 7 tholeiitic basalt samples and 6 calc-alkaline volcanic samples that were reported for the Boromo and Houndé belts in western Burkina Faso. Data from Ilboudo (2010) were reported for the Tiebélé region in the south of the country. Tshibubudze and Hein (2013) reported data for two meta-volcanic samples (major-elements only) from the Oudalan-Gorouol belt (OGB) in the northeast of Burkina Faso.

The volcanic rocks of the GB have undergone variable metamorphism, varying from sub-greenschist to amphibolite facies (Kříbek et al., 2008). The rocks are also variably silicified. Increased silica was taken into account by determining its abundance through field and petrographic observation when interpreting the geochemistry by measuring relationships between chemical variables, using the correlation coefficient (r).

The alteration of the rocks indicates that HFSE such as Ta, Nb, Ce, P, Zr, Hf, Sm, Ti, Y are immobile during greenschist facies metamorphism (Pearce, 1983; Saunders and Tarney, 1984; Rollinson, 1993). In general, Th is considered to be less mobile, but not to the extent of the HFSE. Large ion lithophile elements (LILE) such as Rb, Sr and Ba are normally significantly mobile during alteration and greenschist facies conditions. Due to the immobility of HFSE, it was not likely that correlations resulted from secondary alteration processes, but rather reflected the true nature of the primary chemistry of the rocks.

6.1.1. Major element geochemistry

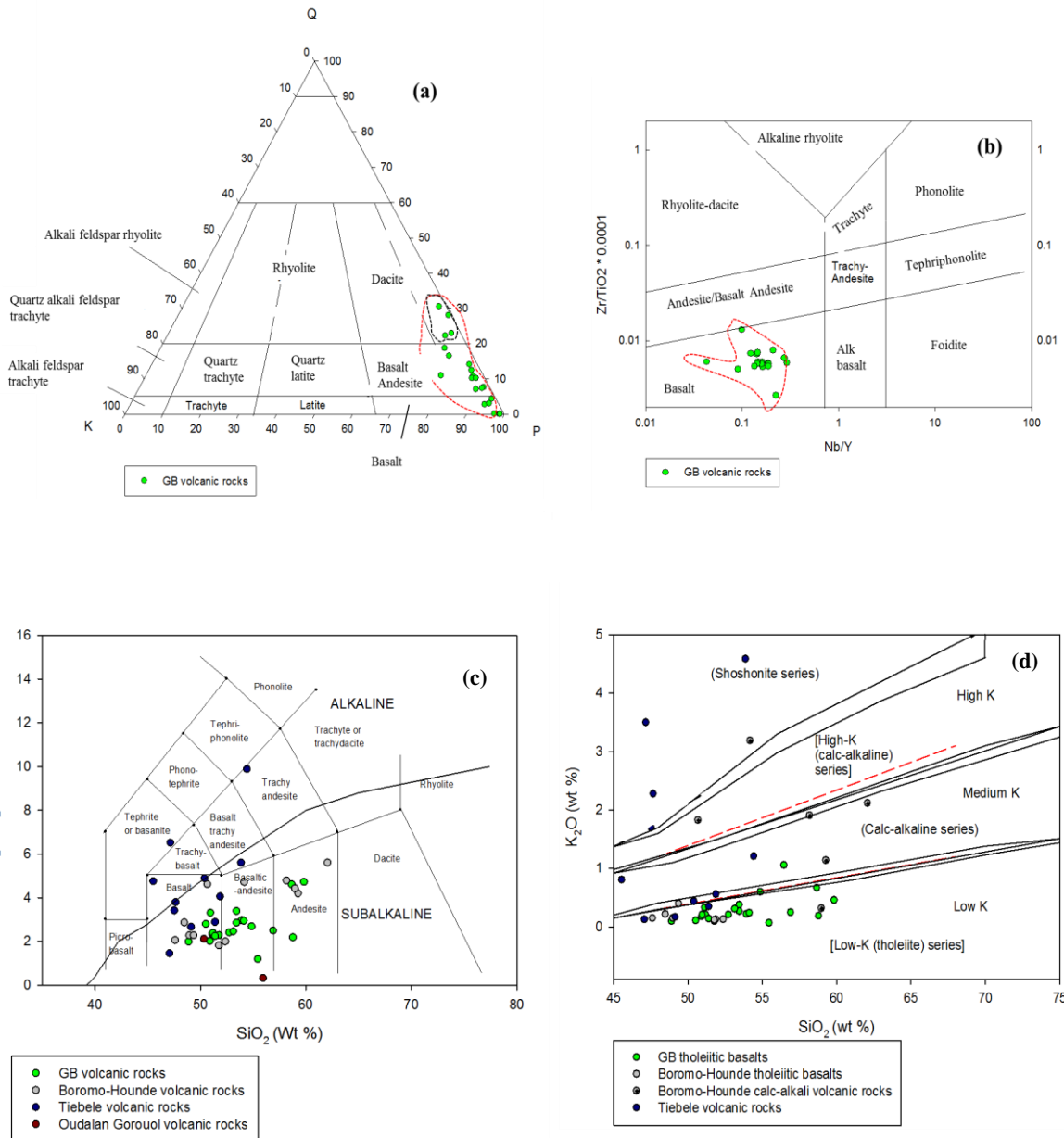
The XRF data (Appendix C) for selected samples of volcanic rocks from the GB yield a SiO_2 range between 48.92 and 59.86 wt %. MgO values varied from 3.31 to 8.16 wt %, while the $\text{Mg} \#$ ranges from 31.64-57.52 and has an average value of 45.77. Al_2O_3 ranges from 10.65 to 15.59 wt %. The sum of Na_2O and K_2O generally equals less than 4 wt%. The FeO content ranges from 10.24 to 14.57 wt% and P_2O_5 values are between 0.07 and 0.21. Using these data, a number of classification diagrams (Figures 6.3a - e) were used to establish the type of volcanic rocks that make up the southern GB.

Major elements have likely been affected by alteration, thus making any interpretations based on them less reliable. However, analyses can still be done, albeit with caution. Mineral abundances from CIPW norms were plotted on a Streckeisen classification diagram (Streckeisen, 1976) for volcanic rocks (Figure 6.1a). The data resolves a trend from the basalt field towards the dacite field with increasing silica content and a minor increase in K, which is interpreted to be the result of potassium mobility during alteration, such as silicification. The overall data trend observed is thus not surprising, particularly because the rocks have been silicified. Further to this, it is important to note that the Streckeisen classification diagram, when plotted using the CIPW norm, is not able to distinguish between primary and secondary minerals, in this case quartz. Confirmation of secondary silica was therefore determined by petrographic analyses of the samples (Chapter 5).

A classification diagram using the immobile element ratios of Nb/Y plotted against $Zr/TiO_2 \times 0.0001$ after Winchester and Floyd (1976) was plotted for the GB volcanic rocks (Figure 6.1b). The samples plot well within the basalt field with the exception of Sample G12-02-126, which straddles the boundary between the basalt and basaltic andesite fields.

A total alkalis versus silica (TAS) diagram (after Le Maitre et al., 1989) plots samples within the basalt, basaltic andesite and andesite fields (Figure 6.1c). The TAS diagram indicates that the rocks are sub-alkaline (tholeiitic) in composition. A comparison of the GB samples with the Boromo-Houndé volcanics reported by Baratoux et al. (2011), Tiebélé volcanics reported by Ilboudo (2010) and 2 samples from the OGB reported by Tshibubudze and Hein (2013) indicates that most samples plot within the basalt and basaltic andesite field. The samples range from 45.5 to 55.9 SiO₂ (wt%) with the lowest SiO₂ concentration sampled from the Tiebélé region and the highest from the GB. Some samples from Tiebélé and Boromo-Houndé belts show higher Na₂O+K₂O (wt%) when compared to the GB volcanics. The OGB samples show a relatively large difference in SiO₂. Sample BF_1366, in particular reported little Na₂O+K₂O (~ 0.2 wt %). The Boromo-Houndé volcanics plot on a trend from basalt to andesite as the SiO₂ and Na₂O+K₂O increased. The Tiebélé samples (HTPILL and HTBA), which had been classified as basaltic rocks by Ilboudo (2010), show high Na₂O+K₂O values (up to ~6 and 10 wt%) and plot as tephrite/basanite and trachyandesite, respectively. Sample HTGOGO from the Tiebélé region, plots as an alkaline volcanic rock in the basalt field. The highest K₂O+Na₂O value from the Tiebélé samples is 9.86 wt%. The GB samples show a maximum K₂O+Na₂O value of 4.7 wt%.

A further sub-division of sub-alkalic rocks is shown using SiO₂ versus K₂O in wt% in Figure 6.1d. Le Maitre et al. (1989) originally compiled this diagram. It plots almost all the GB data points within the Low-K field, which is defined as tholeiitic in composition.



(Caption overleaf)

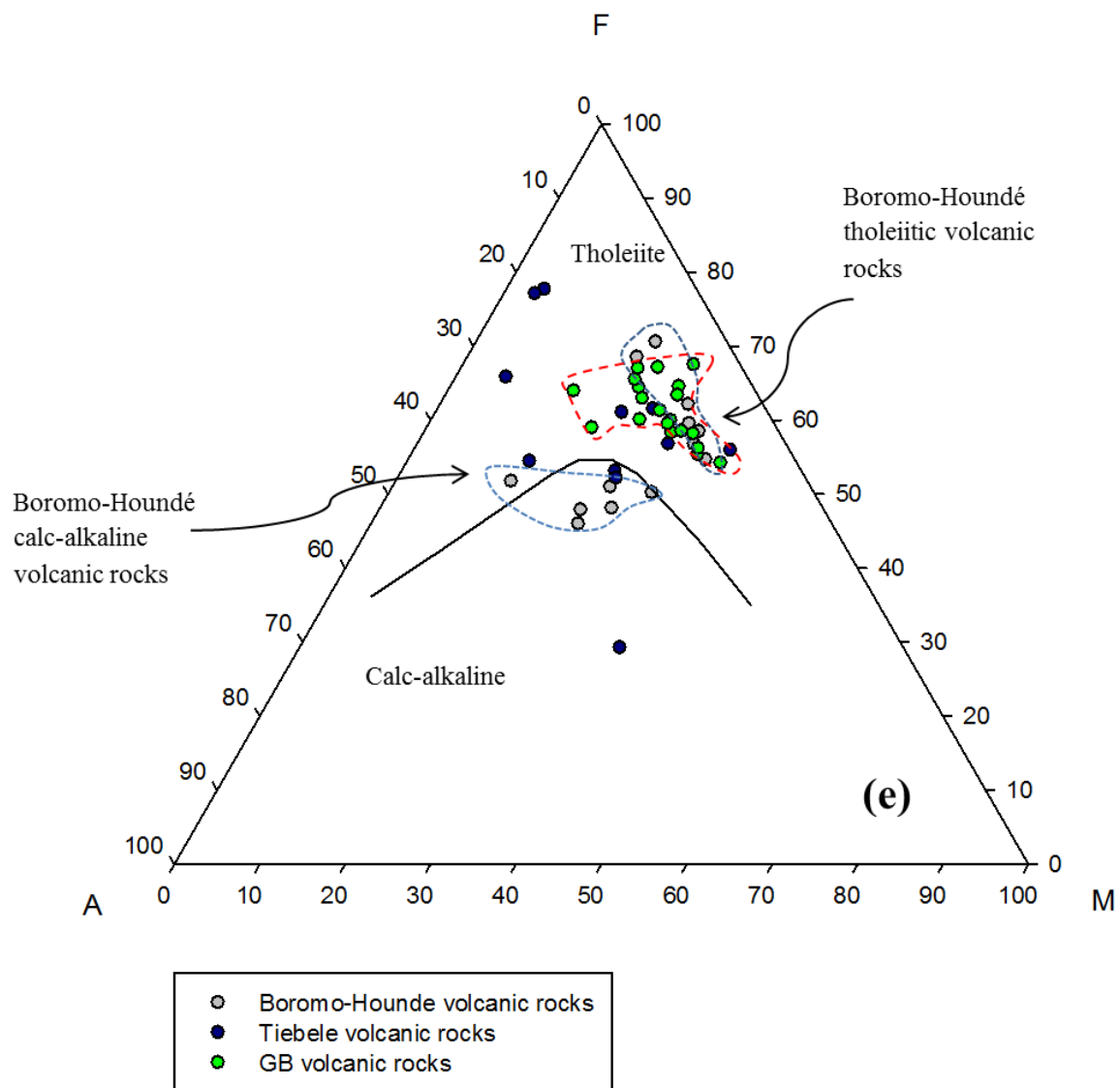


Figure 6.1. (a) Streckeisen classification diagram for volcanic rocks plots the rocks from the GB as basalts, basalt-andesite to dacite in composition. The samples that indicate dacitic composition contain increased secondary silica, interpreted to be a result of silicification. (b) Nb/Y versus $Zr/TiO_2 \times 0.0001$ diagram (after Winchester and Floyd, 1976). The GB volcanic rocks generally plot in the basalt field. (c) Le Maitre's classification for volcanic rocks. The GB rocks plot within the basalt, basaltic-andesite and andesite fields. Samples from the Boromo-Houndé belts are distributed throughout the basalt, basaltic-andesite and andesite fields. The Tiebélé samples have a smaller SiO_2 range but some samples contain increased alkali concentrations and plot as trachyandesite and tephrite. The Oudalan-Gorouol belt samples plot between basalt and basaltic-andesite. (d) SiO_2 versus K_2O (wt%) demonstrates that the GB volcanic rocks plot within the Low-K series for the most part. One sample plots in the Medium-K series with a K_2O value of ~1 wt%. Samples from the Boromo-Houndé belts plot within the Low-K series as well as the calc-alkaline fields (Medium-K, High-K series and the Shoshonite series). The Tiebélé samples vary between the different fields. (e) The AFM diagram plots samples from various locations. The GB volcanic rocks plot in the tholeiitic phase whereas the Boromo-Houndé samples are split between tholeiitic and calc-alkaline compositions which agrees with classifications made by Baratoux et al. (2011). The Tiebélé samples are also distributed between calc-alkaline and tholeiitic compositions.

The Boromo-Houndé and Tiebélé basaltic rocks were also plotted in Figure 6.1d. The highest silica content for all the samples was less than 65 wt% SiO₂. The maximum K₂O value was approximately 4.5 wt%. Half of the Boromo-Houndé samples plot in the Low-K series together with the GB samples. The remaining samples, originally defined as calc-alkaline basalt and andesite by Baratoux et al. (2011), plot in the calc-alkaline fields, including the Medium-K, High-K and Shoshonitic fields. Less than half of the Tiebélé basalts plot in the Low-K field, while the rest plot within the Medium-K and Shoshonite series. This indicates both tholeiitic and calc-alkaline compositions for all the samples plotted.

The samples from the GB were plotted on an AFM diagram. AFM diagrams can have their limitations, including their petrogenetic information. This is due to the components that make up the trivariate diagram that collectively make up less than half of the potential chemical constituents of a rock. In addition, because data are normalised to 100 % in order to plot on a ternary diagram, distortions can occur to a certain degree (Rollinson, 1993). These elements are also prone to alteration, therefore alteration is a cause for distortion.

However, the AFM diagram presented in Figure 6.1e plots all samples from the GB in the tholeiitic series. The data plots above the calculated boundary between tholeiitic and calc-alkaline series (Irvine and Baragar, 1971). Besides a few outliers, a trend from MgO toward FeO_{total} was resolved for the GB samples. The comparative data from Boromo-Houndé and Tiebélé belts primarily plot within the tholeiitic series, but samples from both regions do show calc-alkaline compositions. This was observed by data plotting below the calc-alkaline-tholeiitic boundary. A trend from MgO toward FeO_{total} was resolved for the Boromo-Houndé tholeiitic basalts, which plot in the tholeiite field. The Tiebélé samples did not resolve a trend possibly due to the limited sample suite analysed by Ilboudo (2010). They were scattered throughout the calc-alkaline and tholeiitic fields.

Harker diagrams were plotted for samples from the GB. They are summarized according to trends observed. MgO was used on the x-axis rather than SiO₂ because the range of MgO in mafic volcanic rocks is much less than SiO₂, avoiding the effect of distortion. In addition, the amount of silica represented was not considered reliable, due to silicification of the GB samples. MgO is accepted to be relatively more immobile than SiO₂ (Rollinson, 1993) and therefore able to provide an relatively accurate representation of the original MgO wt% of the rocks. MgO was plotted against TiO₂, P₂O₅, SiO₂, Al₂O₃, Na₂O, CaO, FeO, NiO, Cr₂O₃ and K₂O (Figure 6.2 a-j). Both increasing and decreasing oxide trends are interpreted to represent periods of mineral crystallization, and termination of crystallization.

Some trends resolved on the Harker diagrams exhibit better correlations than others. The MgO-NiO plot resolv a trend line in which NiO decreases with MgO (Figure 6.2a). This was interpreted to be the result of the crystallization of clinopyroxene, which consumed Ni, thus removing it from the melt to the crystal structure. The slight shallowing of the NiO-MgO trend line is probably due to the end of clinopyroxene crystallization.

The MgO-Cr₂O₃ plot (Figure 6.2b) resolved a similar trend to Figure 6.2a, and Cr₂O₃ decreases in wt% as MgO decreases. The decrease of Cr₂O₃ is interpreted to be the result of crystallization of

spinel and clinopyroxene, because Cr can occupy part of the clinopyroxene crystal lattice. The trend shallows, indicating less Cr was used-up, caused by a decrease or halt in spinel and clinopyroxene crystallization.

The MgO-CaO and MgO-Al₂O₃ plots exhibit directly proportional trends as the magma evolved (Figure 6.2c-d), i.e., proportional depletion in MgO, CaO and Al₂O₃. Ca is a constituent of anorthite, whereas Al occurs across the solid solution spectrum of plagioclase. Ca is generally a constituent of apatite in basalt; due to its continuous decrease during crystallization Ca can be accommodated in the crystal structure of apatite in the later stages of basalt evolution. However, apatite was not observed during petrographic analyses (Chapter 5) and thus it was interpreted that the decrease in CaO and Al₂O₃ was the result of plagioclase crystallization.

MgO-SiO₂ and MgO-TiO₂ plots resolve similar trends (Figure 6.2e-f). At high MgO values, there are low concentrations of SiO₂ and TiO₂. As the melt began to crystallise, the concentration of SiO₂ and TiO₂ increased. Ti is regarded as being incompatible (Rollinson, 1993) and therefore preferentially remains in the liquid rather than partitioning into a crystal. Ti thus increases during the crystallization process. However, at some stage, TiO₂ will crystallise within oxide minerals such as rutile and ilmenite, which are common oxides in basalts.

The MgO-Na₂O plot (Figure 6.2g) displays the Na₂O concentration increasing with respect to MgO. This is interpreted to be the result of the crystallization of the Na-rich end-members of plagioclase, i.e., albite. Albite tends to crystallise at lower temperatures compared to the Ca-rich anorthite (Orville, 1972); however, it is evident from the trend that most Na₂O would have remained in the liquid. The MgO-P₂O₅ plot also resolves an increasing trend as MgO decreased (Figure 6.2h). This indicates that phosphate minerals did not crystallise in any significant way. The MgO-FeO plot (Figure 6.2i) resolves an increasing FeO trend, which is typical of a liquid in which MgO fractionates first. The K₂O-MgO plot (Figure 6.2j) illustrates a poor correlation, where data points shows as a scatter.

6.1.2. Trace element geochemistry

Multi-element diagrams were used to compare the GB tholeiitic basalt samples to regional volcanic units (Figure 6.3a). The samples from the GB were normalised to chondrites (Anders and Grevesse, 1989) and plotted in an elemental array after Baratoux et al. (2011). The tholeiitic basalt samples from the GB show similar element concentrations, exhibited by parallel plots and similar magnitudes. This indicates comparable trace element behaviour. A negative Ti anomaly was observed for every sample. Rb also shows low values, particularly for the GB and Boromo-Houndé samples. The Tiebélé basalt samples show low Rb values, but not as low as the other two sample regions. It is unlikely that the negative Rb values are caused by distortion, as a result of its position on the x-axis because it was plotted adjacent to Ba, which contains similar ionic properties. Thus Rb is probably low due its mobility during alteration.

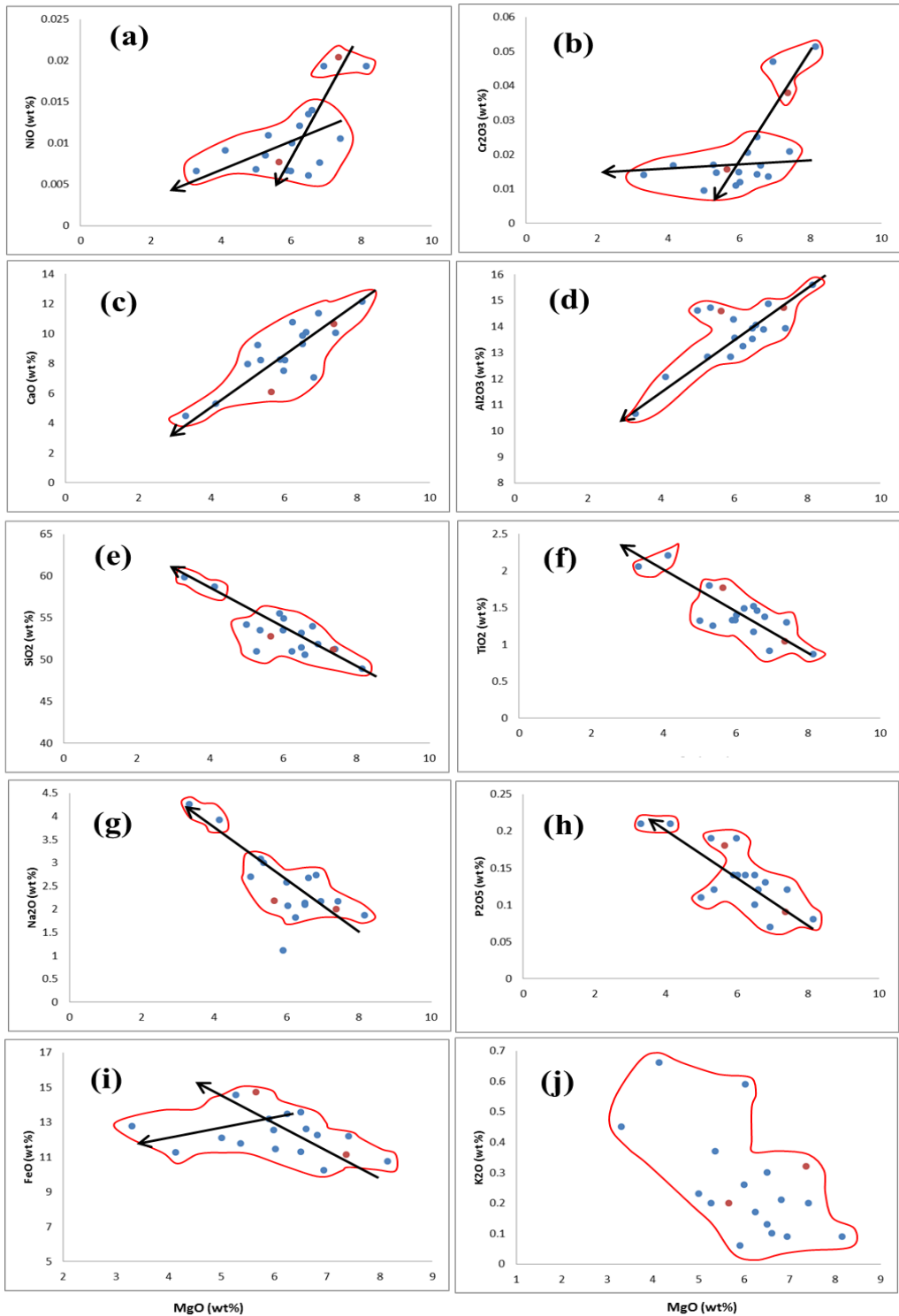


Figure 6.2. Harker diagrams exhibiting crystallization trends of major elements for the GB volcanic rocks. Red dots=more deformed samples; blue dots=less deformed samples (a) The MgO - NiO plot resolves a trend line in which NiO decreases with MgO . This suggests the crystallization of clinopyroxene occurred, which consumed Ni thus removing it from the melt to the crystal structure. The slight shallowing of the NiO - MgO trend line is due to the closure of clinopyroxene crystallization (b) The MgO - Cr_2O_3 plot resolves a similar trend in which Cr_2O_3 decreases in wt% as MgO decreases. The decrease of Cr_2O_3 is credited to the crystallization of spinel and clinopyroxene. The trend shallows, indicating less Cr was used up, caused by a decrease or halt in spinel and clinopyroxene crystallization (c, d) The MgO - CaO and MgO - Al_2O_3 plots exhibit directly proportional trends. As MgO decreases, it was interpreted that CaO and Al_2O_3 decrease as plagioclase crystallized (e, f) MgO - SiO_2 and MgO - TiO_2 plots resolve similar trends. At high MgO values, there are low concentrations of SiO_2 and TiO_2 . As the melt began to evolve and fractionate, the concentration of SiO_2 and TiO_2 increase. TiO_2 will crystallize and form oxide minerals such as rutile and ilmenite (g) The MgO - Na_2O plot displays the Na_2O concentration increasing slowly as MgO concentration remained high. As the MgO concentration began to decrease, the Na_2O concentration rapidly increases. This

can be explained by the crystallization of the Na-rich end-members of plagioclase, towards the end of crystallization (h) The MgO-P₂O₅ plot also resolves an increasing trend as MgO decreases, suggesting phosphorus did not crystallise (i) The MgO-FeO plot resolves an increasing FeO trend. It would be expected at some point in the fractionation process for Fe to partition into Fe-oxide minerals, explaining the decrease in FeO concentrations. (j) K₂O versus MgO shows a poor correlation.

A clearer difference is observed when comparing the tholeiitic basalts from the GB and the calc-alkaline volcanic rocks of the Boromo-Houndé belts (Figure 6.3b). The calc-alkaline rocks report an enrichment of 1-2 orders of magnitude in Rb, Ba, Th, U, relative to the GB tholeiitic basalts. Despite this difference, Rb still displays proportionally lower values compared to Ba in both sample suites. On the x-axis, between Hf and Gd, there is no relative enrichment or depletion. Toward the HFS elements, the Boromo-Houndé samples exhibit slight depletions relative to the GB tholeiitic basalts. Overall, the calc-alkaline rocks from the Boromo-Houndé belts report a decreasing trend from Rb toward Lu. A negative Ti anomaly is again evident in all samples. Chondrite-normalised multi-element diagrams were plotted with a different elemental array (after Rollinson, 1993) on the x-axis (Figure 6.4a). Samples of tholeiitic basalt from the GB, Boromo-Houndé and the Tiebélé belts were compared. With this chemical array, the tholeiitic basalts report relatively similar element abundances, as revealed by their parallel patterns and minimal differences in magnitude between samples. Rb is plotted adjacent to Ba and displays a large negative anomaly, as do P and Ti. The normalised P values for the sample suites range between 0.5 and 0.03. The calc-alkaline rocks show an overall decreasing trend from left to right on the multi-element diagram (Figure 6.4b). The GB basalt samples show an overall flat trend, with the exception of the anomalies present. A primitive-mantle normalised multi-element diagram was plotted for the GB volcanic rocks (Figure 6.4c). The graph also shows a clear negative P anomaly. The chemical array used on the graph was taken after McCuaig et al. (1994). An N-type MORB normalised (Tarney et al., 1981) multi-element diagram is presented in Figure 6.5a. The elemental array represents a transition from LIL to HFS elements, from left to right. The LILE of the GB samples are slightly more enriched than average N-type MORB compositions. The HFSE are similar to MORB values, with Y having a significant negative anomaly. Cr shows scattered values, varying from near N-type MORB concentrations to values an order of magnitude lower. There is an overall decreasing trend from the LILE to HFSE. The non-normalised Y values of the GB samples (see Appendix C) are, on average, one third of the normalising factor for N-type MORBs. Therefore, the Y anomaly is not considered to be an effect of distortion. Ta and P were removed from the plot for the GB samples because they resolve large positive and large negative anomalies, respectively. Such anomalies are reported by Saunders and Tarney (1984) and Väisänen and Westerlund (2007) for tholeiitic basalts from modern back-arc and Palaeoproterozoic terranes in Finland. Tectonic environments can in some cases be deduced by HFSE concentrations such as Ti, Ta and Nb. The calc-alkaline rocks from the Boromo-Houndé belts were plotted against the GB samples, while still normalised to N-MORB (Figure 6.5b). Enrichment in Rb, Ba and Th was noted relative to the GB samples, as well as negative Ti and P anomalies. The calc-alkaline samples from the Boromo-Houndé belts did not show Nb or Ta anomalies.

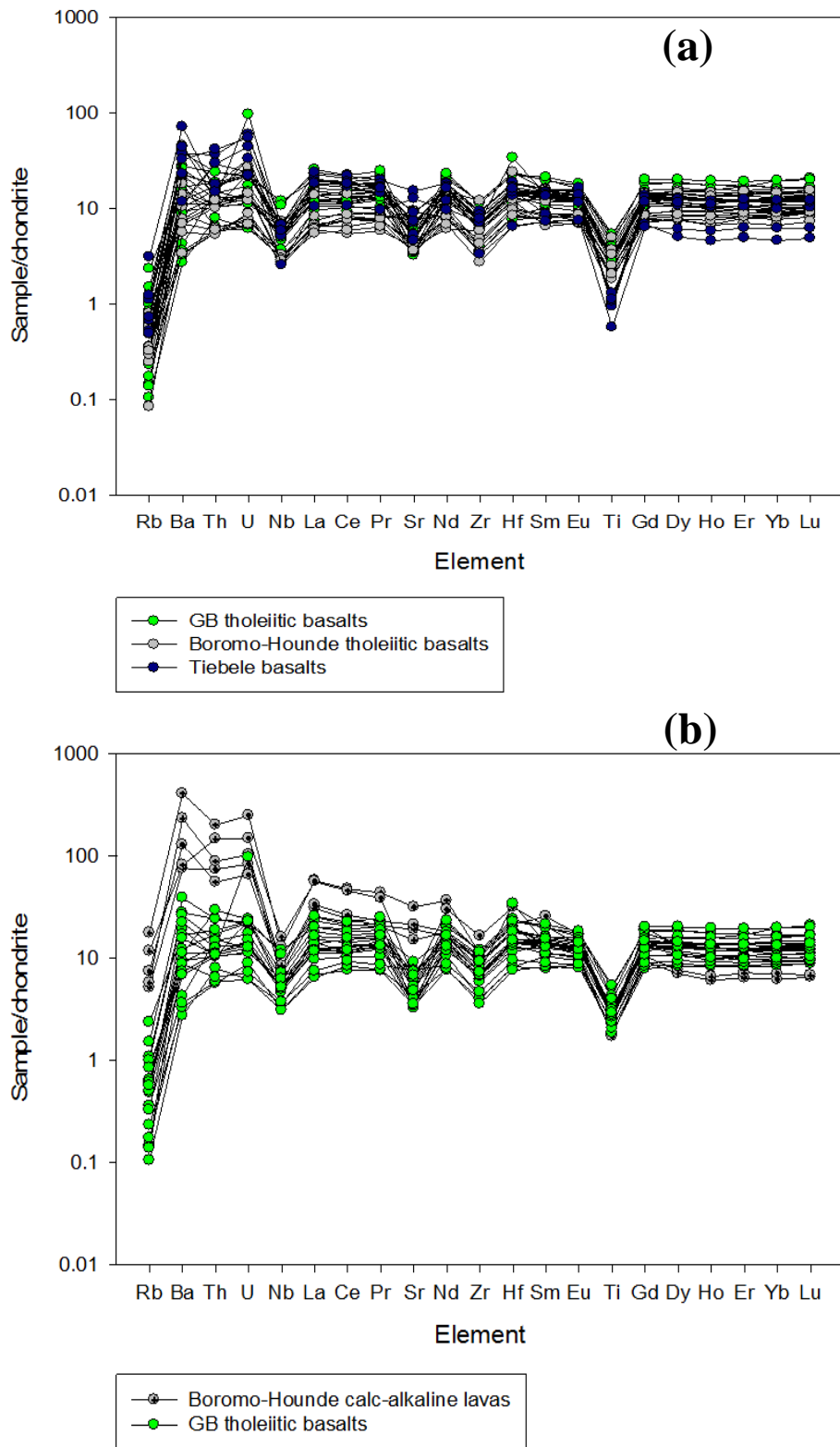
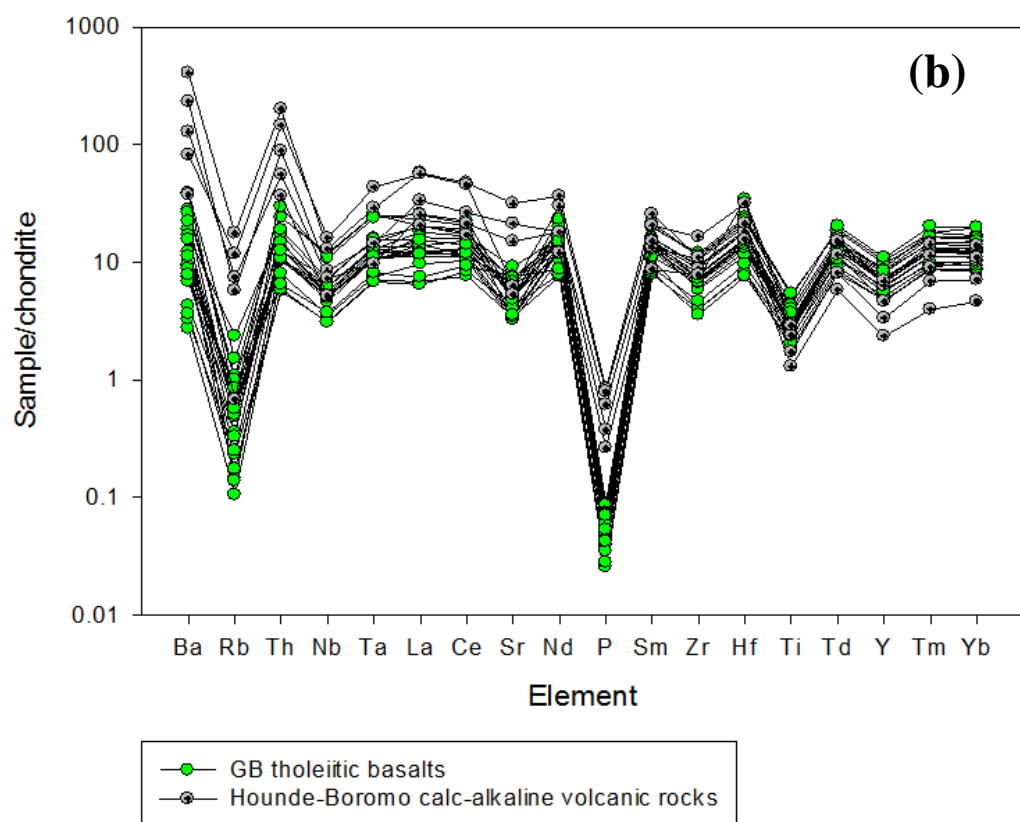
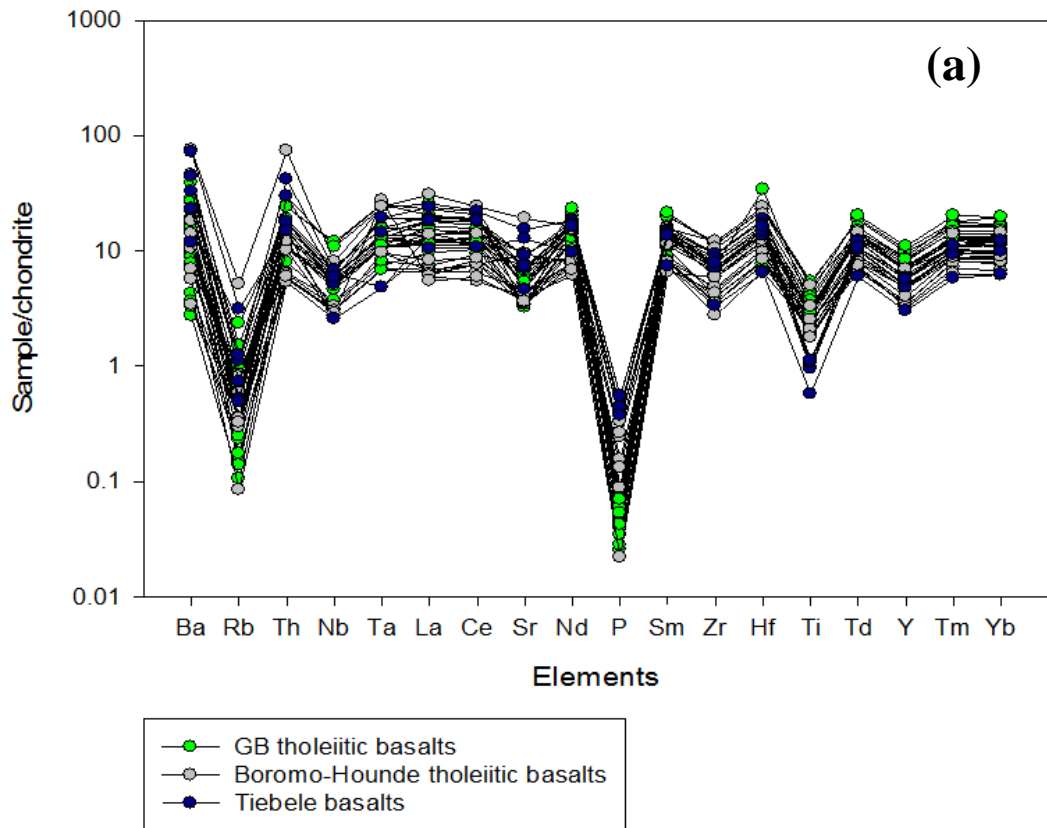


Figure 6.3 (a) Chondrite-normalised multi-element diagram comparing the tholeiitic basalts from the GB, Boromo-Houndé belts and the Tiebelé region. The sample suites contain similar trace element affinities indicated by similar patterns. Rb exhibits a negative anomaly ranging from 0.1 to 5 times the chondritic value. Similarly, Ti displays a negative anomaly ranging from 0.5 to 5 times that of chondrite. (b) Chondrite-normalised multi-element diagram comparing the tholeiitic basalts of the GB with the calc-alkaline volcanic rocks of the Boromo-Houndé belts. The Boromo-Houndé data present enrichment in Rb, Ba, Th, U, La, Ce, Pr, Sr and Nd relative to the GB samples. This indicates that calc-alkaline rocks are more enriched in LIL elements relative to tholeiitic compositions. Both sample suites have similar concentrations for the remaining elements.



(Caption overleaf)

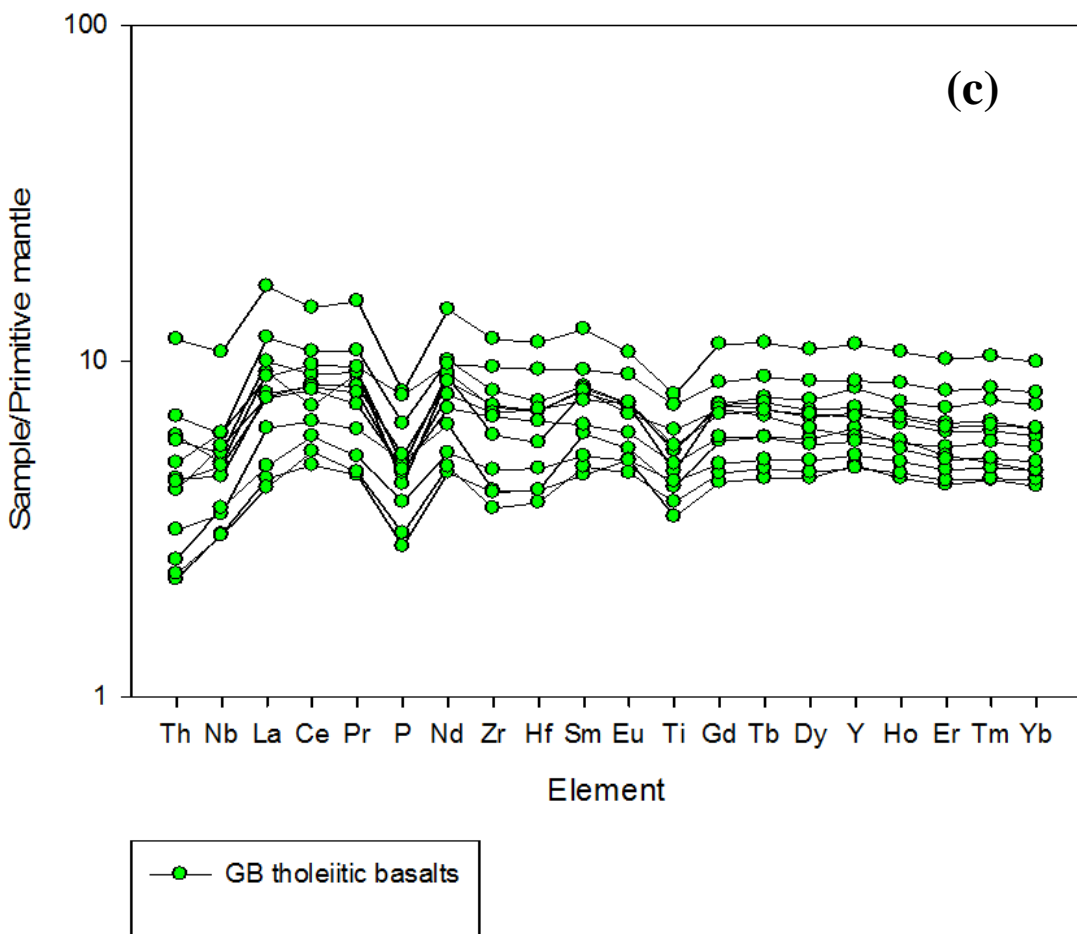


Figure 6.4. (a) Chondrite-normalised multi-element diagram comparing the tholeiitic basalts from the GB, Boromo-Houndé belts and the Tiebélé region. Similar patterns indicate similar trace element properties for the tholeiitic basalt samples from three regions. On this element array, Rb and Ti display negative anomalies. P exhibits a large, negative anomaly (~twice the size of Ti) with values ranging from ~0.03–0.5 that of chondrite. (b) Chondrite-normalised multi-element diagram comparing the tholeiitic basalts from the GB with the calc-alkaline volcanic rocks from the Boromo-Houndé belts. Enrichment from Ba to P relative to the GB samples in the calc-alkaline rocks is shown. Ba, Rb and Th show a relative enrichment of one order of magnitude, indicating significantly different trace element chemistry for the sample suites. Although the sample suites are compositionally different, the P anomaly is present throughout both plots, albeit the anomaly is smaller for the calc-alkaline volcanic rocks. (c) Primitive mantle normalised multi-element diagram with a chemical array used in McCuaig et al. (1994) that presents negative P and Ti anomalies. These anomalies are interpreted to form because of phosphorus and titanium retention in silicate minerals in the magma source region.

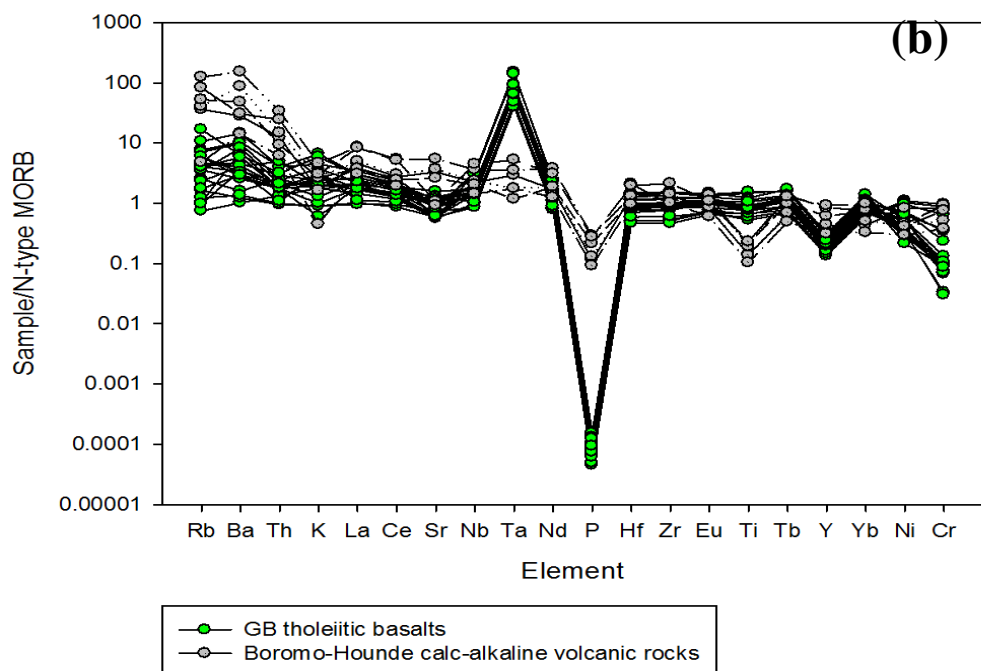
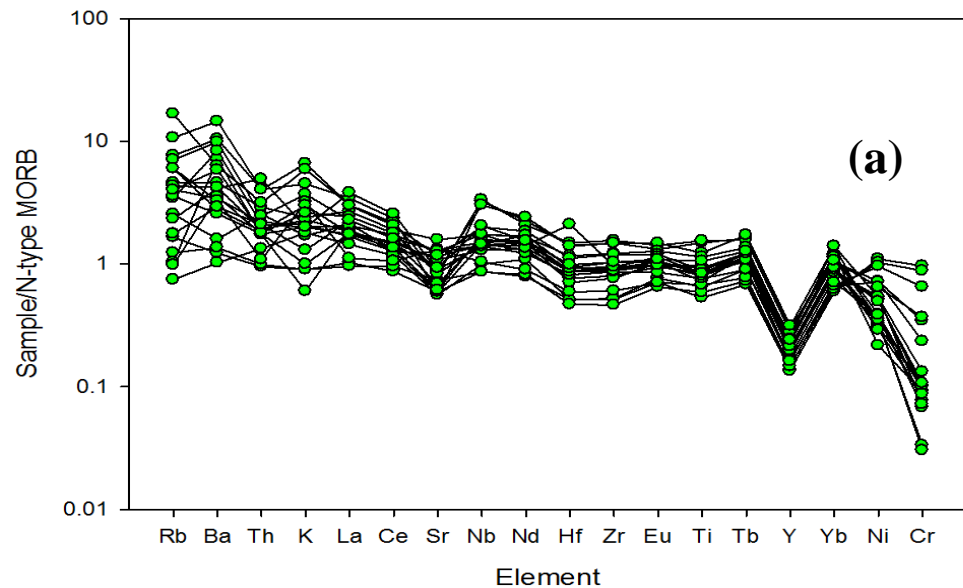
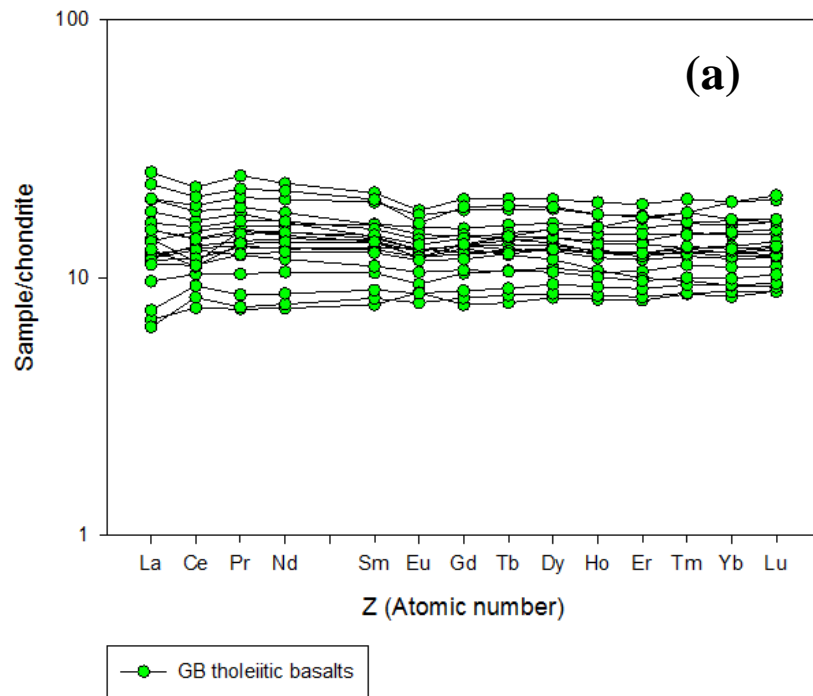


Figure 6.5. (a) N-MORB normalised multi-element (after Tarney et al., 1981) diagram presenting the data from the GB. The elemental array increases in compatibility from left to right. Ta and P are removed from the x-axis. The data represents a similarity between the GB rocks and the average N-type MORB concentrations. A range in concentrations exists but they do not deviate significantly from the N-MORB values. Rb and Cr have the widest range of concentrations (~1-20 and ~1-0.05 the value of N-MORB) and Y portrays a negative anomaly, consistent with each sample. (b) N-MORB normalised multi-element diagram (after Tarney et al., 1981) comparing the GB tholeiitic basalts to the Boromo-Houndé calc-alkaline volcanic rocks. Ta and P are added to the x-axis. The GB tholeiitic basalts present large Ta and P anomalies, positive and negative, respectively. The calc-alkaline rocks present negative Ti and P anomalies.

The chondrite-normalised REE patterns (Figure 6.6a) show an overall flat trend, although samples are slightly enriched, or slightly depleted in LREE relative to HREE. Small negative Eu anomalies as well as positive and negative Ce anomalies were observed in some samples. When comparing the Tiebélé basalts to the GB tholeiitic basalts (Figure 6.6b), the LREE are slightly enriched relative to the HREE. The majority of the Tiebélé basalts exhibit REE concentrations more than 10 times that of chondrite. Both negative and positive Eu anomalies occur in the Tiebélé basalts, which contrasts with the GB tholeiitic basalts. The positive anomalies suggest that plagioclase accumulated from the melt in high enough abundance to allow for positive Eu concentrations.

The REE patterns for the tholeiitic basalts from the Boromo-Houndé belts are similar to the GB (Figure 6.6b). They possess a flat overall trend coupled with minor enrichment or depletion. They are 5 to 14 times that of chondrites. The Boromo-Houndé samples do not show Eu anomalies.



(caption overleaf)

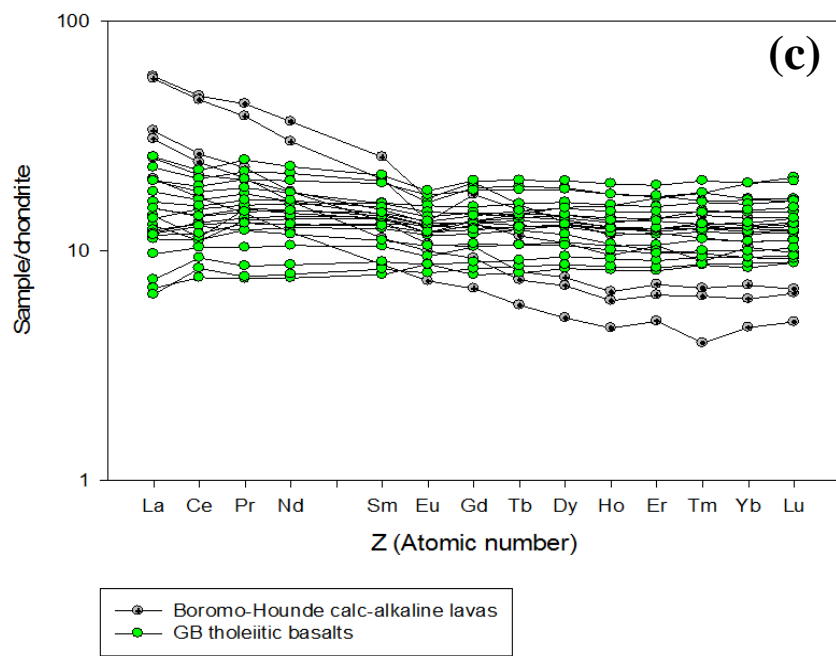
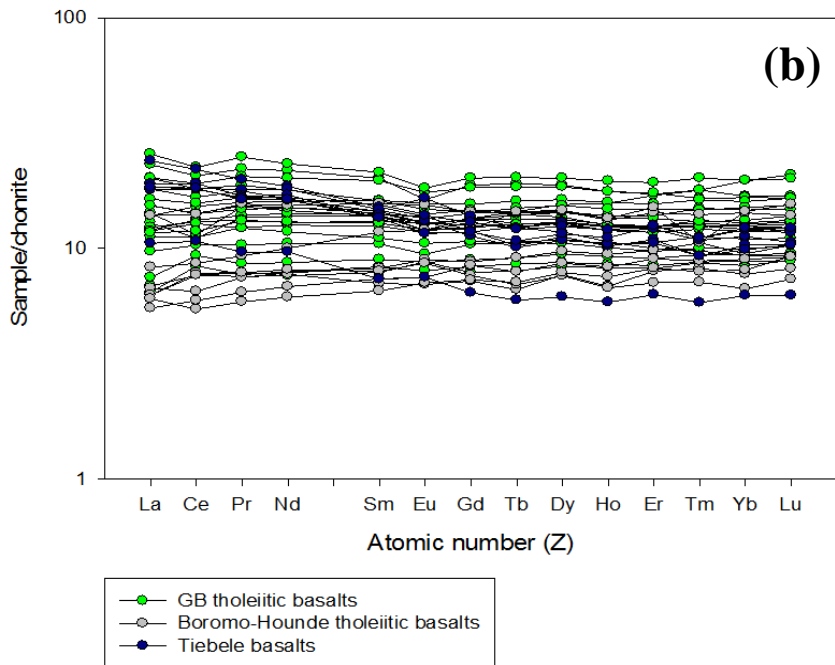


Figure 6.6. (a) Chondrite-normalised REE patterns for the GB tholeiitic basalts. The data presents flat overall patterns and are considered typical of tholeiitic MORB. The average range in concentrations for LREE is from ~8-25 times the chondritic value, whereas the HREE range between ~9 and 20 times chondrite. Some samples present slight depletions, while others present slight enrichments from LREE to HREE. (b) Chondrite-normalised REE diagram comparing the GB, Boromo-Houndé and Tiebélé tholeiitic basalts. The REE patterns of each sample suite present parallel patterns of similar magnitudes. The Tiebélé samples present a slightly decreasing trend from LREE to HREE. (c) Chondrite-normalised REE diagram comparing tholeiitic basalts from the GB to the Boromo-Houndé calc-alkaline volcanic rocks. The calc-alkaline rocks present enrichment in LREE relative to HREE compared to the tholeiitic compositions, resulting in a decreasing trend. Boromo-Houndé calc-alkaline volcanic rocks have La values range from ~30-80 time chondrite and Lu between ~6 and 12 times chondrite. Negative Eu anomalies are present.

The GB tholeiitic basalts and the Boromo-Houndé calc-alkaline lavas are plotted in Figure 6.6c and demonstrated a noticeable enrichment in LREE relative to HREE for the calc-alkaline volcanic rocks. The La values vary between 21 and 60 times chondrites, all of which were larger than the GB La values. The $(\text{La}/\text{Yb})_{\text{CHON}}$ for the GB tholeiitic basalts range from 0.65 to 3.14, whereas the ratio for the calc-alkaline volcanics range from 2.44-5.27. A large enrichment indicates a slightly more evolved melt, typical of calc-alkaline compositions (Saunders and Tarney, 1984), as would be expected. Negative Eu anomalies are observed for samples H03 and H09, which are significantly larger than that of the tholeiitic basalts. This suggests that either more plagioclase retention occurred in the residue during melting or plagioclase fractionation occurred and was then removed.

Tectonic discrimination diagrams are used in this study to provide some indication as to the type of tectonic setting that existed at the time the basalts were erupted. For older geological terranes, these diagrams are best used in conjunction with other sources of evidence such as geochemistry, lithological relationships and petrographic studies to improve confidence in interpretation (Rollinson, 1993).

The relatively immobile HFS elements (Zr, Ti, Nb, Y and P) are ideal elements to use when attempting to discriminate between different settings. They are considered to withstand the effects of hydrothermal, seawater and metamorphic alteration up to middle amphibolite facies (Rollinson, 1993; White, 2013). Consequently, the Ti-Zr-Y plot (Figure 6.7a), a binary plot which uses Zr versus Ti (ppm) (Figure 6.7b), and a Zr-Nb-Y ternary discrimination plot (Figure 6.9c) were chosen to represent possible tectonic environments into which the basalts of the GB were erupted.

The Ti-Zr-Y plot (Figure 6.7a) is able to differentiate ‘within-plate’ basalts from other tectonic environments. However, it is not the most useful diagram when it came to discriminating between MORB, island-arc tholeiitic basalts and calc-alkaline basalts because these fields overlap on the diagram. Regardless, the majority of data for the GB plot within the field of MORB, island-arc tholeiitic basalts and calc-alkaline basalts, eliminating the possibility of a ‘within-plate’ environment. The remaining samples plot outside the field boundary.

The binary diagram (Figure 6.7b), which used Zr versus Ti (ppm), was the most ambiguous discrimination diagram because it shows significant tectonic field overlap. The GB samples plot within the field described by MORB, island-arc tholeiitic basalts and calc-alkaline basalts, but the majority of samples plot in the MORB only field, with one sample close to MORB in the calc-alkaline field. However, Figure 6.7b indicates a strong possibility for the presence of MORB.

The GB sample data was also plotted on a Zr-Nb-Y ternary discrimination diagram (Figure 6.7c) (after Meschede, 1986) in order to characterize the various types of MORB and identify volcanic-arc basalts (Rollinson, 1993). The GB samples plot well within the field that represents the tectonic setting of N-type MORB or volcanic arc basalts. There was a weak correlation resolved amongst the data points trending from higher to lower Y concentrations. As Y decreased, Zr and Nb increased slightly.

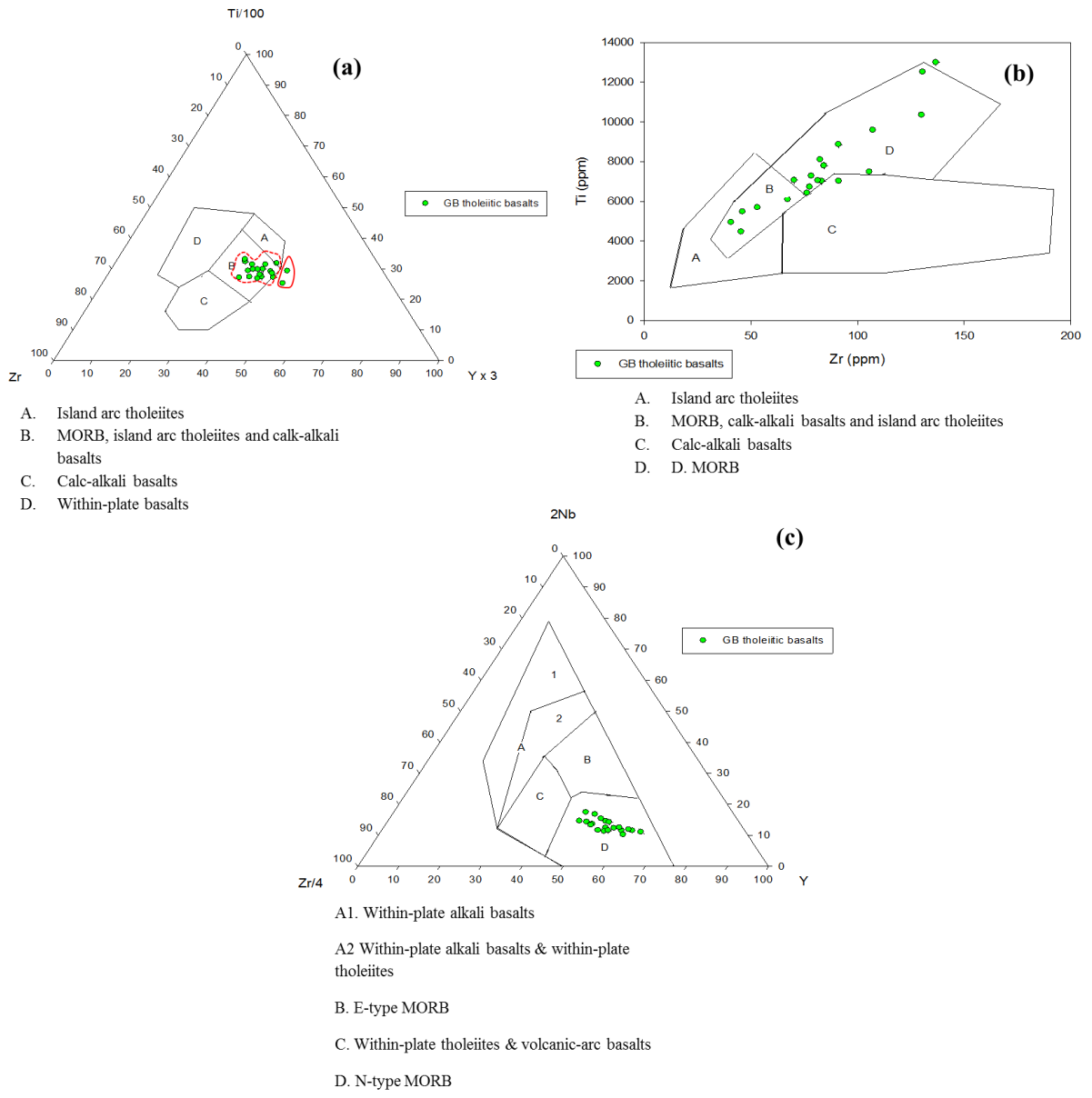


Figure 6.7. (a) Ternary discrimination diagram ($Ti/100$, Zr and $Y \times 3$). The data are clustered within field B and A, indicating most of the GB volcanic rocks are MORB, island arc tholeiite or calc-alkaline basalt. Two outliers, although clustered with the data, do not plot in a tectonic field. (b) Binary discrimination diagram that plots Zr versus Ti (ppm). A good correlation between the data is presented. The GB volcanic rocks plot in fields B and D, representing MORB, calc-alkali basalts and island arc tholeiites; therefore, no definitive tectonic setting can be established from this graph. (c) A ternary discrimination diagram ($2Nb$, Y and $Zr/4$) that follows from Figure 6.7b. The GB samples plot well within field D. Field D categorizes the data either as N-type MORB or volcanic-arc basalts. The data represents a linear trend, becoming more enriched in Zr and Nb or Y .

Averages and ranges for TiO_2 (weight %), Zr (ppm) and certain REEs (including ratios) for the GB, Boromo-Houndé and Tiebélé samples are presented in Table 6.1. Normalizing factors were taken from Anders and Grevesse (1989). The table reports differences in concentrations for these immobile trace elements, which are approximated to occur in specific tectonic regimes. The GB samples had slightly higher Nb, Th and larger $[\text{La/Yb}]_{\text{CHON}}$ values compared with the Boromo-Houndé volcanics. Despite this, their concentrations are similar. This suggests that the environment(s) into which the basalts were erupted were similar.

The Boromo-Houndé calc-alkaline rocks were included in Table 6.1. Besides the lower concentration of TiO_2 , they exhibited significantly higher values for Zr , Nb, Th and $[\text{La/Yb}]_{\text{CHON}}$. The Tiebélé volcanics share similar TiO_2 , Zr and Nb values with the GB samples; however, slightly larger concentrations of Th were observed. The notable difference is the anomalously high $[\text{La/Yb}]_{\text{CHON}}$ values, which are almost 4 times that of the Boromo-Houndé calc-alkaline rocks, with an average ratio value of 11.93.

Summarily, the Boromo-Houndé volcanic rocks are a combination of tholeiitic and calc-alkaline basalts and andesites, which agrees with Baratoux et al. (2011). The Tiebélé volcanic rocks that were classified as basalt by Ilboudo (2010), show trace-element chemistry that is typical for tholeiitic basalts. However, major element classification diagrams suggest that they are not all basaltic rocks but some are trachy-andesite and trachy-basalt, but geochemical differences are most likely the result of alteration rather than primary chemistry. With regards to the GB, three discrimination plots, REE and various multi-element patterns suggest that the basaltic rocks are N-type MORB and/or volcanic arc basalts.

6.2. Geochemistry of the Mn-Fe-rich carbonaceous sedimentary rocks

Specimens of metamorphosed Mn-Fe-rich carbonaceous sedimentary rocks were sampled from various localities within the southern GB (Figure 3.1). They were geochemically analysed to ascertain base metal concentrations and Ba concentrations. Anomalous Ba concentrations can indicate seafloor hydrothermal activity (c.f., Burnham, 1962; Lydon, 1988; Çağatay 1993; Herrington et al., 2005).

In general, the six samples are fine-grained, massive to finely laminated and banded, with rare intercalated carbonate beds (Section 5.2.3). They are composed of Mn-Fe oxide minerals, varying concentrations of sulphides and carbon. The major element geochemistry of these rocks yield SiO_2 values between 73 and 93 wt%. This is interpreted to be the result of addition of silica during multiple phases of silicification, as found for basalt samples (Section 6.1). In comparison, Mn-Fe-rich carbonaceous sedimentary rocks from the Nangodi belt in northern Ghana (Figure 1.1) show 31-56 wt% SiO_2 (Melcher, 1995), which is considerably lower than that reported for the GB samples. Al_2O_3 contents in the GB samples range from 2.3-14.95 wt%. FeO values range from 1.7 to 5.59 wt %

whereas MnO from 0.02-8.44 wt%. Loss on ignition (LOI) values are notably high with values from 6.5 to 9.5 wt%. This is interpreted to be a result of high carbon or carbonate content.

Concentrations of major and trace elements, vary between samples and are not specific to iron and manganese content. However, where base metals are enriched, Ba is also enriched, but not in all samples. XRF trace element analyses of Samples G12-004, G12-023 G12-02-035 and G12-02-080 report Ba concentrations of 115, 197, 666 and 1155 ppm, respectively. ICP-MS concentrations gave lower values, but still significantly higher than Samples G12-017 and G12-02-015, which yields concentrations of less than 35 ppm for both analyses. The mean average for Mn/Fe for all samples is 12.518. The high Mn values, relative to Fe in the samples suggests that ample amounts of fractionation of these two metals may have occurred (Melcher, 1995). The ratio of Co/Zn ranges from 0.04 to 1.19, with an average of 0.378.

In summary, silicified Mn-Fe-rich carbonaceous sedimentary rocks from the GB show correlations between Ba and base metal concentrations as well as Al₂O₃ contents for some samples. This suggests a possible influence of volcanic-related hydrothermal fluids.

7. INTERPRETATIONS AND DISCUSSION

7.1. Depositional Environment and Interpretations

The intercalated, conformable succession and spatial distributions of the lithologies of the GB indicate simultaneous deposition of sedimentary and volcanic rocks. The lithologies represent proximal to distal depositional facies relative to a volcanic source region (Figure 7.1). The depositional environment and spatial distributions were constrained using volcanic and sedimentary textures, lithological relationships, mineralogies and alteration types.

7.1.1. *Volcanic rocks of the southern Goren belt*

The basaltic rocks of the GB present textural evidence that distinguishes subaqueous from subaerial extrusion. This evidence includes hyaloclastic brecciation, high concentrations of amygdales and vesicles, an abundance of pillow lavas, and volcano-sedimentary lithological relationships. Lithological relationships include siltstone intercalations within the volcanic sequences and turbiditic greywacke sequences. These textures suggest a subaqueous environment was present during basin formation.

Pillow lavas are a significant environmental indicator for eruption settings. The formation of pillow lavas often suggests that eruptions occurred under water. They are associated with low discharge rates of magma and/or extrusion onto low gradient slopes (Griffiths and Fink, 1992). Pillow lavas of the southern GB are interpreted to have formed in relatively shallow water, due to their high vesicle abundance, and perhaps only a few hundred meters water depth (cf. Jones, 1969). The vesicles indicate movement of gas toward flow boundaries, particularly the top of flow units; for example, Archaean subaqueous basalts in Quebec were identified by Dimroth et al. (1978) with an abundance of vesicles positioned towards the upper margins of flow units and less abundant in the flow/pillow interior. However, the accumulation of vesicles is not unique to subaqueous flows. In subaerial lava flows, such as pahoehoe lavas, the vesicles differ in size, shape and accumulation (McPhie et al., 1993), with no accumulation in any particular part of the flow, but with random distribution, and vesicles are large.

Volcanic textures, lithofacies and mineralogies are critical when determining volcanic facies. Porphyritic, aphyric, glassy, variolitic and amygdaloidal textures indicate that the GB basaltic sequences represent coherent units. They make up a large proportion of the volcanic facies architecture of the study area.

The hyaloclastic basalts of the southern GB are characterized by angular basaltic fragments surrounded by an altered, fine-grained matrix. Hyaloclastite basalts in general, form most commonly

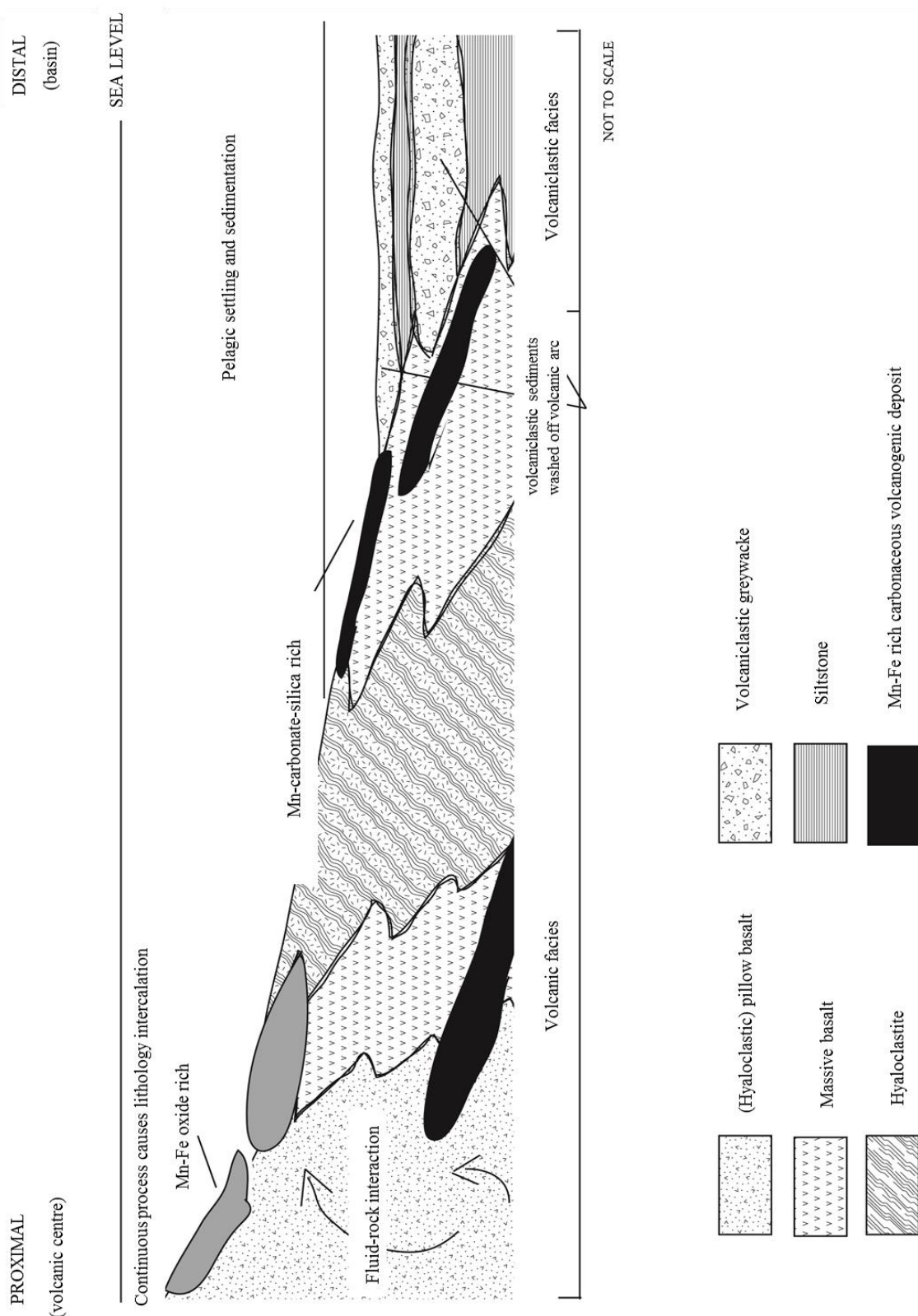


Figure 7.1. Schematic diagram depicting the lateral volcanic facies variation of the Goren volcano-sedimentary belt at the time of deposition. Volcanic lithofacies represented are pillow and massive basalts.

in low viscosity lavas and are a product of non-explosive, in-situ, quench fragmentation. Quench fragmentation is a result of the immediate contact between cold water and hot lava (Lajoie and Stix, 1992; Parfitt and Wilson, 2008). Basaltic liquid is known to erupt at temperatures in excess of 950 °C (Green and Ringwood, 1967) making the thermal difference between seawater and lava possibly in excess of 900 °C. It is interpreted that the basalts of the southern GB extruded directly onto the seafloor.

The hyaloclastite units represent an autoclastic facies, which is commonly observed as intercalated, transitional units within the coherent units in the southern GB. Summarily, autoclastic units share a close spatial relationship with the coherent units (McPhie et al., 1993).

Porphyritic and aphyric textures are characteristic of coherent units. They represent crystallisation processes within the magma chamber prior to eruption (McPhie et al., op cit.). In the GB, aphyric textures are ubiquitous (thus coherent units) and represented by uniformly fine-grained plagioclase and clinopyroxene that were altered to chlorite, actinolite and epidote. Coherent volcanic lithofacies include massive, pillowd, tortoise-shell jointed, variolitic and flow banded basalts. They occurred in conjunction with aphyric, amygdaloidal and less commonly variolitic and porphyritic basalts, which further validate the coherence of the units.

Varioles form due to liquid immiscibility caused during cooling of lavas. However, in old rocks they can be misleading. Arndt and Fowler (2004) suggested that varioles are best used as descriptive terms in the field as they are often misinterpreted as accretionary lapilli, amygdales, magma mixing textures or altered phenocrysts. Arndt and Fowler (op cit.) suggested that varioles, which form by liquid immiscibility in Archaean and Palaeoproterozoic rocks, are actually quite rare. They require further geochemical examination to determine their formation process.

In general, flow banding can occur in basalt (Expedition 309 Scientists, 2005), despite being more commonly observed in felsic lavas such as dacite and rhyolite. The distinct variation in composition suggests preferential mineral accumulation occurred, thus creating compositional bands (leucocratic and melanocratic bands). Although considered rare in mafic, non-viscous lavas, flow banding has been recorded in the Archaean Barberton greenstone belt of South Africa (Robbins et al., 2010) and occurs in the southern Bouroum belt in Burkina Faso (WAXI, 2013) (Figure 1.1).

The coherent and autoclastic units of the study area formed as a result of effusive eruptions. Effusive eruptions are typical of basaltic liquids, particularly when submerged beneath the confining water column. Effusive eruptions are characterized by the ability of lava to flow (low viscosity) rather than explode (Parfitt and Wilson, 2008) because volatiles escape passively through vesicle formation (McPhie et al., 1993; Bardintzeff and Mc Birney, 2000; Parfitt and Wilson, 2008).

The coherent and autoclastic facies are interpreted to have formed proximally to the volcanic source. However, because basaltic lavas have low viscosities, they are able to flow laterally between tens and hundreds of metres before solidification. This is dependent on the gradient of the sea floor, morphology of the lava and cooling rate (Smellie and Hole, 1997). Thus it is reasonable to suggest that

the GB basalts could have extended into an intermediate facies, further away from the volcanic vent from which they were erupted.

7.1.2. Sedimentary rocks of the south Goren belt

Conformable sedimentary sequences are intercalated with basalt flows in the stratigraphic sequence of the southern GB. These include Mn-Fe-rich carbonaceous sediments, siltstone, volcaniclastite, volcanogenic greywacke and a discrete pyroclastic breccia deposit.

Mn-Fe-rich carbonaceous sedimentary rocks are common in the southern GB (Section 4.3.5; Hein et al., 2004) and, in fact, throughout the WAC (Section 1.1; Blanchot et al., 1972; Bésoles, 1977; Wright, 1985; Neumann, 1988; Leube et al., 1990; Melcher, 1995; Kříbek et al., 2008; Beauvais et al., 2008). They are also reported from a number of Palaeoproterozoic terranes in India (Roy, 1968; 1973, 1981; Roy and Purkait, 1968), Guyana (Choubert, 1973) and South Africa (Gutzmer and Buekes, 1996; Eriksson et al., 1993; Beyeme Zogo, 2010).

The Mn-Fe-rich carbonaceous sedimentary rocks from the southern GB are commonly intercalated with basaltic units and/or siltstone-volcaniclastite units (Section 4.3.5). These rocks have elevated Ba concentrations (Chapter 6.2) and disseminated pyrite, chalcopyrite, braunite, iron-oxides, native Au and quartz-carbonate vein systems (Section 5.2.3), all of which resemble volcanogenic manganese deposits described by (Constantinou and Govett, 1972; Mosier and Page, 1988). The formation of volcanogenic manganese deposits is indicative of the formation of VHMS deposits. Hydrothermal fluids permeate through fractures, leaching metals from the underlying basalt (Lydon, 1988). The metal assemblages in VHMS and volcanogenic manganese deposits commonly include Cu-Zn-Pb-Ag-(Au) and Mn-Fe-(Au) (Mosier and Page, 1988). With respect to the GB, the volcanogenic system included Cu, Fe, Mn and minor Au, but lacked Pb-Zn. Additionally, the southern GB is dominated by secondary manganese oxides as veins, breccias, tablets and colloform overgrowths (Sections 4.3.5 and 5.2.3). These overprinting textures resemble typical supergene alteration found in the Kuruman manganese deposits in the Transvaal Supergroup of South Africa (Beyeme Zogo, 2010), suggesting that the volcanogenic system underwent supergene alteration at some stage.

The volcanogenic manganese deposits of the GB resemble the Cyprus-type volcanogenic manganese deposits defined by Mosier and Page (1988). Cyprus-type deposits occur as lenticular units bounded between volcanic and volcaniclastic rocks, and can be proximal to distal to the volcanic source. It is probably the case for the GB that the Mn-Fe-rich, carbonaceous sedimentary rocks formed as volcanogenic manganese deposits in a proximal to distal volcanic setting. A distal setting is indicated by low Ba concentrations, fine-laminations with thin ferruginous chert, and dolomite interbeds, while a proximal setting is indicated because some Mn-Fe-rich units present an increase in oxides and Ba concentrations and increased base metal values.

A correlation between increased Ba and base metals also suggests seafloor hydrothermal activity in a proximal setting to a volcanic source (c.f., Burnham, 1962; Lydon, 1988; Çağatay 1993; Herrington et al., 2005). For the most part, higher Ba values in the GB correlate with higher concentrations of Mn, implying that the manganese deposits formed in oxidising conditions proximally.

The manganese mineralization of the GB is similar to primary manganese mineralization seen throughout the WAC that is interpreted as volcanogenic in character. For example, the VHMS mineralization in the Tiebélé belt is intercalated with chert and manganese units (Sections 1.1 and 2.4) in carbonaceous manganese rocks (Ilboudo, 2010) and is characterized by sphalerite-galena-chalcopyrite-pyrite-bornite assemblages that are volcanogenic. Additionally, the manganese-carbonates of the Nsuta deposit in the Ashanti Belt in Ghana are hosted by a volcano-sedimentary sequence in basalt-andesite units (Nyame, 2008), and indicate a volcanic setting. Furthermore the Tambão (supergene) deposit in Burkina Faso (Figure 1.1) is sited above primary manganese-rich carbonate that is hosted in volcanic units (Colin et al., 2005). There is thus a strong correlation between primary manganese mineralization in the WAC and a volcanic setting, with a potential for exploitable resources of base metals and primary manganese. The Tambão deposit has an exploitable reserve of 15 Mt of manganese ore divided between primary and supergene manganese resources (Colin et al., 2005).

The greywacke units of the GB are characterized by trough cross bedding, upward-fining sequences, scour and fill, thin conglomerate interbeds, flame structures, chert interbeds, mud clasts and mud drapes (Section 4.3.3) which indicates that deposition took place in a marginal marine to offshore environment (Fischer and Schmincke, 1994; Boggs, 2006). The greywacke units best represent a prograding delta front adjacent to a shelf margin. This is supported by fining upwards sequences interpreted to represent various incomplete, small-scale Bouma sequences (Bouma, 1962). Turbidite flows can account for large volumes of sediment deposition in a short period of time, thus explaining the thick succession in the GB, relative to thicknesses of other lithologies. The presence of conglomerate beds and mud clasts, possibly due to rip-up action within the greywacke units suggests energetic and erosive deposition (Walker, 1992).

The greywacke units of the GB are composed of coarse-grained, angular to sub-rounded quartz, plagioclase and intact clinopyroxene grains (Sections 4.3.3, 5.2.1). Clinopyroxene and plagioclase grains are readily altered during transportation processes (Albarede, 2003), suggesting that deposition of the greywackes in the southern GB took place proximal to the source. Consequently, the greywacke was likely derived from a volcano-(plutonic) source nearby.

The pyroclastic breccia unit of the GB is a polyolithic, poorly bedded, poorly sorted deposit that is interbedded within the greywacke succession (Section 4.3.4). The breccia is composed of euhedral quartz, plagioclase, volcanic hornblende and anhedral clinopyroxene crystals cemented with a fine-grained epidote-sericite rich matrix (Section 5.2.2). The euhedral mineralogy, coupled with the lack of

sedimentary structures, suggests that the breccia formed as a pyroclastic deposit. The fine-grained matrix and polylithic fragments probably constitute volcanic ash, lapilli and bombs. In summary, the pyroclastic breccia is a clear indication of bimodal volcanism in the GB during formation of the belt.

Finally, volcanically-derived hornblende occurs in volcanic-arc environments (Pearce et al., 1983; Cameron, 1985). The explosive nature of the deposit, as evidenced by block and bomb-sized volcanic debris, implies the breccia was not derived from the same volcanic source as the basalt sequence. The coarser, denser volcanic material is likely to have been deposited proximal to the source, whereas a fine-grained ash deposit was perhaps dispersed further away (Lajoie, 1984; Lajoie and Stix, 1992; McPhie et al., 1993).

7.2. Tectonic setting of the Goren belt and geochemical interpretations

The basalt of the GB are N-type tholeiitic MORB. Tholeiitic basalts in general, are common in a variety of tectonic settings, for example, ocean islands, island-arcs, intra-continental rifts and mid-oceanic ridges. Therefore, trace element data and other lines of evidence are required to confidently place the formation of the GB volcanic rocks into a tectonic setting.

Hottin and Ouedraogo (1992) contented that the GB contained tholeiitic basalt, calc-alkaline andesite, dacite and rhyolite throughout the entire belt. Hammond (1997) refuted the existence of felsic lavas in the southern GB. However, Castaing et al. (2003) reported rhyolitic tuff with ages of 2238 ± 5 Ma and 2177 ± 5 Ma from the northeast and southeast of the GB, respectively, and they represent the oldest ages for the Birimian Supergroup in the WAC. Roberts (1996) reported rhyolitic flows in the southern GB. However, geochemical and field evidence from the southern GB does not confirm this. Samples from the study area reported higher than expected SiO₂ concentrations, showing dacitic compositions at most on a standard Streckeisen diagram, but silica in the samples studied is the result of silica alteration and not primary composition as evidenced petrographically (Chapter 5; Section 6.1). Thus, primary calc-alkaline andesite, dacite and rhyolite units do not exist in the southern GB.

Additionally, in comparing tholeiitic basalts from the GB with tholeiitic basalts from the Tiebélé and Boromo-Houndé belts, and calc-alkaline rocks from the Boromo-Houndé belts, differences in geochemical affinities become apparent. Major element geochemistry, despite their likelihood of alteration, suggests that the volcanic rocks of the GB are tholeiitic basalts. This was determined by classification and variation diagrams (Figures 6.3-6.8) and represented by their SiO₂, MgO, Al₂O₃ and low alkaline element contents. The variation diagrams reveal the fractionation process for different minerals, which most-likely crystallised post eruption. MgO versus NiO, CaO, Al₂O₃ and Cr₂O₃ show decreasing trends, suggesting that calcic-plagioclase and clinopyroxene were the dominant crystals produced. NiO can represent the crystallisation of olivine, however no olivine or common olivine alteration products (e.g., serpentine minerals) were observed, suggesting Ni

partitioned into clinopyroxene. Plagioclase is occasionally identified as phenocrysts and more so as microlites (Sections 4.2 and 5.1), explaining the decreasing trends in the GB samples from this study. FeO and SiO₂ content increased as MgO decreased, typical of tholeiitic evolution (Rollinson, 1993).

Trace element results show notable anomalies. The large, negative phosphorus observed in the chondrite-normalised and primitive mantle-normalised multi-element diagrams (Figures 6.5 b-c) of the GB samples was indeed surprising. However, it is a common occurrence in Archaean and Palaeoproterozoic basalts (Prof. A. H. Wilson, pers. comm.). These anomalies have been observed in a variety of mafic-intermediate volcanic rocks throughout the WAC (WAXI, 2013) although their meaning has not been studied to date.

It is unlikely that the decrease in phosphorus in the GB samples was the result of hydrothermal alteration and metamorphic processes due to the known immobility of phosphorus during low temperature processes (Rollinson, 1993; McCuaig et al., 1994). Due to a correlation of MgO versus P₂O₅ in the variation diagram plotted for the GB samples (Figure 6.2 h), where P₂O₅ increases as MgO decreases, the interpretation is that hydrothermal alteration had little or no effect. Therefore, it is suggested that Ca-perovskite and garnet were retained in the magma source as suggested by McCuaig et al. (1994) for Archaean basalts from the Yilgarn and Superior Cratons. They calculated partition coefficients for phosphorus and reported that phosphorus is more likely to substitute for silica in garnet, clinopyroxene and Ca-perovskite, and determined that phosphorus partitioned into Ca-perovskite > majorite garnet > pyrope garnet > clinopyroxene with negligible amounts partitioning into olivine, orthopyroxene and spinel.

In attempt to quantify the likelihood of phosphorus retention in the magma source in general for GB samples, a simple calculation was done (Appendix C) to determine how much phosphorus could be retained in garnet and clinopyroxene in ancient magmas. The assumption was made that 0.05 wt% P₂O₅ was present in these magmas and 15 % partial melting occurred. The primitive mantle value for phosphorus was taken from Anders and Grevesse (1989). Partition coefficient values of phosphorus for clinopyroxene and garnet are approximately 0.025 and 0.04 respectively (Rollinson, 1993). It was calculated that garnet and clinopyroxene could retain approximately 272 ppm of phosphorus. This quantity is supported by Brunet and Chazot (2001) on phosphorus retention in mantle nodules from the upper mantle. Their calculations indicated that garnet, clinopyroxene and olivine can retain up to 600 ppm of phosphorus. These calculated phosphorus values confirm that phosphorus retention in the magma source is plausible. However, further studies on phosphorus anomalies needs to be undertaken from individual terranes across the WAC in order to create a petrogenetic model with reference to modern and ancient tholeiites. Another possibility for such anomalous phosphorus could be due to carbonate alteration. Phosphate bearing minerals such as apatite do dissolve readily in acidic fluids, even with relatively weak acidity (Prof. G. Cawthorn, Pers. Comm.).

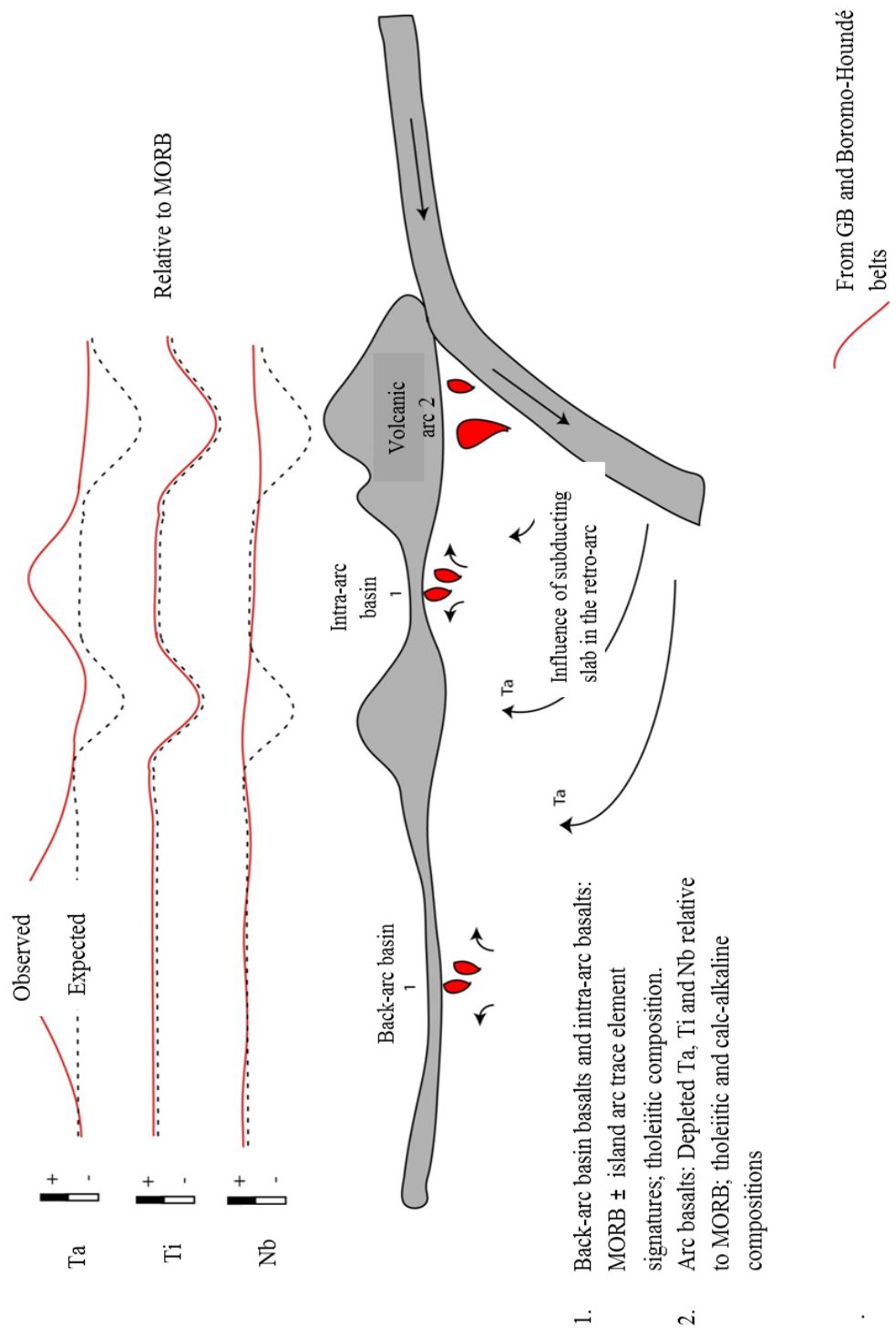
The comparison between the tholeiitic basalts from the southern GB with those from the Tiebélé and Boromo-Houndé belts, and calc-alkaline mafic-intermediate rocks of the Boromo-Houndé belts

indicate a clear difference in trace element behaviour. The calc-alkaline volcanic rocks of the Boromo-Houndé belts are interpreted by Baratoux et al. (2011) to represent an island-arc tectonic setting. The calc-alkaline rocks showed enrichments in LREE relative to HREE (Figure 6.6) and enrichments in Rb, Ba, Th and other LILE relative to those seen in the tholeiitic basalts (Figure 6.3b). The enrichments can be explained because LREE are considerably more incompatible relative to HREE. However, although Rb and Nb are of similar incompatibility during mantle melting they do not share this affinity during alteration, Rb is more mobile. LFSE to HFSE ratio in arc-related magmas are increased because fluid from the subducted slab causes mantle wedge metasomatism. This was shown by Pearce (1983) and Pearce and Peate (1995). LREE are more incompatible than HREE, however, it does not indicate that LILE are more incompatible than all HFSE as it depends on the LILE and HFSE. This idea suggests that although the samples from the Boromo-Houndé belts are most likely calc-alkaline arc-derived lavas, enriched LILE to HFSE may not be conclusive evidence on its own to support the conclusions drawn by Baratoux et al. (2011); fractionation of various trace elements relative to each should be studied further.

Volcanic arcs, inclusive of tholeiitic and calc-alkaline compositions, result from melting caused by a cold and dense subducting slab which undergoes dehydration-induced melting. During subduction and dehydration, water and HFSE move into the mantle wedge providing arc-magmas with their geochemical signature. However, rutile stabilises in the slab and allows for certain immobile elements to be retained in the subducting slab, or the sub-arc mantle wedge (Ryerson and Watson, 1987; Foley and Wheller, 1990; Saunders et al., 1991; Bau and Knittel, 1993; Sajona et al., 1993; Kepezhinskas et al., 1997). Thus, volcanic rocks from volcanic arc terranes are characterized by depletions in Ta, Nb and Ti relative to tholeiitic MORB. The GB samples contain large positive Ta anomalies and no Ti or Nb anomalies are apparent when normalised to average N-MORB compositions. In contrast, the Boromo-Houndé calc-alkaline samples have negative Ti anomalies and smooth patterns for Nb and Ta (Figure 6.5b). The differences in Ti and Ta suggest that the magma underwent processes unlikely to be derived from the same source. By comparing the data from the GB tholeiitic basalts with data from the calc-alkaline volcanic rocks of the Boromo-Houndé belts, it is also possible that the GB basalts were emplaced in a back-arc/intra-arc relative to the arc (Figure 7.2). Alternatively, hydrated MORB can stabilise Ti in Ti-bearing minerals as is seen at the modern Galapagos and EPR which gives arc-type geochemical signatures. This has significance in bimodal volcanic environments (Haase et al., 2005)

The flat REE patterns and various multi-element diagrams observed for the GB display trends similar to tholeiitic basalts that are typical of mid-ocean ridge type settings (Rollinson, 1993; Väisänen and Westerlund, 2007; White, 2013). The basalts of the southern GB possess many characteristics of tholeiitic mid-ocean ridge basalts (MORB), specifically normal MORB (N-MORB) as defined from trace elements compositions (Figures 6.7); rare earth, multi element and trace element analyses of the GB samples (Section 6.1.2). They also share some characteristics that are derived from convergent

zones and are thus interpreted to form in extentional terranes such as back arc or intra-arc basins as possible tectonic settings. The data are characteristic of back-arc and/or intra-arc basin basalts (Taylor



and Karner, 1983; Saunders and Tarney, 1984; Wilson, 1989).

Figure 7.2. Schematic diagram depicting Ta, Ti and Nb signatures relative to MORB values in a volcanic-arc environment. These values present the similarities between back-arc and intra-arc terranes as well as the differences between retro-arc and volcanic arc trace element geochemistry. The dotted line indicates the concentrations that are expected across the tectonic setting based on literature and the red line represents observed concentrations using data from the Goren belt and the Boromo-Houndé belts (interpreted back-arc/intra-arc and arc environments respectively).

Petrographically, lithologically and geochemically, back-arc and/or intra-arc basin basalts settings are extremely difficult to distinguish, especially in ancient terranes (Pearce, 1996; Väisänen and Westerlund, 2007). It was suggested by Pearce (1996) that back-arc and/or intra-arc basin basalts should be referred to as transitional between back-arc basin basalts and intra-arc tholeiites (IAT) when geochemical evidence cannot ascertain the correct tectonic setting. This has been the rationale adopted in this thesis.

7.3. The Goren belt in a regional context

In northeast Burkina Faso, geochemical analyses of volcanic rocks from various belts, including the Oudalan-Gorouol, Bouroum-Yalogo and Goren volcano-sedimentary belts suggest that deposition of supracrustal rocks occurred in island arc terranes, followed by the accretion of multiple arcs (WAXI, 2013). Vidal et al. (2009) suggested these terranes were deposited concomitantly with the emplacement of the TTG plutons (2250-2170 Ma) across the WAC, and represent the lowermost part of the Birimian Supergroup stratigraphic succession. In the GB, supracrustal deposition of Birimian Supergroup occurred prior to TTG emplacement (Hein et al., 2004; Hein 2010; WAXI, 2013).

Research conducted by Dia (1988), Lüdtke et al. (1998), Béziat et al. (2000) and Dampare et al. (2008) concluded that tholeiitic and calc-alkaline volcanic rocks are characteristic of juvenile volcanic arc systems. However, studies by Abouchami et al. (1990), including work from the Bouroum belt in Burkina Faso, suggested that the best tectonic analogue for the formation of tholeiitic basalts of the Birimian Supergroup is oceanic flood basalts (OFB). This conclusion was established from Ti and LREE depletions, where the LREE depletion is less than N-type MORBs. It was suggested that an intermediate geochemistry between back-arc basins and island-arc tholeiites made such an environment an attractive setting, especially due to regionally low Nb concentrations (Zonou, 1987), but the lack of ultramafic rocks (Burke, 1988) and unfitting isotopic and trace element signatures indicated an oceanic plateau origin (Abouchami et al., 1990).

The distinction between the GB basalt samples forming in an arc-related basin compared to an oceanic plateau setting is in their strato-tectonic context. The tholeiitic basalts from the GB have many similarities to the general tholeiitic compositions from around the craton. These similarities include the reporting of negative normalised Ti and Nb anomalies (Figure 6.5), but the GB basalts are not depleted in LREE relative to HREE (Figure 6.6), making them more enriched in LREE compared to Palaeoproterozoic OFB. Thus the GB basalts are not OFB.

With respect to the sedimentary rocks that are intercalated with the tholeiitic basalts, Abouchami et al. (1990) stated that sedimentary rocks do not host obvious reworked components. The GB has direct evidence to oppose this idea as it is composed of a conformable sequence of arc-derived volcaniclastic greywacke deposits, siltstones and pyroclastite breccia, which are more likely to have

deposited in a back-arc or intra-arc basin, proximal-distal to a pre-existing island-arc terrane (Figure 7.3). Thus the GB basalts are unlikely to be OFB.

The Birimian Supergroup has been compared to Archaean granite-greenstone terranes due to their similar lithologies and temporal relationship between supracrustal and granitoids emplacement (Bassot, 1986; N'Gom, 1989). The tholeiitic basalts are typically overlain by calc-alkaline lavas and associated sedimentary rocks and pyroclastites (Hottin and Ouedraogo, 1975; Zonou, 1987) in some belts (WAXI, 2013). The calc-alkaline volcanic rocks, are commonly intruded by TTG suite plutons throughout the WAC and post-date the eruption of tholeiitic lavas (Melcher and Stumpfl, 1992; WAXI, 2013). Various conclusions of the Birimian Supergroup stratigraphy have been reached by Junner (1935, 1940), Leube et al. (1990), Ledru et al. (1991), Milési et al. (1989, 1991), Hein et al. (2004), Hein (2010) and Baratoux et al. (2011), but the GB is interpreted to be an intercalated succession of volcanic and sedimentary rocks (Hein, 2010), which is confirmed in this study. Although the GB is represented by large quantities of MORB tholeiites, the differently-sourced pyroclastic agglomerate interbeds suggest a distinct period of localised bimodal volcanism. Essentially, whilst the GB arc-basin was infilling with lavas and sediments, arc eruptions and erosion off the arc were depositing into the basin simultaneously, supporting the model of Leube et al. (1990) and Sylvester and Attoh (1992). This indicates that the tectonic setting for the GB was probably a back-arc.

Regionally, Leube et al. (1990) identified that the Mn-Fe-rich carbonaceous sedimentary rocks, chert, carbon, carbonate and sulphide rich-rocks precipitated syn-volcanically, often proximal to volcanic edifices. This is identified in the GB as intercalated Mn-Fe-rich carbonaceous sedimentary-tholeiitic basaltic units and evidence of syn-volcanic hydrothermal activity identified as quartz-carbonate veins, Fe-Mn oxide veins, and Ba anomalies.

7.4. The Goren belt and the West African craton in a global context

On a global scale the Palaeoproterozoic is an era in which the formation of accretionary island arc systems, development of large sedimentary basins and crustal growth were dominant (de Vries et al., 2008). However, research in the WAC over the last two decades has shifted paradigms of stratigraphic-tectonic-magmatic-metallogenic-structural understanding. The Birimian Supergroup is defined by volcano-sedimentary belts rather than greenstone belts (WAXI, 2013; Tshibubudze et al., 2013), which (*sensu stricto*) commonly contain mafic volcanic components making up the majority of the belt, with subordinate sedimentary units. The volcano-sedimentary belts likely formed in arc-related basin (back-arc or intra-arc basin) that underwent periods of extension, inducing tholeiitic lavas similar to MORB.

The formation of island-arcs provide similar volcanic and sedimentary products from various locations. Volcanism, particularly arc-related, is reported from many Palaeoproterozoic terranes

including Finland, Australia, Mid-West United States and Canada (Stern et al., 1995; Hill and Bickford, 2001; Väisänen and Westerlund, 2007; Li et al., 2013). The volcanic facies are similar due to analogous depositional environments, many of which are mineralised in volcanogenic massive sulphides.

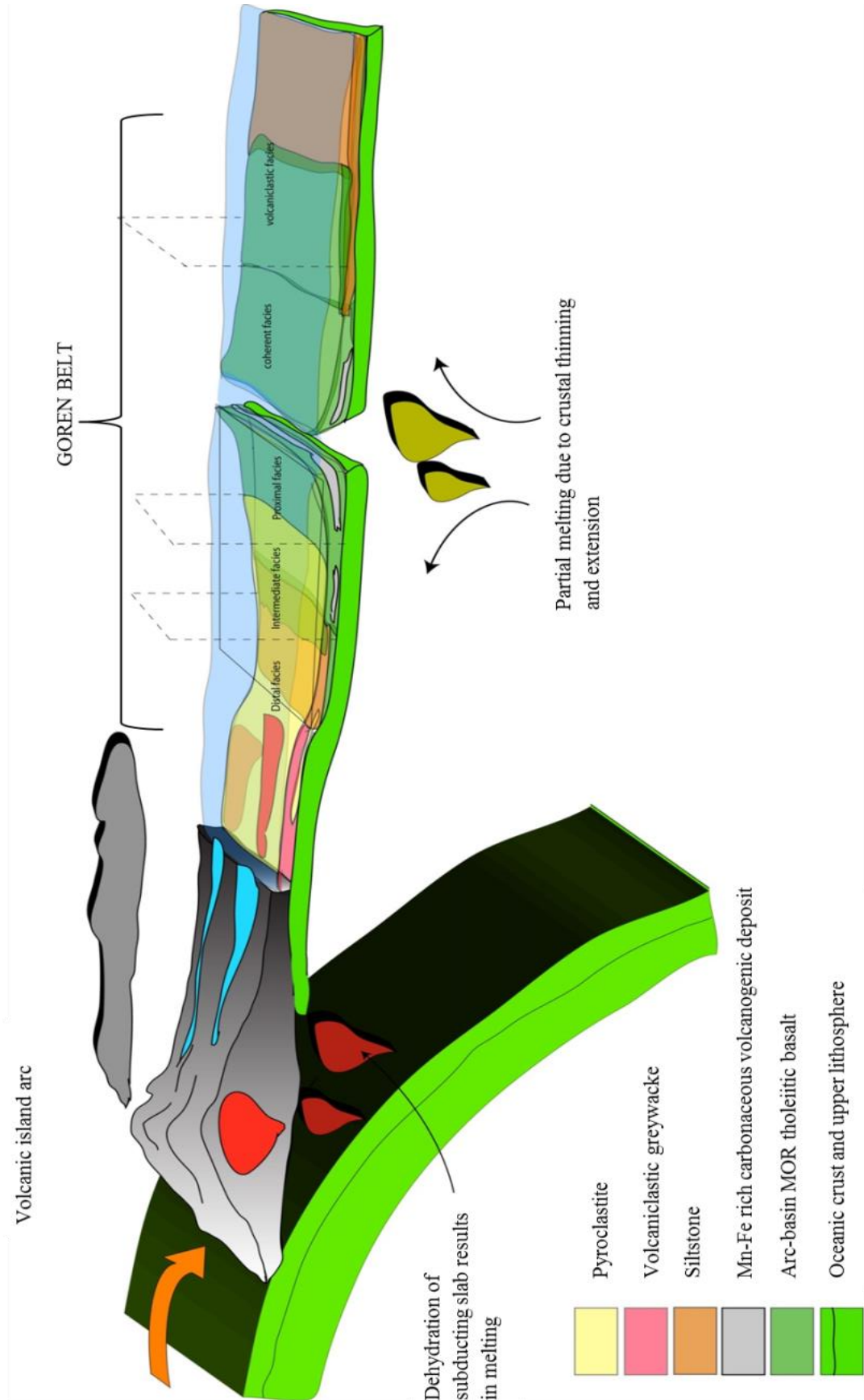


Figure 7.3. Schematic diagram illustrating the tectonic setting, depositional environment and facies distribution for the Goren belt.

8. CONCLUSIONS

8.1. Summary and conclusions

Lithological and volcanic facies maps were created using data collected during multiple field seasons. The rocks of the GB were affected by regional sub-greenschist to greenschist metamorphism. The stratigraphy is represented by a conformable succession of sub-vertically dipping, northwest-trending volcanic flows intercalated with sequences of sedimentary rocks. These include siltstone, Mn-Fe-rich carbonaceous sedimentary rocks, epiclastic greywacke units, basalt-derived volcaniclastic units and a discrete pyroclastic interbed. Conformable sequences were identified by gradational contacts in the field.

Field, petrographic and geochemical analyses were used to classify the volcanic rocks as basalts. Further geochemistry and mineralogical analyses established a tholeiitic composition. This was based on the sub-alkaline Na_2O - K_2O values, SiO_2 , MgO , Al_2O_3 concentrations and low modal abundances of the primary minerals, namely plagioclase and clinopyroxene, which typically occur as microlites. Trace element analyses, including REE and multi-element patterns show a strong similarity to tholeiitic N-MORB. This indicated that the tectonic setting was an extensional basin. Lithological and spatial relationships, comparative work with known arc-related calc-alkaline andesites from the Boromo-Houndé belts, as well as trace element tectonic discrimination indicate deposition in an arc-related basin (back-arc or intra-arc basin) that underwent periods of extension, inducing tholeiitic basalts with MORB geochemical affinities.

Analyses of volcanic textures resulted in the delineation of volcanic facies architecture. The volcanic rocks are dominated by coherent units. This was based on the occurrence of porphyritic, aphyric, aphanitic, amygdaloidal and variolitic textures, as well as flow banded, tortoise-shell jointed, massive and pillow basalts lithofacies. Intercalated with the coherent basalts were autoclastic facies characterized by (jig-saw fit) hyaloclastite breccia flows. Pillow lavas, hyaloclastites, the size and abundance of amygdales and intercalated siltstones indicated subaqueous emplacement in a marginal marine setting. Spatially, both the coherent and autoclastic facies represent a proximal facies.

Mn-Fe-rich carbonaceous sedimentary rocks formed syn-volcanically proximal to the source, indicating a proximal facies distribution. They are finely laminated, chert-bearing and contain volcaniclastite and carbonate interbeds. They are differentiated from proximal volcanogenic deposits due to lower Ba and higher carbon concentrations with little evidence to suggest unusual amounts of base metals (Cu, Pb, Zn).

Continuous successions of volcanogenic greywacke deposits occupy a distal facies relative to the volcanic source. They conformably overlie older volcano-sedimentary lithologies and represent a marginal marine to offshore deltaic-turbiditic depositional environment. This interpretation was based

on fining upwards sequences, trough cross-bedding, ripple marks, scour and fill structures, mud clasts\balls, mud drapes and conglomerate beds. Their source region is concluded to be land-derived as opposed to basin derived. Intercalated within the greywacke succession is a pyroclastic deposit containing euhedral lapilli of quartz, plagioclase and hornblende cemented in a fine to medium grained ash-lapilli sized matrix. Its derivation is interpreted as a volcanic arc source, depositing in a back-arc or intra-arc basin, thus indicating bimodal volcanism in the GB.

Potential for economic Mn and Fe mineralisation exists. An example of one such deposit is Tambão hill near the Malian border, northeast of the GB. It is also plausible for the GB to contain base metal deposits, such as VHMS deposits. However, the sample suite collected in the GB do not suggest high enough concentrations of base metals (Pb-Zn-Cu and Au) to define VHMS deposits. However, based on the similarities of deposit styles, they could potentially exist in the GB and other belts on the WAC such as the already discovered Perkoa deposit and Tiebélé dome.

REFERENCES

- Abouchami, W., Boher, M., Michard, A., Albarede, F., (1990). A major 2.1 Ga event of mafic magmatism in West Africa: an early stage of crustal accretion. *Journal of Geophysical Research*, **95**, 17605-17629.
- Albarede, F., (2003). *Geochemistry: An Introduction*. Cambridge University Press, Cambridge, 248pp.
- Allen, R. L., Lundstrom, I., Ripa, M., Christofferson, H., (1996). Facies analysis of a 1.9 Ga continental margin, back-arc, felsic caldera province with diverse Zn-Pb-Ag-(Cu-Au) sulfide deposits and Fe-oxide deposits, Bergslagen region, Sweden. *Economic Geology*, **91**, 979-1008.
- Anders, E., Grevesse, N., (1989). Abundances of the elements: meteoritic and solar. *Geochimica et Cosmochimica Acta*, **53**, 197-214.
- Arndt, N., Fowler, A. D., (2004). Komatiites and variolitic basalts. Unpublished. 28pp.
- Arndt, N.T., Albarede, E., Nisbet, E.G., (1997). Mafic and ultramafic magmatism. In: De Wit, M.J., Ashwal, L.D. (Eds.), *Greenstone Belts*. Clarendon Press, Oxford, 233–254.
- Baratoux, L., Metelka, V., Naba, S., Jessell, M.W., Gregoire, M., Ganne, J., (2011). Juvenile Palaeoproterozoic crust evolution during the Eburnean orogeny (~2.2-2.0 Ga), western Burkina Faso. *Precambrian Research*, **191**, 18-45.
- Bardintzeff, J., McBirney, A., (2000). *Volcanology*; 2nd Edition. Jones and Bartlett Publishers, Massachusetts, 268 p.
- Bassot, J.P., (1986). Le Protérozoïque inférieur de l'Afrique de l'Ouest: ce qui a été fait, ce qui reste à faire. *Publication Occasionnelle*, **10**, 7-16.
- Bau, M., Knittel, U., (1993). Significance of slab derived partial melts and aqueous fluids for the genesis of tholeiitic and calc-alkaline island-arc basalts: Evidence from Mt. Arayat, Philippines. *Chemical Geology*, **105**, 233–251.
- Beauvais, A., Ruffet, G., Hénocque, O., Colin, F., (2008). Chemical and physical erosion rhythms of the West African Cenozoic morphogenesis: The ^{39}Ar - ^{40}Ar dating of supergene K-Mn oxides. *Journal of Geophysical Research*, **113**, 1-15.
- Bessoles, B., (1977). *Géologie de l'Afrique. Le craton Ouest-Africain Mémoires*. BRGM, Paris, 88pp.
- Beyeme Zogo, J.C., (2010). Origin and emplacement of manganese with conglomeratic iron ore at the Beeshoek Iron Ore mine, Northern Cape Province. The annual report for the Palaeoproterozoic Mineralization Research Group, University of Johannesburg, 46 pp.
- Béziat, D., Bourges, F., Debat, P., Lombo, M., Martin, F., Tollon, F., (2000). A Paleoproterozoic ultramafic-mafic assemblage and associated volcanic rocks of the Boromo greenstone belt: fractionates originating from island-arc volcanic activity in the West African craton. *Precambrian Research*, **101**, 25-47.

- Béziat, D., Dubois, M., Debat, P., Nikiema, S., Salvi, S., Tollon, F., (2008). Gold metallogeny in the Birimian craton of Burkina Faso (West Africa). *Journal of African Earth Sciences*, **50**, 215–233.
- Bierschenk, W.H., (1968). Geohydrological Reconnaissance in Upper Volta. *Groundwater*, **6**, 29-40.
- Blanchot, A., Dumas, J.P., Papon, A., (1972). Geological Map of South-Central West Africa, Explanatory Note. Bureau de Recherches Géologiques et Minières, France (scale 1:2,000,000).
- Boggs, S., (2006). Principles of Sedimentology and stratigraphy: Fourth Edition, Pearson Prentice Hall, New Jersey, 662pp.
- Boher, M., Abouchami, W., Michard, A., Albarede, F., Arndt, N.T., (1992). Crustal growth in West Africa at 2.1 Ga. *Journal of Geophysical Research*, **97**, 345-369.
- Bossière, G., Bonkoungou, I., Peucat, J.J., Pupin, J.P., (1996). Origin and age of Palaeoproterozoic conglomerates and sandstones of the Tarkwaian Group in Burkina Faso, West Africa. *Precambrian Research*, **80**, 153-172.
- Bouma, A.H., (1962). Sedimentology of some flysch deposits: A graphic approach to facies interpretation, Elsevier, Amsterdam, 168pp.
- Brown, E.T., Bourles, D.L., Colin, F., Safno, Z., Raisbeck, G.M., Yiou, F., (1994). The development of iron crust lateritic systems in Burkina Faso, West Africa examined with in-situ-produced cosmogenic nuclides. *Earth and Planetary Science Letters*, **124**, 19–33.
- Brunet, F., Chazot, G., (2001). Partitioning of phosphorus between olivine, clinopyroxene and
- Burke, K., (1988). Tectonic evolution of the Caribbean. *Annual Reviews of Earth and Planetary Sciences*, **16**, 201-230.
- Burnham, W.C., (1962). Facies and types of hydrothermal alteration. *Economic Geology*, **57**, 768-784.
- Çağatay, M.N., (1993). Hydrothermal alteration associated with volcanogenic massive sulfide deposits: examples from Turkey. *Economic Geology*, **88**, 606-621.
- Cameron, W.E., (1985). Petrology and origin of primitive lavas from the Troodos Ophiolite, Cyprus. *Contributions to Mineralogy and Petrology*, **89**, 239-255.
- Cas, R.A.F., Wright, J.V., (1987). Volcanic successions, modern and ancient: geological approach to processes, products and successions, Chapman and Hall, London, 528pp.
- Castaing, C., Billa, M., Milési, J.P., Thiéblemont, D., Le Mentour, J., Egal, E., Donzeau, M. (BRGM) (coordonnateurs) et Guerrot, C., Cocherie, A., Chevremont, P., Tegyey, M., Itard, Y. (BRGM), Zida, B., Ouedraogo, I., Kote, S., Kabore, B.E., Ouedraogo, C. (BUMIGEB), Ki, J.C., Zunino (ANTEA), (2003). Notice explicative de la Carte Géologique et Minière du Burkina Faso à 1/1 000 000.
- Cheilletz, A., Barbey, P., Lama, C., Pons, J., Zimmerman, J.L., Dautel, D., (1994). Age de refroidissement de la croûte juvénile Birimienne d'Afrique de l'Ouest. Données U-Pb, Rb-Sr et K-Ar sur les formations à 2.1 Ga du SW Niger. *Comptes Rendus Académie Sciences Paris*, **319**, 435–442.

- Choubert, B., (1973). Occurrences of manganese in the Guianas (South America) and their relation with fundamental structures. UNESCO, Earth Science Series, **9**, 115-124.
- Colin, F., Beauvais, A., Ruffet, G., Hénocque, O., (2005). First 40Ar/39Ar geochronology of lateritic manganeseiferous pisolithes: Implications for the Palaeogene history of a West African landscape. *Earth and Planetary Science Letters*, **238**, 172– 188
- Constantinou, G., Govett, G. J. S., (1972). Genesis of sulphide deposits, ochre and umber of Cyprus. *London Institute of Mining and Metallurgy Transactions*, **81**, 34-46.
- Dampare, S.B., Shibata, T., Asiedu, D.K., Osae, S., Banoeng-Yakubo, B., (2008). Geochemistry of Paleoproterozoic metavolcanic rocks from the southern Ashanti volcanic belt Ghana: Petrogenetic and tectonic setting implications. *Precambrian Research*, **162**, 403–423.
- de Kock, G.S., Armstrong, R.A., Siegfried, H.P., Thomas, E., (2011). Geochronology of the Birim Supergroup of the West African craton in the Wa-Bolé region of west-central Ghana: implications for the stratigraphic framework. *Journal of African Earth Sciences*, **59**, 1-40.
- de Vries, S.T., Pryer, L.L., Fry, N., (2008). Evolution of Neoarchaean and Proterozoic basins of Australia. *Precambrian Research*, **166**, 39-53.
- Debat, P., Nikiéma, S., Mercier, A., Lompo, M., Béziat, D., Bourges, F., Roddaz, M., Salvis, S., Tolland, F., Wenmenga, U., (2003). A new metamorphic constraint for the Eburnean orogeny from Paleoproterozoic formations of the Man shield (Aribinda and Tampelga countries, Burkina Faso). *Precambrian Research*, **123**, 47-65.
- Dia, A., (1988). Caractères et significations des complexes magmatiques et métamorphiques du secteur de Sandikounda-Laminia (Nord de la boutonnière de Keïdougou, Est Sénégal). Un modèle géodynamique du Birimien de l’Afrique de l’Ouest. UCAD, Dakar.
- Dia, A., Van Schmus, W.R., Kröner, A., (1997). Isotopic constraints on the age and formation of a Paleoproterozoic volcanic arc complex in the Kedougou Inlier; eastern Senegal, West Africa. *Journal of African Earth Sciences*, **24**, 197-213.
- Dimroth, E., Cousineau, H., Leduc, M., Sansch, Y., (1978). Structure and organisation of Archean basalt flows, Rouyn Noranda area, Quebec, Canada. *Canadian Journal of Earth Sciences*, **15**, 902-918.
- Drummond, M.S., Defant, M.J., (1990). A model for trondhjemite-tonalite-dacite genesis and crustal growth via slab melting; Archean to modern comparisons. *Journal of Geophysical Research-Solid Earth*, **95**, 503–521.
- Eriksson, P. G., Schweitzer, J. K., Bosch, P. J. A., Schereiber, U. M., Van Deventer, J. L., Hatton, C. J. (1993). The Transvaal sequence: an overview. *Journal of African Earth Science*, **16**, 25-51.
- Expedition 309 Scientists, (2005). Superfast spreading rate crust 2: a complete in situ section of upper oceanic crust formed at a superfast spreading rate. IODP Preliminary Report 309. doi:10.2204/iodp.pr.309.2005.

- Feybesse, J.L., Billa, M., Guerrot, C., Duguey, E., Lescuyer, J.L., Milési, J.P., Bouchot, V., (2006). The Palaeoproterozoic Ghanaian province: Geodynamic model and ore controls, including regional stress modelling. *Precambrian Research*, **149**, 149-196.
- Fischer, R.V., Schmincke, H.U., (1994). Volcaniclastic sediment transport and deposition. In: Pye, K. (Ed.), *Sediment transport and depositional processes*. Blackwell Scientific Publishing, London, 351-388.
- Foley, S.F., Wheller, G.E., (1990). Parallels in the origin of the geochemical signatures of island arc volcanics and continental potassic igneous rocks: The role of residual titanites. *Chemical Geology*, **85**, 1-18.
- Govindaraju, K., (1994). Compilation of working values and sample description for 383 geostandards, special edition. *Geostandards Newsletter*, **18**, 1-158.
- Green, D.H., Ringwood, A. E., (1967). The genesis of basaltic magmas. *Contributions to Mineralogy and Petrology*, **15**, 103-190.
- Griffiths, R.W., Fink, J.H., (1992). Solidification and morphology of submarine lavas: a dependence on extrusion rate. *Journal of Geophysical Research*, **97**, 19729–19737.
- Gromet, L.P., Dymek, R.F., Haskin, L.A., Korotev, R.L., (1984). The “North American Shale Composite”: its compilation, major and trace element characteristics. *Geochimica et Cosmochimica Acta*, **48**, 2469-2482.
- Gueye, M., Ngom, P.M., Diène, M., Thiam, Y., Siegesmund, S., Wemmer, K., Pawlig, S., (2008). Intrusive rocks and tectono-metamorphic evolution of the Mako Paleoproterozoic belt (Eastern Senegal, West Africa). *Journal of African Earth Sciences*, **50**, 88-110.
- Gutzmer, J., Buekes, N. J. (1996). Mineral paragenesis of the Kalahari manganese field, South Africa. *Ore Geology Reviews*, **11**, 405-428.
- Haase, K. M., Stroncik, N. A., Henkinian, R., Stoffers, P., (2005). Nb-depleted andesites from the Pacific-Antarctic Rise as analogs for early continental crust. *Geology*, **33**, 921-924.
- Hammond, R., (1997). Workshop-Sanmatenga JV. Unpublished report, 4pp.
- Hastings, D., (1982). On the tectonics and metallogenesis of West Africa: A model incorporating new geophysical data. *Geoexploration*, **20**, 295-327.
- Hein, K.A.A., (2010). Succession of structural events in the Goren greenstone belt (Burkina Faso): Implications for West African tectonics. *Journal of African Earth Sciences*, **56**, 83-94.
- Hein, K.A.A., Morel, V., Kagoné, O., Kiemde, F., Mayes, K., (2004). Birimian lithological succession and structural evolution in the Goren Segment of the Boromo-Goren Greenstone Belt, Burkina Faso. *Journal of African Earth Sciences*, **39**, 1-23.
- Herrington, R., Maslennikov, V., Zaykov, V., Seravkin, I., Kosarev, A., Buschmann, B., Orgeval, J. J., Holland, N., Tesalina, S., Nimis, P., Armstrong, R., (2005). Classification of VMS deposits: Lessons from the south Uralides. *Ore Geology Reviews*, **27**, 203-237.

- Hill, B. M., Bickford, M. E., (2001). Paleoproterozoic rocks of central Colorado: Accreted arcs or extended older crust? *Geology*, **29**, 1015-1018.
- Hirdes, W., Davis, D.W., (2002). U-Pd geochronology of Palaeoproterozoic rocks in the southern part of the Kédougou-Kéniéba Inlier, Senegal, West Africa: Evidence for diachronous accretionary development of the Eburnean province. *Precambrian Research*, **118**, 83-99.
- Hirdes, W., Davis, D.W., Lüdtke, G., Konan, G., (1996). Two generations of Birimian (Paleoproterozoic) volcanic belts in north-eastern Côte d'Ivoire (West Africa): consequences for the 'Birimian Controversy'. *Precambrian Research*, **80**, 173-191.
- Hole, M., Saunders, A. D., Mariner, G. F., Tarney, J., (1984). Subduction of pelagic sediments: Implications for the origin of Ce-anomalous basalts from the Mariana Islands. *Journal of the Geological Society of London*, **51**, 303-323.
- Hottin, G., Ouedraogo, O.F., (1975). Notice explicative de la carte géologique à 1/1 000 000 de la République de Haute-Volta. Direction de la Géologie et des Mines, BRGM, 58pp.
- Hottin, G., Ouedraogo, O.F., (1992). Carte Géologique du Burkina Faso Échelle 1/1 000 000. 2 édition. Ouagadougou: Bureau des Mines et de la Géologie du Burkina (BUMIGEB).
- Ilboudo, H., (2010). Le Gite D'amas sulfure de Tiebélé (Burkina Faso - Afrique de L'Ouest). PhD thesis (Unpublished), Laboratoire de Géologie Minéralogie - Pétrophysique et Tectonique, Université de Ouagadougou, 158pp.
- Irvine, T.N., Barager, W.R.A., (1971). A guide to chemical classification of the common volcanic rocks. *Canadian Journal of Earth Sciences*, **8**, 523-548.
- Jones, J.G., (1969). Intratrabalvolcanoes of the Laugarvatn region, southwest Iceland. *Journal of the Geological Society of London*, **124**, 197–211.
- Junner, N.R., (1935). Gold in the gold coast, Ghana Geological Survey Memoir, No. 4, 67pp.
- Junner, N.R., (1940). Geology of the gold coast and Western Togoland (with revised geological map). Gold Coast Geological Survey Bulletin, No. 11, 40pp.
- Kepezhinskis, P., McDermott, F., Defant, M. J., Hochstaedter, A., Drummond, M. S., Hawkesworth, C. J., Koloskov, A., Maury, R. C., Bellon, H., (1997). Trace element and Sr-Nd-Pb isotopic constraints on a three-component model of Kamchatka Arc petrogenesis. *Geochimica et Cosmochimica Acta*, **61**, 577–600.
- Kitson, A.E., (1918). Annual Report. Gold Coast Geological Survey for 1916/17 (unpublished), Accra. 49 pp.
- Kříbek, B., Sýkorová, I., Machovič, V., Laufek, F., (2008). Graphitization of organic matter and fluid-deposited graphite in Palaeoproterozoic (Birimian) black shales of the Kaya-Goren greenstone belt (Burkina Faso, West Africa). *Journal of Metamorphic Geology*, **26**, 937-958.
- Lajoie, J., (1984). Volcaniclastic rocks. In Walker, R. G. (Ed.), *Facies Models: 2nd Edition*. Geological Association of Canada, Ontario, 39-52.

- Lajoie, J., Stix, J., (1992). Volcaniclastic rocks. In: Walker, R. G. and James, N. P. (Eds.), *Facies models, Response to sea level change*. Geological Association of Canada, Ontario, 101-118.
- Le Maitre, R.W., Bateman, P., Dudek, A., Keller, J., Lameyre Le Bas, M.J., Sabine, P.A., Schmid, R., Sorensen, H., Streckeisen, A., Woolley A. R., Zanettin, B., (1989). *A classification of igneous rocks and glossary of terms*. Blackwell, Oxford.
- Ledru, P., Pons, J., Milési, J.P., Feybesse, J.L., Johan, V., (1991). Transcurrent tectonics and polycyclic evolution in the lower Proterozoic of Senegal-Mali. *Precambrian Research*, **50**, 337–354.
- Leube, A., Hirdes, W., Mauer, R., Kesse, G.O., (1990). The early Proterozoic Birimian Supergroup of Ghana and some aspects of its associated gold mineralization. *Precambrian Research*, **46**, 139–165.
- Li, N., Bagas, L., Gallardo, L. A., Said, N., Diwu, C., McCuaig, T. C., (2013). Back-arc and post collisional volcanism in the Palaeoproterozoic Granites-Tanami Orogen, Australia. *Precambrian Research*, **224**, 570-587.
- Lombo, M., (2009). A model of subsidence of an oceanic plateau magmatic rocks in the Man-Leo Shield of the West African Craton Geodynamic evolution of the 2.25–2.0 Ga Palaeoproterozoic. In: Reddy, S.M., Mazumder, R., Evans, D.A.D., Collins, A.S. (Eds.), *Palaeoproterozoic Supercontinents and Global Evolution*. Geological Society, London, 231–254.
- Luddon, J. N., Thompson, G., (1979). An evaluation of the behaviour of rare earth elements during the weathering of sea-floor basalt. *Earth and Planetary Science Letters*, **43**, 85-92.
- Lüdtke, G., Hirdes, W., Konan, G., Kone, Y., Yao, C., Diarra, S., Zamble, Z., (1998). Géologie de la région Haute Comoe Nord—feuilles Kong (4b et 4d) et Tehini-Bouna (3a à 3d). Direction de la Géologie Abidjan Bulletin, 178.
- Lydon, J.W., (1988). Ore Deposit Models #14: Volcanogenic massive sulphide deposits, Part 2, Genetic models. *Geoscience Canada*, **15**, 43-65.
- Martin, H., (1994). The Archean grey gneisses and the genesis of continental crust. *Developments in Precambrian Geology*, **11**, 205–259.
- Martin, H., Smithies, R.H., Rapp, R., Moyen, J.F., Champion, D.C., (2005). An overview of adakite, tonalite–trondhjemite–granodiorite (TTG), and sanukitoid: relationships and some implications for crustal evolution. *Lithos*, **79**, 1–24.
- McCuaig, T.C., Kerrich, R., Xie, Q., (1994). Phosphorus and high field strength element anomalies in Archean high-magnesian magmas as possible indicators of source mineralogy and depth. *Earth and Planetary Science Letter*, **194**, 221-239.
- McFarland, D.M., Lawrence, A.R., (1998). *Historical Dictionary of Burkina Faso*, 2nd Edition. Lanham, Scarecrow Press, 360pp.

- McLennan, S.M., Hemming, S.R., Taylor, S.R. and Eriksson, K.A. (1995) Early Proterozoic crustal evolution: Geochemical and Nd-Pb isotopic evidence from metasedimentary rocks, southern North America. *Geochimica et Cosmochimica Acta*, **59**, 1153–1177.
- McLennan, S.M., Taylor, S.R., McCulloch, M.T., Maynard, J.B. (1990). Geochemical and Nd-Sr isotopic composition of deep-sea turbidites: Crustal evolution and plate tectonic associations. *Geochimica et Cosmochimica Acta*, **54**, 2015–2050.
- McPhie, J., Allen, R.L., (2003). Submarine, silicic, syn-eruptive pyroclastic units in the Mount Read volcanics, Western Tasmania: Influence of vent setting and proximity on lithofacies characteristics. American Geophysical Union, **140**, 245-258.
- McPhie, J., Doyle, M., Allen, R., (1993). Volcanic Textures: A guide to the interpretation of textures in volcanic rocks. CODES, Hobart. 197pp.
- Melcher, F., (1995). Genesis of chemical sediments in Birimian greenstone belts: evidence from gondites and related manganese-bearing rocks from northern Ghana. *Mineralogical Magazine*, **59**, 229-251.
- Melcher, F., Stumpfl, E.F., (1992). Chemical facies and gold mineralization in northern Ghana. *Berichte zur Lagerstätten-und Rohstoffforschung*, Hanover, 233 pp.
- Meschede, M., (1986). A method of discriminating between different types of mid-ocean ridge basalts and continental tholeites with the Nb-Zr-Y diagram. *Chemical Geology*, **56**, 207-218.
- Mickus, K., (2008). Regional gravity analysis of Burkina Faso: Implications for the location of metallic ore deposits. *Journal of African Earth Sciences*, **50**, 55-66.
- Milési, J.P., Feybesse, J.L., Ledru, P., Dommange, A., Ouedraogo, M.F., Marcoux, E., Prost, A., Vinchon, Ch., Sylvain, J.P., Johan, V., Tegyey, M., Calvez, J.Y., Lagny, P., (1989). West African gold deposits, in their lower Proterozoic lithostructural setting. *Chronique de la Recherché Minière*, **497**, 3-98.
- Milési, J.P., Ledru, P., Ankrah, P., Johan, V., Marcoux, E., Vinchon, C., (1991). The metallogenic relationship between Birimian and Tarkwaian gold deposits in Ghana. *Mineralium Deposita*, **26**, 228-238.
- Milési, J.P., Ledru, P., Feybesse, J.L., Dommange, A., Marcoux, E., (1992). Early Proterozoic ore deposits and tectonics of the Birimian orogenic belt, West Africa. *Precambrian Research*, **58**, 305-344.
- Mosier, D.L., Page, N.J., (1988). Descriptive and grade-tonnage models of volcanogenic manganese deposits in oceanic environments- a modification. U.S. Geological Survey Bulletin 1811, Washington, 28 pp.
- N'Gom, P.M., (1989). Caractères géochimiques des formations birrimiennes du supergroupe de Mako (Sabodala et ses environs). *Journal of African Earth Science*, **8**, 91-97.

- Naba, S., Lombo, M., Debat, P., Bouchez, J.L., Béziat, D., (2004). Structure and emplacement model for late-orogenic Palaeoproterozoic granitoids: the Tenkodogo-Yamba elongate pluton (Eastern Burkina Faso). *Journal of African Earth Sciences*, **38**, 41-57.
- Nesse, W.D., (2000). Introduction to mineralogy. Oxford University Press, New York, 442pp.
- Neumann, U., (1988). Mineralogie und genese der manganvorkommen in den Schiefergürteln von Nord-Nigeria. Ph.D thesis (unpublished), Universität Göttingen, 227pp.
- Nyame, F.K., 2008. Petrography and geochemistry of intraclastic manganese-carbonates from the ~2.2 Ga Nsuta deposit of Ghana: significance for manganese sedimentation in the Palaeoproterozoic of West Africa. *Journal of Earth Sciences* 50, 133-147.
- Orville, P.M., (1972). Plagioclase cation exchange equilibria with aqueous chloride solution; results at 700° and 2000 bars in the presence of quartz. *American Journal of Science*. **72**, 234-272.
- Palinkaš, L.A., Bermanec, V., Šoštarić, S.B., Kolar-Jurkovšek , T., Palinkaš, S.S., Molnar, F., Kniewald, G. (2008). Volcanic facies analysis of a subaqueous basalt lava-flow complex at Hrskovec, NW Croatia-Evidence of advanced rifting in the Tethyan domain. *Journal of Volcanology and Geothermal Research*, **178**, 644-656.
- Parfitt, E.A., Wilson, L., (2008). Fundamentals of physical volcanology. Blackwell Publishing, Oxford, 230pp.
- Pawlig, S., Gueye, M., Klischies, R., Schwarz, S., Wemmer, K., Siegesmund, S., (2006). Geochemical and Sr-Nd isotopic data on the Birimian of the Kedougou-Kenieba Inlier (Eastern Senegal): Implications on the Palaeoproterozoic evolution of the West African Craton. *South African Journal of Geology*, **109**, 411-427.
- Pearce, J. A., (1983). Role of the sub-continental lithosphere in magma genesis at active continental margins. In : Hawkesworth, C. J., and Norry, M. J., (Eds.), Continental basalts and mantle xenoliths. Shiva, Nantwich, 230-249.
- Pearce, J. A., Peate, D. W., (1995). Tectonic implications of the compositions of volcanic arc magmas. *Earth and Planetary Science Letters*, **23**, 251-285.
- Pearce, J.A., (1996). A user's guide to basalt discrimination diagrams. In: Wyman, D. A. (Ed.), Trace element geochemistry of volcanic rocks: applications for massive sulphide exploration. Geological Association of Canada - Short course notes **12**, 79-113.
- Pearce, J.A., Cann, J.R., (1973). Tectonic setting of basic volcanic rocks determined using trace element analysis. *Earth and Planetary Science Letters*, **19**, 290-300.
- Pearce, J.A., Lippard, S.J., Roberts, S., (1984). Characteristics of tectonic significance of supra-subduction zone ophiolites. In: Kokelaar, B. P., Howell, M. F., (Eds.), Marginal basin geology: Palo Alto, California. Blackwell Scientific Publications, 74-94.
- Pedersen, S.A.S., Craig, L.E., Upton, B.G.J., Ramo, O.T., Jepsen, H.F., Kalsbeek, F., (2002). Palaeoproterozoic (1740 Ma) rift-related volcanism in the Hekla Sund region, eastern North

- Greenland: field occurrence, geochemistry and tectonic setting. *Precambrian Research*, **114**, 327–346.
- Perrouty, S., Ailleres, L., Jessell, M. W., Baratoux, L., Bourassa, Y., (2012). Revised Eburnean geodynamic evolution of the gold-rich southern Ashanti belt, Ghana, with new field and geophysical evidence of pre-Tarkwaian deformations. *Precambrian Research*, **204**, 12-39.
- Peters, L. F. H., (2011). Geology of the eastern Markoye region, Oudalan-Gorouol greenstone belt, NE Burkina Faso. Honours thesis (Unpublished), University of the Witwatersrand, South Africa, 61pp.
- Piché, M., Jébrak, M., (2006). Determination of alteration facies using the normative mineral alteration index: Selbaie Cu-Zn deposit, northern Abitibi greenstone belt, Canada. *Canadian Journal of Earth Sciences*, **43**, 1877-1885.
- Pons, J., Barley, P., Dupuis, D., Léger, J.M., (1995). Mechanisms of pluton emplacement and structural evolution of a 2.1 Ga juvenile continental crust: the Birimian of south western Niger. *Precambrian Research*, **70**, 281-301.
- Pouclet, A., Vidal, M., Delor, C., Simeon, Y., Alric, G., (1996). Le volcanisme birimien du nord-est de la Côte-d'Ivoire mise en évidence de deux phases volcano tectoniques distinctes dans l'évolution géodynamique du Paleoprotérozoïque. *Bulletin de la Société Géologique de France*, **167**, 529–541.
- Ringwood, A. E., Kesson, S. E., Hibberson, W., Ware, N., (1992). Origin of kimberlites and related magmas. *Earth and Planetary Science Letters*, **113**, 521-538.
- Robbins, B., Sandstål, N.R., Furnes, H., De Wit, M., (2010). Flow banding in basaltic pillow lavas from the Early Archean Hooggenoeg Formation, Barberton Greenstone Belt, South Africa. *Bulletin of Volcanology*, **72**, 579-592.
- Roberts, R.G., (1996). A report on aspects of the geology and gold mineralisation in the Komsilga-Liliga district, Burkina Faso, Sanmatenga Joint Venture. Unpublished report to Randgold Resources Pty. Ltd. by R. Gwilym Roberts of the University of Waterloo, Ontario.
- Rollinson, H.R., (1993). Using geochemical data: evaluation, presentation, interpretation. Pearson-Prentice Hall, London, 352 p.
- Roy, S., (1968). Mineralogy of the different genetic types of manganese deposits. *Economic Geology*, **60**, 760-786.
- Roy, S., (1973). Genetic studies on the Precambrian manganese formations of India with particular reference to the effects of metamorphism. UNESCO, Earth Science Series, **9**, 229-242.
- Roy, S., (1981). Manganese deposits. Academic Press, London, 458 pp.
- Roy, S., Purkait, P. K., (1968). Mineralogy and genesis of the metamorphosed manganese silicate rocks (gondite) of Gowari Wadhona, Madhya Pradesh, India. *Contributions to Mineralogy and Petrology*, **20**, 86-114.

- Ryerson, F.J., Watson, E.B., (1987). Rutile saturation in magmas: Implications for Ti-Nb-Ta depletion in island-arc basalts. *Earth and Planetary Science Letters*, **86**, 225–239.
- Sajona, F.G., Maury, R.C., Bellon, H., Cotten, J., DeFant, M.J., Pubellier, M., (1993). Initiation of subduction and the generation of slab melts in western and eastern Mindanao, Philippines. *Geology*, **21**, 1007–1010.
- Saunders, A.D., Norry, M.J., Tarney, J., (1991). Fluid influence on the trace element compositions of subduction zone magmas. *Royal Society of London Philosophical Transactions*, **335**, 377–392.
- Saunders, A.D., Tarney, J., (1984). Geochemical characteristics of basaltic volcanism within back-arc basins. *Geological Society, London, Special Publications*, **16**, 59-76.
- Schwartz, M.O., Melcher, F., (2003). The Perko Zinc deposit, Burkina Faso. *Economic Geology*, **98**, 1463-1485.
- silicate glass in a spinel lherzolite xenolith from Yemen. *Chemical Geology*, **176**, 51-72.
- Simoko, N., (2012). Petrography, geochemistry and structure of the Pissila batholiths and Saaba Zone gneisses. Honours thesis (Unpublished), University of the Witwatersrand, South Africa, 61pp.
- Smellie, J.L., Hole, M.J., (1997). Products and processes in Pliocene-recent, subaqueous to emergent volcanism in the Antarctic Peninsula: examples of englacial Surtseyan volcano construction. *Bulletin of Volcanology*, **58**, 628-646.
- Stern, R.A., Syme, E. C., Bailes, A. H., Lucas, S. B., (1995). Paleoproterozoic (1.90-1.86 Ga) arc volcanism in the Flin Flon Belt, Trans-Hudson Orogen, Canada. *Contributions to Mineralogy and Petrology*, **119**, 117-141.
- Streckeisen, A., (1976). To each plutonic rock its proper name. *Earth Sciences Review Letters*, **12**, 1-33.
- Sylvester, P.J., Attoh, K., (1992). Lithostratigraphy and composition of 2.1 Ga greenstone belts of the West African Craton and their bearing on crustal evolution and the Archean-Proterozoic boundary. *Journal of Geology*, **100**, 377–393.
- Tarney, J., Saunders, A.D., Mattey, D.P., Wood, D.A., Marsh, N.G., (1981). Geochemical aspects of back-arc spreading in the Scotia Sea and western Pacific. *Philosophical Transactions of the Royal Society, London*, **A300**, 263-285.
- Taylor, B., Karner, G.D., (1983). On the evolution of marginal basins. *Reviews of Geophysics and Space Physics*, **21**, 1727-1 741.
- Taylor, P.N., Moorbat, S., Leube, A., Hirde, W., (1992). Early Proterozoic crustal evolution in the Birimian of Ghana: constraints from geochronology and isotope geochemistry. *Precambrian Research*, **56**, 97–111.
- Thiéblemont, D., Goujou, J.C., Egal, E., Cocherie, A., Delor, C., Lafon, J.M., Fanning, C.M., (2004). Archaean evolution of the Leo Rise and its Eburnean reworking. *Journal of African Earth Sciences*, **39**, 97-104.

- Tshibubudze, A., Hein, K.A.A., (2013). Structural setting of gold deposits in the Oudalan-Gorouol greenstone belt east of the Markoye Shear Zone, West African craton. *Journal of African Earth Sciences*, **80**, 31-47.
- Tshibubudze, A., Hein, K.A.A., Marquis, P., (2009). The Markoye Shear Zone in NE Burkina Faso. *Journal of African Earth Sciences*, **55**, 245-256.
- Tshibubudze, A., Hein, K.A.A., Peters, L.F.H., Woolfe, A.J., McCauig, T.C., (2013). Oldest U-Pb crystallization age for the West African craton from the Oudalan-Gorouol belt of Burkina Faso. *South African Journal of Geology*, **116**, 169-181.
- Väisänen, M., Westerlund, G., (2007). Palaeoproterozoic mafic and intermediate metavolcanic rocks in the Turku area, SW Finland. *Bulletin of the Geological Society of Finland*, **79**, 127-141.
- Vidal, M., and Alric, G., (1994). The Palaeoproterozoic (Birimian) of Haute-Comoé in the West African craton, Ivory Coast: a transitional back-arc basin. *Precambrian Research*, **65**, 207–229.
- Vidal, M., Gumiaux, C., Cagnard, F., Pouclet, A., Ouattara, G., Pichon, M., (2009). Evolution of a Paleoproterozoic “weak type” orogeny in the West African Craton (Ivory Coast). *Tectonophysics*, **477**, 145–159.
- Walker, R.G., (1992). Turbidites and submarine fans. In: Walker, R. G. and James, N. P. (Eds.), *Facies models, Response to sea level change*. Geological Association of Canada, Ontario, 239-263.
- WAXI, (2013). Confidential Final report, P934A West African Exploration Initiative, Stage 2, 924pp (with 917 pages of appendices).
- White, W.M., (2013). *Geochemistry*. Wiley-Blackwell. Oxford, 660pp.
- Wilson, M., (1989). *Igneous petrogenesis: A global tectonic approach*. Springer, The Netherlands, 466 p.
- Winchester, J.A., Floyd, P.A., (1976). Geochemical magma type discrimination; application to altered and metamorphosed basic igneous rocks, *Earth Planetary Sciences Letters*, **28**, 459-469.
- Wright, J.B., Hastings, D.A., Jones, W.B., Williams, H. R., (1987). *Geology and Mineral Resources of West Africa*. *Journal of African Earth Sciences*, **2**, 243 p.
- Zonou, S., (1987). Les formations leptyno-amphibolitiques et le complexe volcanique et volcanosédimentaire du Protérozoïque inférieur de Bouroum-nord (Burkina Faso – Afrique de l’Ouest): Etude pétrographique, géochimique approche pétrogénétique et évolution géodynamique. Université de Nancy I, France, 329pp.

Appendix A
Station point field descriptions

January 2013 field season

Field descriptions

Station Point	GPS Co-ordinates			Rock Type	Description
G12/001	30P	703502	1446724	Chlorite-amphibole schist	Amphibolite facies, deformed
G12/002	30P	702984	1446629	Basalt	Pillows, vesicles, carbonaceous quartz veins
G12/003	30P	702832	1446448	Basalt-andesite	Deformed, more silicic
G12/004	30P	702744	1446079	Mn-Fe-rich sediments	Slump folding
G12/005	30P	702704	1445973	Intercalated volcaniclastic greywackes and hyaloclastites	Deformed
G12/006	30P	702344	1446021	Fe-rich sediments	
G12/007	30P	696828	1443986	Greywacke-gritstone (previously mapped as dacite)	Fragments, grains
G12/008	30P	694317	1443450	Hyaloclastic basalt	Fragments, elongate gas tracks (vesicles), pillows
G12/009	30P	693302	1444147	Basalt-andesite	Pseudo pillows, vesicles
G12/010	30P	693325	1444398	Basalt	Pseudo pillows
G12/011	30P	693247	1444459	Pillow basalt	Fragments, carbonate-in filled hyaloclastic material
G12/012	30P	678993	1467130	Basalt	Vesicles, contraction fractures, pseudo pillows

G12/013	30P	678818	1467063	Pillow basalt	Tension fractures, undefined pillows
G12/014	30P	678440	1466962	Basalt	Braided style flow textures, vesicles, near shear zone
G12/015	30P	678378	1468663	Hyaloclastic basalt	Fragments, no pillows, near shear zone
G12/016	30P	678189	1466711	Variolitic pillow basalt	Pillows not well defined, variole clusters, volcanic. Derived fragments
G12/017	30P	677996	1466647	Banded chert	Partially brecciated from shear zone
G12/018	30P	675652	1466804	Basalt	Chlorite and epidote veining, carbonate filled fractures, dark concentric rings, vesicles
G12/019	30P	673543	1439364	Variolitic basalt-andesite (chlorite-hornblende schist)	White ellipsoidal varioles, in contact aureole of Sillimidougou pluton
G12/020	30P	696458	1458855	Basalt	Chloritised and silicified, deformed, vesicles
G12/021	30P	695837	1459138	Basalt	Chloritised, hyaloclastic, minor presence of vesicles
G12/022	30P	695793	1459255	Basalt	Lots of large vesicles, deformed, chlorite-amphibole rich
G12/023	30P	709027	1423835	Graphitic siltstone	Slump folding, Fe-Mn rich
G12/024	30P	709775	1423996	Pyroclastic basalt-andesite	Variety of angular fragments/shards
G12/025	30P	693290	1444191	Pillow basalt	Well-formed pillows, possible sub-marine deposition, no vesicles or hyaloclastic material

March-April 2013

Field descriptions

Station Point	GPS Co-ordinates			Rock Type	Description
G12-02-001	30P	702395	1424608	Ferricrete	SW quadrant of GB (Lougouma)
G12-02-002	30P	704134	1425557	Ferricrete	On NE traverse
G12-02-003	30P	703585	1426248	Basalt	Large vesicles (2cm), late fluid infill (veining)
G12-02-004	30P	703584	1426338	Basalt	Hyaloclastic, pseudo pillow with gas tracks, amygdales/pyroclastic material aligning
G12-02-005	30P	705231	1425791	Basalt	Not in situ, developed pillows, cross-cutting veins, hyaloclastite, quartz amygdales (5-8cm)
G12-02-006	30P	705045	1425704	Siltstone	Quartz veins in outcrop cross-cutting, fine-grained, reddish-brown, cleavage and folding, outcrop partially destroyed due to artisanal mining
G12-02-007	30P	705550	1425934	Basalt	Amygdales aligned, hyaloclastite, gas expansion->fracturing, quartz infill,
G12-02-008	30P	709181	1428595	Dyke	Coarse-grained, crystalline, plagioclase, hornblende, chlorite, trending 161-341 degrees.
G12-02-009	30P	709452	1428840	Dyke	Coarser grained, plagioclase, chlorite, (pyroxene), hornblende
G12-02-010	30P	709616	1429270	Greywacke	Fracturing and veining, fragments rounded-angular, 2mm-3cm
G12-02-011	30P	709882	1430136	Amphibolite	Metamorphosed Basalt OR intrusive (fine-grained with hornblende blades and coarser grained with bladed hornblende)
G12-02-012	30P	709831	1430264	Amphibolite	As above
G12-02-013	30P	709739	1430851	Amphibolite	Laterally extensive unit (approx. 300-400m)

Station Point	GPS Co-ordinates			Rock Type	Description
G12-02-014	30P	711294	1431532	Siltstone with chert interbeds	Deformed (northwest-trending cleavage)
G12-02-015	30P	711629	1431822	Fe-rich chemical sediments with chert layers	Botryoidal texture, Fe-rich, quartz-veining, slump folding, ankerite weathering (BIF-style)
G12-02-016	30P	711914	1431828	Shear zone	
G12-02-017	30P	712130	1431987	Amphibolite	Coarse-grained (dyke?)
G12-02-018	30P	712352	1431991	Amphibolite (basalt)	Hyaloclastic, vesicles, high met. -> crystal growth, alignment of crystals.
G12-02-019	30P	712474	1431854	Graphitic shales (chemical sediments)	Deformed, Fe-rich, graphite-rich, fine-grained
G12-02-020	30P	712916	1431713	Basalt	Deformed (cleaved & flattened), fine-grained, chlorite, plagioclase, amphibole-bearing, vesicles and gas tracks, pseudo pillows
G12-02-021	30P	713145	1431643	Basalt	Increased % of epidote in veins, hyaloclastic, gas bubbles
G12-02-022	30P	713245	1431519	Basalt	Vesicles, amygdales
G12-02-023	30P	713501	1431176	Basalt	Cleaved, northwest trending flattening (ne compression)
G12-02-024	30P	713603	1431238	Basalt	Last stop on traverse, highly deformed

Station Point	GPS Co-ordinates			Rock Type	Description
G12-02-025	30P	706667	1423173	Basalt	Vesicles, amygdales, gas tracks (outcrop very weathered)
G12-02-026	30P	706792	1423420	Basalt	Better defined gas tracks & vesicles, pillows in 3D, chert & ferricrete float around
G12-02-027	30P	706940	1423724	Ferricrete	
G12-02-028	30P	707026	1423906	Basalt/Chemical sediments	Similar textures to basalt, highly weathered, Fe-rich (reddish colour)
G12-02-029	30P	707009	1423936	Basalt/Chemical sediments	Similar textures to basalt, highly weathered, Fe-rich (reddish colour)
G12-02-030	30P	702957	1423554	Hyaloclastic basalt	Hyaloclastic (quartz & carbonate), carbonates weathered out, good exposure, epidote veining, lack of vesicles, no pillows (?Lava dumped quickly?)
G12-02-031	30P	710181	1424389	Volcaniclastic greywacke	Volcanic fragments vary in size (1-3 mm)
G12-02-032	30P	709279	1424708	Pyroclastic breccia	Volcanic fragments in basaltic/andesitic groundmass (coarse-grained amphibolite dyke cross-cuts, same as further NE)
G12-02-033	30P	709521	1424918	Pyroclastic breccia	Volcanic fragments in basaltic/andesitic groundmass

Station Point	GPS Co-ordinates			Rock Type	Description	
G12-02-034	30P	707113	1424697	Ferricrete		
G12-02-035	30P	707346	1425026	Fe-rich graphitic shales with chert layers and greywacke interbeds	Chert beds, slump folding, fine-grained, black-red-grey in colour, trending NW, quartz veins	
G12-02-036	30P	707539	1425072	Dyke	Plagioclase, chlorite, quartz, (pyroxene) -> petrography needed	
G12-02-037	30P	707496	1425279	Dyke and buck quartz	Coarsening northwards, trending NW (~ 58 degrees), buck quartz same direction	
G12-02-038	30P	706953	1425326	Chert-Fe-chemical sediments	NW trending, Fe-rich, lacking graphite	
G12-02-039	30P	706989	1425023	Dyke	Finer-grained, plagioclase, biotite, hornblende, (pyroxene), Fe-rich-> weathering crust hematised	
G12-02-041	30P	702502	1429132	Ferricrete	Eastern side of railway	
G12-02-042	30P	703464	1430479	Siltstone with chert & greywacke interbeds	Highly weathered and bleached, adjacent to railway, deformed (cleavage & tight isoclinal folds), poor exposure- Cleavage: 090/72	
G12-02-043	30P	706895	1437356	Ferricrete		

Station Point	GPS Co-ordinates			Rock Type	Description
G12-02-044	30P	701716	1430843	Ferricrete	
G12-02-045	30P	701204	1430372	Fe-rich chemical sediments	
G12-02-046	30P	701140	1430125	Fe-rich shales with greywacke & siltstone interbeds	Lacks graphite, makes up prominent ridges, thick succession(300-400 m lateral distance), fine-grained
G12-02-047	30P	700412	1430174	Basalt	Hyaloclastic material, minor veining, gas tracks & fractures present (low abundance), gas bubbles (1-2 mm) present, chlorite, plagioclase, sulfides.
G12-02-048	30P	699650	1429026	Dyke (?)	Coarser-grained than basalt, chlorite, plagioclase, pyroxene, (sulphides, biotite), crystals ~ 1- 3 mm (needs petrography)
G12-02-049	30P	699909	1428706	Siltstone intercalated with greywacke	Deformed (cleavage & folding), increase in quartz float around ridge, ridge looks like macro-boudin, structural influence, average cleavage: 053/58; fractures in opposite direction present
G12-02-050	30P	700000	1428808	Basalt	Deformed, fine-grained, chlorite, plagioclase, ~ sulfides, not good for sampling
G12-02-051	30P	699755	1429095	Greywacke/Siltstone	Fe-rich, deformed, POOR exposure, very weathered (not sure on identification)
G12-02-052	30P	699566	1429980	Basalt	
G12-02-053	30P	699504	1430061	Basalt	Homogenous, minor hyaloclastic material, chlorite, plagioclase, sulfides

Station Point	GPS Co-ordinates			Rock Type	Description
G12-02-054	30P	700508	1435915	Basalt	Hyaloclastic (quartz infill), 'braided' texture (flow texture)
G12-02-055	30P	700472	1435863	Basalt	50-70 m from last outcrop- amygdales and vesicles (1-5 mm) plentiful, gas tracks, chlorite, plagioclase, (amphibole)-> very fine-grained
G12-02-056	30P	700162	1435621	Ferricrete	
G12-02-057	30P	699990	1435556	Hyaloclastic basalt	Quartz-carbonate material, very fine-grained (glassy)
G12-02-058	30P	699733	1435378	Ferricrete	
G12-02-059	30P	699822	1435306	Basalt	Very deformed (cleaved), located in river channel
G12-02-060	30P	699558	1435266	Dyke (?)	Appears to be same mineral assemblage as basalt but coarser-grained (chlorite, plagioclase, (pyroxene), crystal size- 1-2 mm
G12-02-061	30P	699312	1435190	Basalt	Located in river channel, deformed, hyaloclastic, very fine-grained
G12-02-062	30P	698384	1434809	Basalt	Hyaloclastic, slightly deformed, flow texture
G12-02-063	30P	697815	1434195	Siltstone with greywacke and Fe-rich chemical sediments	Carbonates weathered out, slump folding, deformed (cleavage), unit continues to the flat land (westwards) strikes N-S

Station Point	GPS Co-ordinates			Rock Type	Description
G12-02-064	30P	706417	1443224	Hyaloclastic basalt	Deformed, quartz veining, epidote veining
G12-02-065	30P	706200	1443085	Hyaloclastic basalt	Vesicles (1-3 cm), (pseudo) pillows formed-> deformed-> elongated, gas tracks, pillows do not easily show facing (N-NNE)
G12-02-066	30P	706077	1442978	Basalt	Same as above, cross-cutting quartz & carbonate veins, epidote veins, vesicles abundant
G12-02-067	30P	705953	1442951	Hyaloclastic pillow basalt	More hyaloclastic brecciation, vesicles, quartz "clasts" present tracking up length of pillow, deformed
G12-02-068	30P	705632	1442485	Basalt (Amphibolite)	Vertical, cleaved slabs of basalt, cleavage: NW direction-> stress direction = NE, vesicles, hyaloclastite
G12-02-069	30P	704973	1441425	Hyaloclastic basalt	Quartz-carbonate, increase in epidote, deformed but can see textures well, vesicles-amygdales
G12-02-070	30P	704690	1441380	Hyaloclastic basalt	Same as above, cleavage: NW direction
G12-02-071	30P	704529	1441372	Basalt	At contact between basalt and sedimentary unit
G12-02-072	30P	704412	1441370	Intercalated sequence of greywacke, siltstone & Fe-rich shales	Fe-rich shales (chemical sediments), siltstone & greywacke also Fe-rich, fine-grained, deformed, carbonate minerals weathered out
G12-02-073	30P	705293	1441888	Intercalated sequence of greywacke & Fe-rich graphitic shales	On track through basalt ridges (along traverse), folded, cleaved, very fine-grained, small outcrop, outcrop further north is deformed

Station Point	GPS Co-ordinates			Rock Type	Description
G12-02-074	30P	704682	1444619	Hyaloclastic basalt	Very deformed, quartz-carbonate in filled hyaloclastic material, epidote-chlorite-plagioclase-amphibole-rich, flow texture, possible pillows (out of situ), buck quartz veins abundant (trending NW-SE)
G12-02-075	30P	704422	1444275	Hyaloclastic basalt	Deformed, chlorite-amphibole-rich (upper greenschist->amphibolite facies), fine-grained
G12-02-076	30P	703934	1443661	Fe-Mn-rich graphitic shales	Chert & quartz rich, fine-grained, carbonate-rich layers (weathering), botryoidal texture, black-red in colour (hematitisation), slump folding, deformed, ridge approximately 50 m wide
G12-02-077	30P	704083	1443129	Ferricrete	
G12-02-078	30P	703722	1443844	Fe-rich chemical sediments intercalated with siltstone	Siltstones show well developed cleavage planes (no bedding), chemical sediments show bedding (see field notebook for measurements)
G12-02-079	30P	703512	1444037	Fe-rich chemical sediments intercalated with siltstone	Along strike (see field notebook for measurements)
G12-02-080	30P	703388	1444244	Fe-rich chemical sediments intercalated with siltstone	Along strike (see field notebook for measurements)
G12-02-081	30P	703501	1444250	Fe-rich chemical sediments intercalated with siltstone	Along strike (see field notebook for measurements)
G12-02-082	30P	703067	1444147	Greywacke intercalated with siltstone	Very deformed-cleavage (lots of compaction-much like the basalt in area)

Station Point	GPS Co-ordinates			Rock Type	Description
G12-02-083	30P	703920	1446075	Hyaloclastic basalt	Deformed, abundance of vesicles, epidote-rich, quartz veins cross-cutting, deformed (pseudo) pillows->get smaller as move NE
G12-02-084	30P	703649	1445847	Hyaloclastic basalt	Deformed, epidote veins & epidote-rich, quartz-carbonate in filled hyaloclastite, buck quartz-vein trending same direction (NW)->possible addition of silica to basalts
G12-02-085	30P	703421	1445760	Hyaloclastic basalt	Deformed, in river channel
G12-02-086	30P	703104	1445656	Basalt	Highly deformed, at contact with chemical sediments
G12-02-087	30P	703012	1445647	Fe-rich chemical sediments	Silica-rich, carbonate-rich, slump folding, ridge trending @ 161 degrees, dipping east between 75-85 degrees, botryoidal texture
G12-02-088	30P	702988	1445503	Siltstone intercalated with greywacke	Deformed, beautifully folded, sigma 1 = NE-SW, cleavage developed well, sediments are Fe-rich, carbonate-rich (due to colouration-red, white)also yellow
G12-02-089	30P	702889	1445451	Fe-rich chemical sediments	Same description-> last 3 station points indicate intercalated sequence
G12-02-090	30P	702641	1445482	Hyaloclastic basalt	Deformed, epidote-chlorite-rich, quartz-carbonate in filled hyaloclastite, vesicles & amygdales, unit trending at approximately 175 degrees.
G12-02-091	30P	702541	1445062	Intercalated unit of siltstone, greywacke and Fe-rich chemical sediments	Deformed, fine-grained, folds and cleavage visible

Station Point	GPS Co-ordinates			Rock Type	Description
G12-02-092	30P	702492	1448025	Hyaloclastic basalt	Deformed, structure induced fabric, quartz-carbonate in filled hyaloclastic brecciation, quartz-carbonate cross-cutting veins, epidote veining, large gas tracks, thin veining in alignment (see picture), epidote-rich
G12-02-093	30P	696678	1444306	Volcaniclastic-greywacke	Variety of grains, poorly sorted, some elongate grains of chert (up to 3.5 cm), grain size: 1mm-3.5cm
G12-02-094	30P	696314	1443395	Greywacke	Carbonate-rich, coarse-grained, deformed (cleavage-trending NW), chert interbeds
G12-02-095	30P	695421	1443258	Basalt	Fine-grained, vesicles, lacks other textures (homogenous), contains pyrite and chalcopyrite
G12-02-096	30P	694686	1443104	Basalt	Amygdales present, medium-grained, contains sulphides and iron oxides visible in hand sample, cross-cut by quartz veins, epidote-chlorite rich.
G12-02-097	30P	694393	1442727	Pillow basalt	Pillows developed (not well), facing= E-ENE, vesicles, epidote-rich, concentric flow bands, sulfides
G12-02-098	30P	693240	1443462	Pillow basalt	Hyaloclastic material, fairly well defined pillows, concentric flow bands, vesicles & amygdales, epidote-rich

Station Point	GPS Co-ordinates			Rock Type	Description
G12-02-099	30P	696917	1441719	Hyaloclastic pillow basalt	Small pillows (10 cm), vesicles, gas tracks (parallel), teeth - shaped texture (see picture), facing NE-E
G12-02-100	30P	696748	1441633	Hyaloclastic pillow basalt	Well-developed pillows (mostly small-10 cm), outlined by lots of hyaloclastic brecciation
G12-02-101	30P	696416	1441547	Hyaloclastic pillow basalt	Same description as above
G12-02-102	30P	696163	1441606	Hyaloclastic basalt	Slightly deformed (zone of deformation begins), otherwise no significant change except lack of pillows (possibly due to deformation?)
G12-02-103	30P	696142	1441631	Quartz vein	Quartz crystals visible, weathered surface does not look like quartz vein-looks volcanic, only small outcrop amongst basalt, very weathered (hard to tell other mineralogy)
G12-02-104	30P	695831	1441613	Dyke	Crystalline (crystals are small but visible with naked eye), quartz, plagioclase, chlorite, (pyroxene?)> Petrography needed!
G12-02-105	30P	695541	1441893	Greywacke	Deformed, highly weathered (not even sure if it is a sediment (most of ridge is ferricrete)

Station Point	GPS Co-ordinates			Rock Type	Description
G12-02-106	30P	692909	1440157	Ferricrete	Walked on ferricrete since traverse started
G12-02-107	30P	694916	1440335	Hyaloclastic pillow basalt	Vesicles/amygdales (1-2 mm), minor hyaloclastic material, chlorite-epidote-clinopyroxene-plagioclase rock mineralogy
G12-02-108	30P	695052	1440422	Hyaloclastic pillow basalt	Vesicles (1-2 mm), looks like pillows tried to develop
G12-02-109	30P	695209	1440586	Hyaloclastic basalt	Partially hyaloclastic, lots of vesicles, chlorite-epidote-rich, no significant change
G12-02-110	30P	694964	1440271	Hyaloclastic pillow basalt	Well-developed pillows (facing N-ENE); size ranges from a few cm to 60-70 cm across, concentric flow texture, quartz-carbonate hyaloclastite between pillows, vesicles present
G12-02-111	30P	694536	1439962	Intercalated unit of siltstone, greywacke & Fe-rich shale units	Ferricrete-capped ridge, sediments deformed, NW-trending cleavage, sediments are fine-grained-medium-grained, ridge trends at 147 degrees (NW)

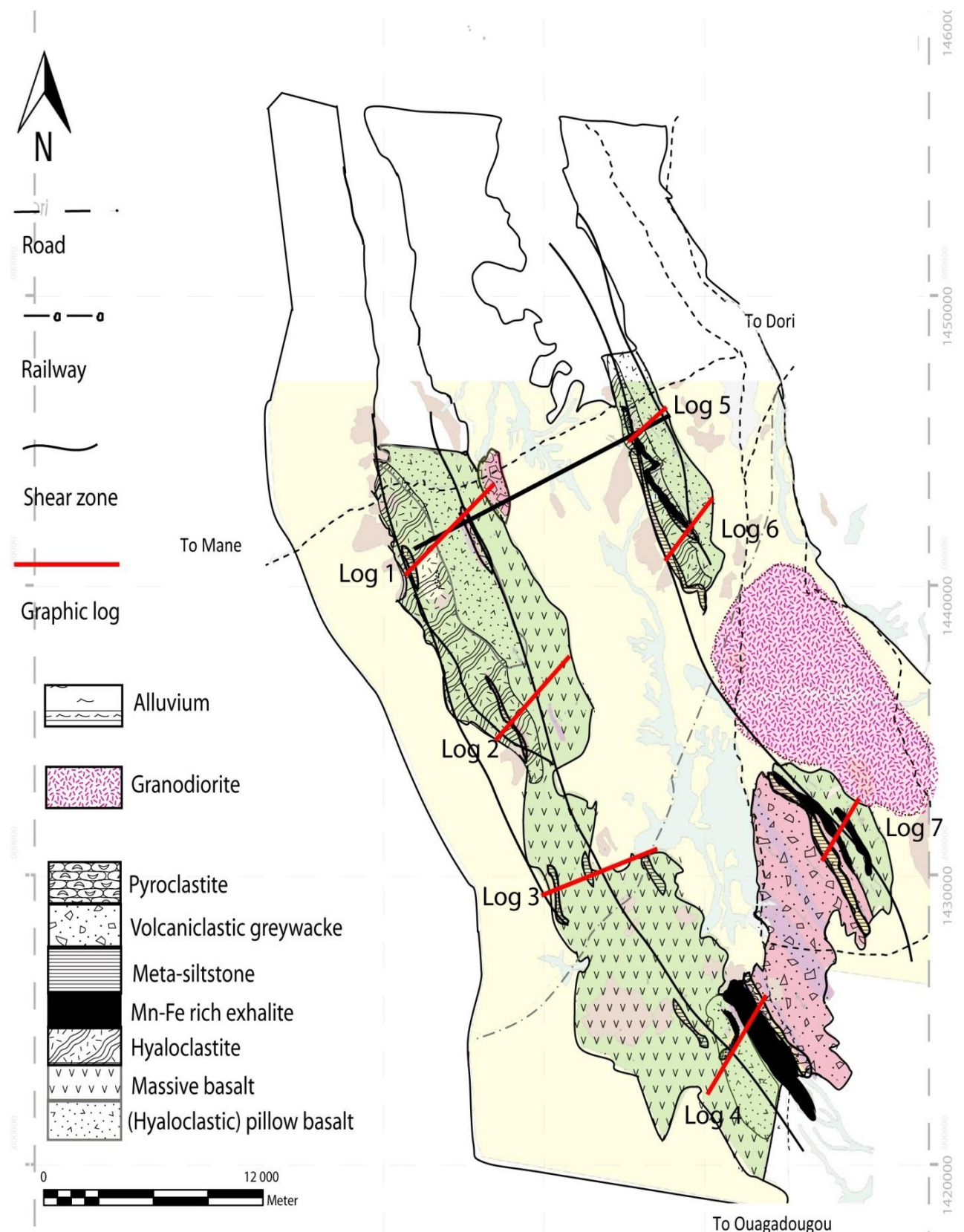
Station Point	GPS Co-ordinates			Rock Type	Description
G12-02-112	30P	709944	1433110	Fe-rich graphitic shale units with chert layers	Slump folded, bedding well defined (folded so no strike), silica-rich (chert interbeds & quartz veins), low-lying outcrop-> not prominent ridge, unit trending NW (127 degrees) and dipping 80-85 degrees NE
G12-02-113	30P	711118	1432916	Hyaloclastic basalt	Deformed, schistose, tiny outcrop (possibly near a fault plane), trending 118 degrees
G12-02-114	30P	711540	1432977	Aplite dyke	Small outcrop, weathered, quartz veins present, some crystals visible but there is added quartz, mineralogy: k-spar, plagioclase, quartz, and hornblende. Intrusive
G12-02-115	30P	712253	1433019	Granodiorite	Mafic xenoliths, mineralogy: hornblende; plagioclase; quartz; minor muscovite -> contact with Louda batholith
G12-02-116	30P	712255	1432474	Hyaloclastic basalt	Very deformed, vesicles, quartz-veins running through, cleavage trending NW
G12-02-117	30P	712206	1432215	Fe-rich graphitic shales	Unit trending NW, slump folded
G12-02-118	30P	709325	1430515	Volcaniclastic greywacke	Contains fragments, fine-grained-coarse-grained, quartz; mafic minerals; and pyrite (disseminated, but a lot of (10 %))
G12-02-119	30P	708845	1431001	Volcaniclastic greywacke	Conglomerate beds up to 1 m wide, same appearance as top of OGB, see notebook for measurements
G12-02-120	30P	710066	1430260	Volcaniclastic greywacke	Small outcrop, trends NW
G12-02-121	30P	708945	1428447	Volcaniclastic greywacke	Small outcrop near village of Boussouma & N3 (main road)

Station Point	GPS Co-ordinates			Rock Type	Description
G12-02-122	30P	709363	1425384	Dyke	Next to road, plagioclase-chlorite-hornblende-(pyroxene), medium-grained to coarse-grained
G12-02-123	30P	709313	1425307	Volcaniclastic greywacke	Dyke intruding greywacke
G12-02-124	30P	709509	1424822	Dyke	Same description, trends NW
G12-02-125	30P	709978	1424653	Volcaniclastic greywacke	Volcaniclastic fragments, thin (approximately 10 cm) conglomerate beds, bedding visible, as move north, strike changes from NW to N, see notebook for measurements
G12-02-126	30P	709365	1424791	Pyroclastic breccia	For sampling purposes, compared sample to known pyroclastic breccia

Station Point	GPS Co-ordinates			Rock Type	Description
G12-02-127	30P	710916	1430656	Greywacke with siltstone	Deformed, chert veins interbedded, trending approx. 121 deg. (NW-WNW), folded and cleaved, steeply dipping to the east, Fe-oxide rim around parts of greywacke
G12-02-128	30P	712818	1430908	Greywacke with graphitic shale	Makes up prominent ridges in region, trending 126 degrees (NW), chemical sediments intercalated with volcaniclastic sediments, Fe-oxide rim around greywacke boudins
G12-02-129	30P	712699	1430205	Fe-rich graphitic shales with graphitic siltstone & greywacke	Slump folded, botryoidal texture, Fe-rich, same unit of sediments (relatively thick succession)
G12-02-130	30P	709295	1427484	Hornblende-rich dyke	M/g-> c/g, c/g part has large & elongate hornblende crystals-large plagioclase crystals (0.5-3 cm), plagioclase-hornblende-chlorite-(pyroxene), petrography needed
G12-02-131	30P	705705	1424811	Pillow basalt	Pillows not well defined (pseudo-pillows), not hyaloclastic, chlorite-epidote-rich, pillows show facing: SW-W (wouldn't rely just on that)
G12-02-132	30P	705824	1424587	Fe-rich sediments	Fe-rich, greywacke intercalated with siltstones

Appendix B

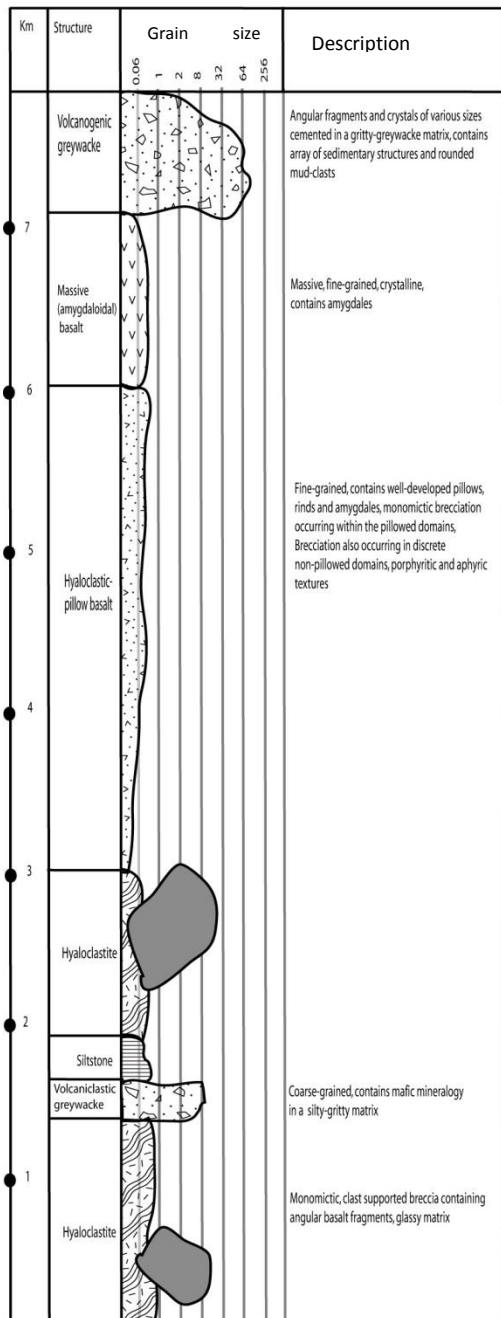
Graphic logs



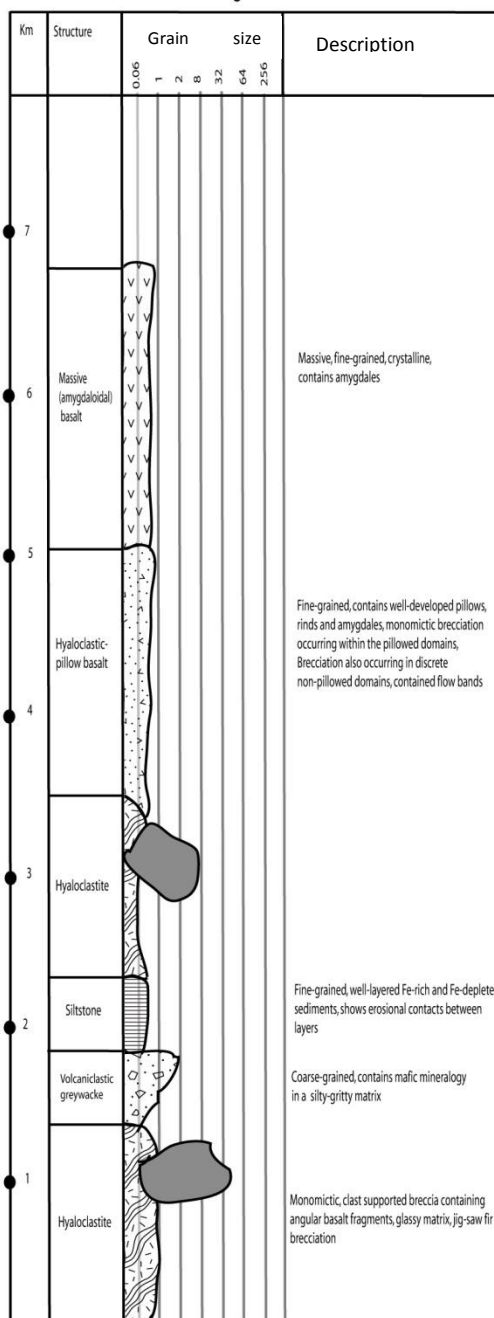
Volcanic facies map of the southern Goren greenstone belt
(dykes not included)

Figure B1. Volcanic facies map with traverse lines for graphic logs indicated.

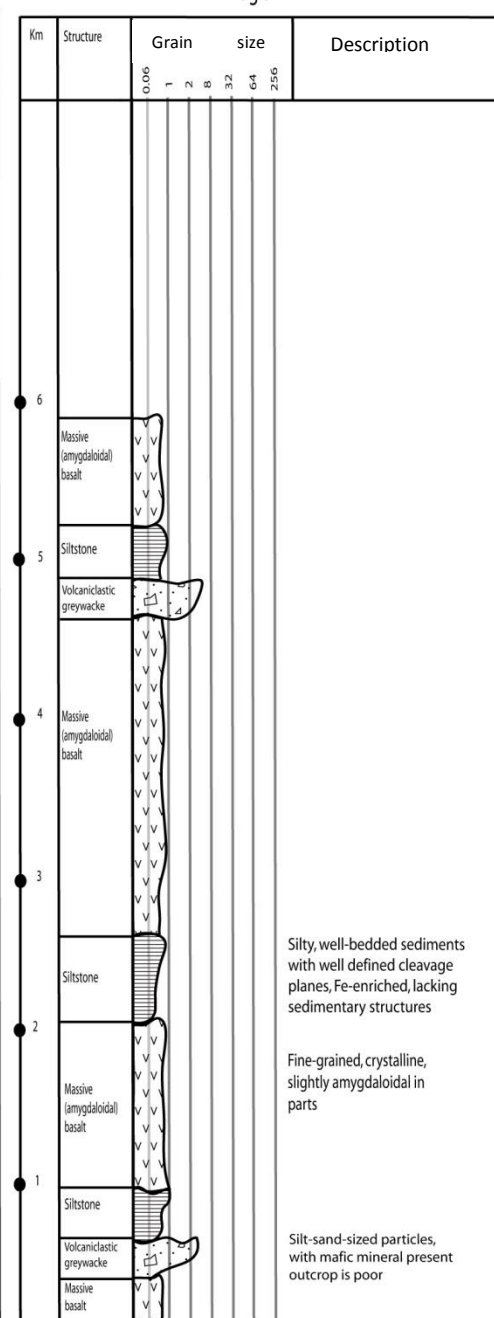
Log 1



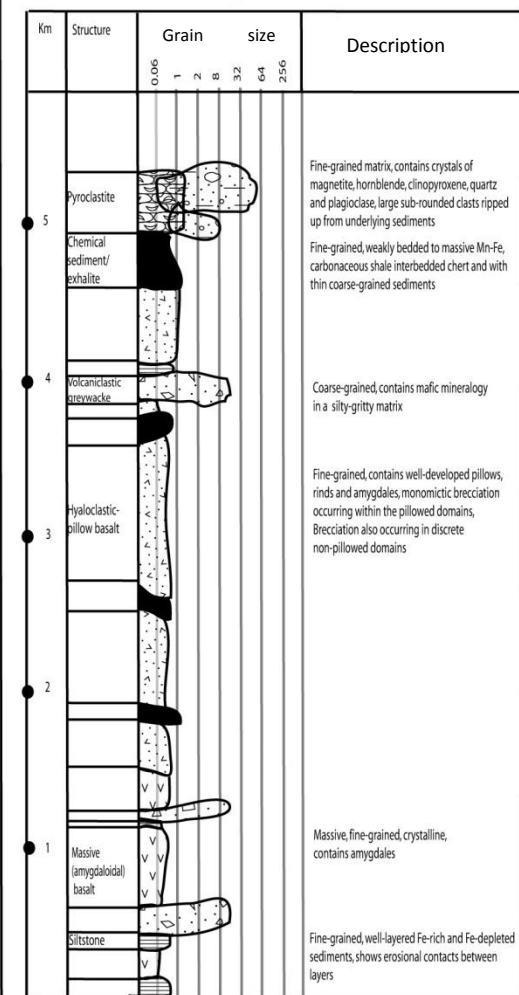
Log 2



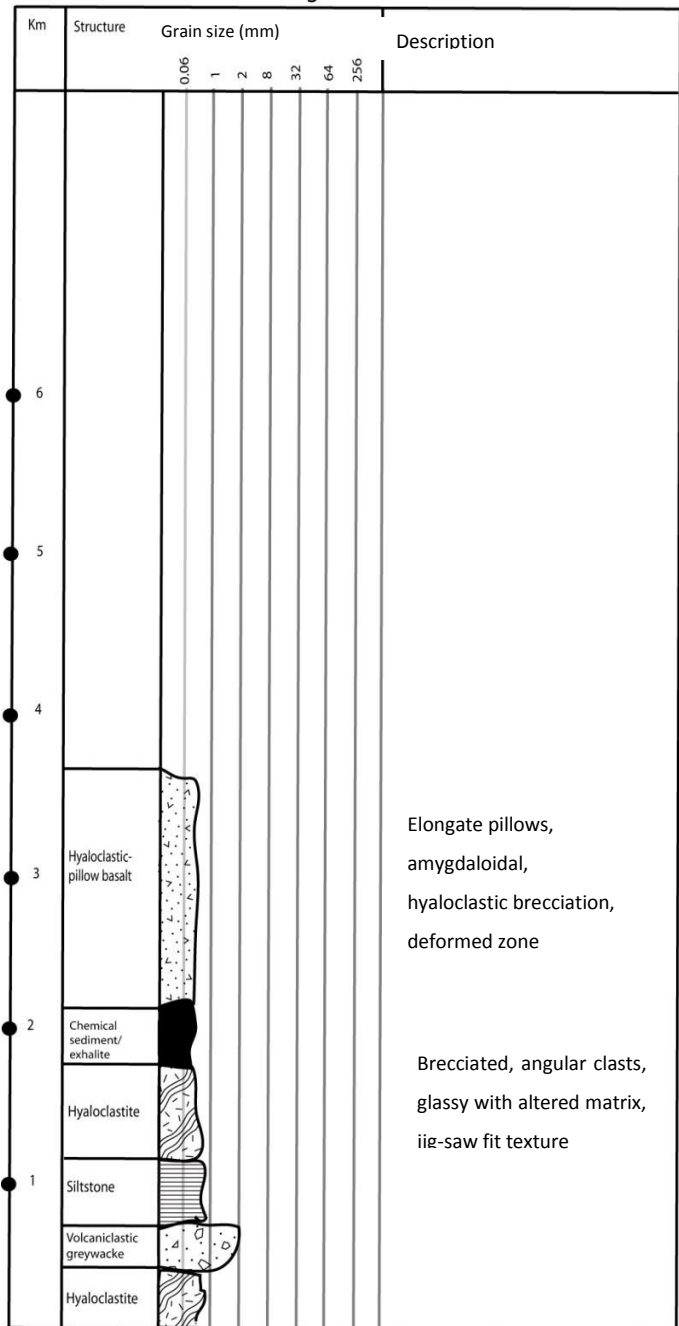
Log 3



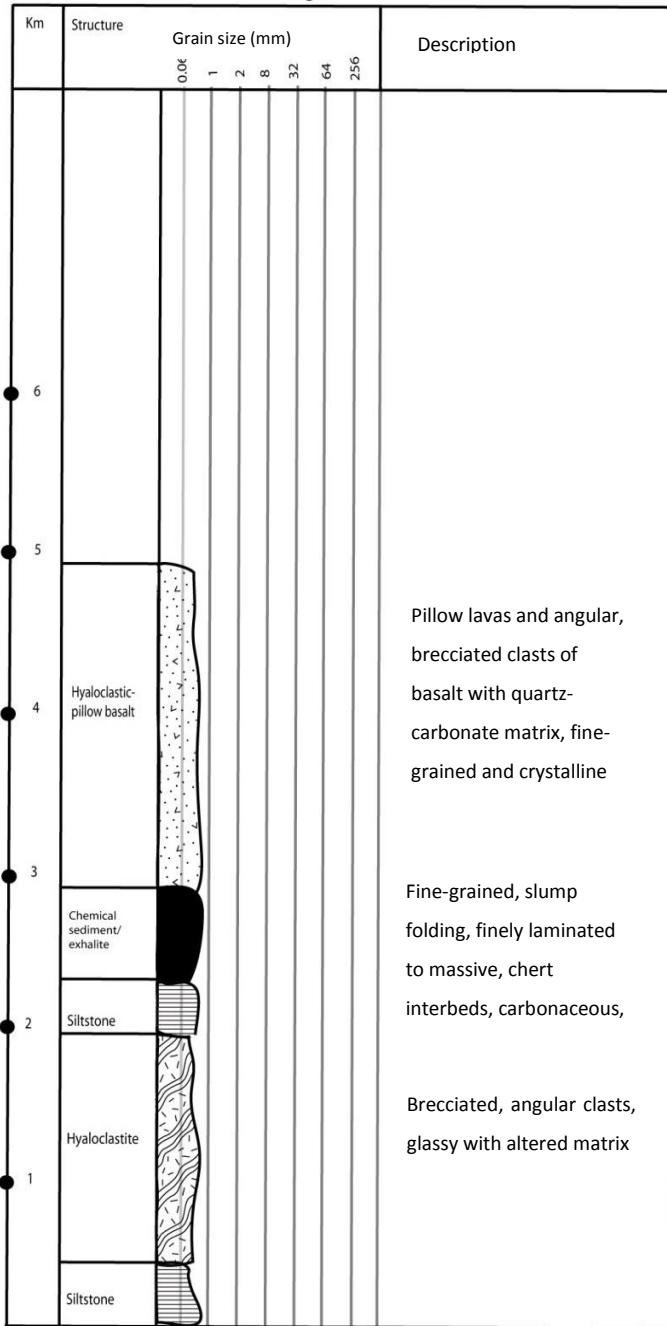
Log 4

**Figure B2.** Graphic logs of traverse lines as represented on the facies map. Log 1-7

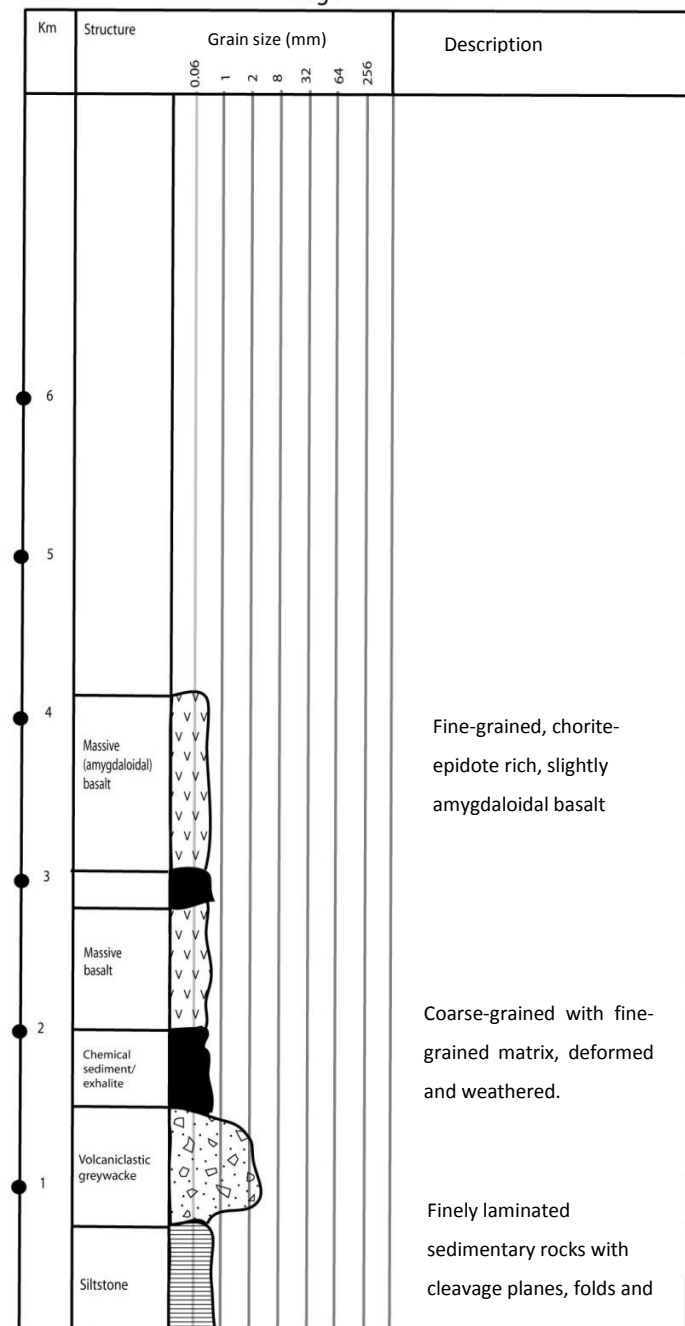
Log 5



Log 6



Log 7



Appendix C

Major and trace geochemical data of the mafic volcanic rocks and exhalite units from the southern Goren belt, the mafic to intermediate volcanic rocks of the Boromo and Houndé belts, the mafic rocks from the Tiebélé dome

ICP-MS geochemical data for the southern Goren belt basalts in ppm (Li-Rb)

Sample number	Lithology	Li	P	Sc	Ti	V	Cr	Co	Ni	Cu	Zn	Ga	As	Rb
KH/LP-009	Basalt	4.59	913.09	51.27	12507.75	326.79	34.47	37.56	41.75	93.40	125.95	11.73	0.42	7.67
KH/LP-012	Basalt	11.07	523.66	51.65	7059.20	396.11	26.08	36.67	51.02	137.04	74.86	12.24	0.56	4.02
KH/LP-018	Basalt	12.71	567.20	52.25	7789.84	367.90	32.37	42.34	51.61	103.84	101.70	18.34	0.97	1.03
KH/LP-025	Basalt	7.40	891.26	48.04	12991.37	391.66	31.26	79.65	62.15	92.65	137.58	13.74	0.51	10.71
KH/LP/02-003	Basalt	4.57	408.66	45.59	6090.40	348.82	56.55	34.34	72.28	115.19	72.21	11.47	0.44	2.55
KH/LP/02-007	Basalt	7.90	618.20	37.92	7017.39	282.20	23.88	35.50	70.00	95.48	81.01	18.47	0.47	4.59
KH/LP/02-011	Basalt	6.77	770.11	49.12	10346.72	368.22	42.43	48.98	76.42	159.03	126.19	18.57	0.52	2.33
KH/LP/02-021	Basalt	1.61	479.46	40.79	5475.51	307.73	23.91	36.07	52.12	106.66	74.22	16.98	0.47	0.75
KH/LP/02-026	Basalt	9.67	463.47	52.64	7045.91	246.64	31.40	45.61	69.66	60.25	93.44	16.06	0.54	7.09
KH/LP/02-030	Basalt	10.60	266.57	52.06	4468.56	288.00	187.75	38.92	118.42	91.81	55.61	11.00	0.41	1.65
KH/LP/02-047	Basalt	10.86	291.47	48.99	4942.36	276.42	253.16	48.88	131.67	125.98	74.10	13.60	0.40	1.23
KH/LP/02-053	Basalt	12.70	498.36	40.24	8100.10	328.37	66.98	58.55	98.53	179.49	99.61	17.23	0.39	0.98
KH/LP/02-057	Basalt	19.42	441.38	51.29	7282.10	299.47	7.43	49.96	49.25	164.92	103.01	17.21	0.88	4.34
KH/LP/02-062	Basalt	12.47	361.29	42.71	5690.03	308.63	197.59	48.79	132.84	156.61	82.64	15.52	0.43	5.99
KH/LP/02-095	Basalt	16.31	748.66	50.08	9590.04	415.84	27.46	45.78	58.85	159.31	119.55	21.45	0.51	3.44
KH/LP/02-096	Basalt	19.74	450.42	41.30	6415.13	298.55	15.90	49.24	57.11	134.58	81.09	16.58	0.41	6.00
KH/LP/02-097	Basalt	15.96	528.52	36.92	7483.04	300.70	21.04	45.38	70.71	142.42	91.16	18.64	0.58	16.75
KH/LP/02-098	Basalt	9.68	440.07	42.34	6727.00	317.87	32.51	51.24	66.34	156.70	95.77	17.18	0.56	3.58
KH/LP/02-099	Basalt	11.56	727.99	46.83	7017.58	305.71	20.98	46.13	44.85	173.07	93.50	16.27	0.58	4.02
KH/LP/02-108	Basalt Pyroclastic breccia	13.34	553.81	49.39	8865.51	395.56	111.15	57.64	97.22	171.06	119.88	18.57	0.55	1.77
KH/LP/02-126		24.10	1057.84	22.13	4806.93	167.63	529.62	44.15	338.07	39.74	92.84	16.84	0.43	26.70

ICP-MS geochemical data for the southern Goren belt basalts in ppm (Sr-Eu)

Sample number	Lithology	Sr	Y	Zr	Nb	Ba	Sn	Cs	La	Ce	Pr	Nd	Sm	Eu
KH/LP-009	Basalt	76.54	47.83	130.61	8.10	125.12	1.43	0.06	10.30	23.43	3.70	18.01	5.21	1.59
KH/LP-012	Basalt	79.91	33.73	70.35	3.66	41.18	0.80	0.29	5.02	12.72	2.06	10.45	3.23	1.14
KH/LP-018	Basalt	169.34	41.59	84.35	3.55	85.57	1.01	0.04	5.75	12.59	2.27	11.40	3.56	1.17
KH/LP-025	Basalt	112.82	45.03	136.79	8.36	174.56	1.17	0.07	9.03	21.73	3.42	16.71	5.08	1.70
KH/LP/02-003	Basalt	157.44	37.75	67.38	3.55	19.16	0.79	0.04	6.35	13.04	2.53	12.09	3.57	1.23
KH/LP/02-007	Basalt	215.17	31.87	91.20	4.32	55.08	1.13	0.10	8.06	18.95	2.96	13.59	3.73	1.25
KH/LP/02-011	Basalt	119.70	50.92	130.13	7.57	49.79	1.37	0.06	11.46	25.54	4.16	19.27	5.51	1.78
KH/LP/02-021	Basalt	76.35	28.70	46.11	2.49	12.28	1.02	0.01	4.33	11.75	1.73	8.74	2.70	0.92
KH/LP/02-026	Basalt	174.72	33.08	81.48	3.79	118.50	0.78	0.19	6.84	16.16	2.55	12.47	3.67	1.25
KH/LP/02-030	Basalt	80.85	22.24	45.51	2.18	14.75	0.63	0.23	3.07	8.69	1.26	6.31	2.03	0.85
KH/LP/02-047	Basalt	100.25	21.83	40.79	2.15	16.34	0.55	0.07	2.88	9.54	1.29	6.55	2.15	0.78
KH/LP/02-053	Basalt	93.81	27.06	82.54	3.98	42.46	0.97	0.07	5.37	15.09	2.32	11.75	3.62	1.17
KH/LP/02-057	Basalt	147.77	31.07	78.38	3.23	50.46	1.02	0.18	5.50	14.85	2.22	10.74	3.38	1.26
KH/LP/02-062	Basalt	178.24	23.81	53.09	2.60	39.38	0.71	0.21	3.34	10.59	1.43	7.19	2.31	0.85
KH/LP/02-095	Basalt	173.16	39.67	107.25	4.36	99.97	1.12	0.14	6.17	17.30	2.64	13.24	4.17	1.53
KH/LP/02-096	Basalt	123.34	26.17	76.33	3.47	33.03	0.86	0.06	5.32	14.55	2.05	9.78	2.87	1.02
KH/LP/02-097	Basalt	159.17	31.95	105.61	5.00	75.87	1.13	0.35	8.99	20.60	3.14	14.81	4.15	1.44
KH/LP/02-098	Basalt	83.23	32.02	77.60	4.37	30.84	0.93	0.12	5.23	13.51	2.20	10.80	3.32	1.17
KH/LP/02-099	Basalt	113.36	34.58	83.22	3.62	70.07	0.92	0.05	7.29	17.83	2.77	13.72	3.99	1.37
KH/LP/02-108	Basalt	125.98	39.02	91.13	5.12	35.04	1.04	0.08	6.84	16.05	2.47	12.39	3.78	1.31
KH/LP/02-126	Pyroclastic breccia	443.19	20.94	101.43	4.99	197.05	1.17	0.75	11.56	25.64	3.54	15.31	3.51	1.07

ICP-MS geochemical data for the southern Goren belt basalts in ppm (Gd-U)

Sample number	Lithology	Gd	Tb	Dy	Ho	Er	Tm	Yb	Lu	Hf	Ta	W	Pb	Th	U
KH/LP-009	Basalt	6.22	1.15	7.43	1.57	4.32	0.68	4.18	0.62	3.54	0.52	0.22	0.89	0.81	0.20
KH/LP-012	Basalt	3.90	0.75	5.09	1.10	3.12	0.50	3.21	0.49	1.91	0.22	0.08	1.13	0.44	0.12
KH/LP-018	Basalt	4.45	0.87	6.11	1.40	4.26	0.68	4.88	0.77	5.26	0.22	0.28	0.92	0.35	0.21
KH/LP-025	Basalt	6.05	1.11	7.30	1.57	4.36	0.62	4.12	0.61	3.71	0.53	0.22	1.30	0.81	0.19
KH/LP-02-003	Basalt	4.44	0.84	5.64	1.24	3.47	0.56	3.64	0.54	1.76	0.22	0.10	0.59	0.51	0.11
KH/LP-02-007	Basalt	4.40	0.78	5.01	1.06	2.95	0.46	2.94	0.44	2.34	0.27	0.44	1.33	0.58	0.20
KH/LP-02-011	Basalt	6.68	1.22	7.96	1.74	4.84	0.76	4.89	0.74	3.50	0.49	0.22	1.14	0.99	0.22
KH/LP-02-021	Basalt	3.44	0.64	4.31	0.93	2.66	0.42	2.73	0.41	1.27	0.15	0.14	0.76	0.27	0.06
KH/LP-02-026	Basalt	4.41	0.81	5.26	1.13	3.14	0.49	3.09	0.45	2.19	0.24	0.47	0.98	0.49	0.16
KH/LP-02-030	Basalt	2.59	0.48	3.30	0.73	2.05	0.33	2.09	0.33	1.27	0.14	0.16	0.49	0.19	0.08
KH/LP-02-047	Basalt	2.76	0.52	3.43	0.76	2.12	0.33	2.19	0.32	1.17	0.14	0.26	0.51	0.20	0.06
KH/LP-02-053	Basalt	4.29	0.74	4.65	0.95	2.51	0.37	2.32	0.34	2.20	0.25	0.21	0.80	0.35	0.10
KH/LP-02-057	Basalt	4.14	0.77	5.12	1.11	3.04	0.48	3.11	0.47	2.22	0.22	0.30	1.12	0.38	0.12
KH/LP-02-062	Basalt	2.94	0.55	3.73	0.82	2.28	0.36	2.33	0.35	1.48	0.17	0.06	0.67	0.22	0.07
KH/LP-02-095	Basalt	5.14	0.97	6.42	1.41	3.91	0.61	3.96	0.61	2.91	0.28	0.12	1.12	0.42	0.87
KH/LP-02-096	Basalt	3.54	0.64	4.16	0.90	2.44	0.38	2.47	0.38	2.04	0.22	0.58	0.88	0.37	0.13
KH/LP-02-097	Basalt	4.78	0.85	5.38	1.12	3.12	0.47	3.00	0.45	2.78	0.33	0.82	1.36	0.63	0.21
KH/LP-02-098	Basalt	4.08	0.77	5.15	1.11	3.15	0.47	3.15	0.48	2.16	0.27	0.13	0.64	0.35	0.10
KH/LP-02-099	Basalt	4.85	0.87	5.66	1.20	3.38	0.49	3.28	0.51	2.30	0.23	0.64	0.71	0.36	0.11
KH/LP-02-108	Basalt Pyroclastic breccia	4.70	0.90	6.05	1.32	3.71	0.56	3.73	0.57	2.47	0.33	0.52	0.86	0.42	0.11
KH/LP-02-126	Pyroclastic breccia	3.60	0.57	3.49	0.71	2.01	0.31	2.04	0.30	2.65	0.30	0.28	3.25	1.03	0.41

ICP-MS geochemical data for the southern Goren belt exhalite units in ppm (Li-Rb)

Sample number	Lithology	Li	P	Sc	Ti	V	Cr	Co	Ni	Cu	Zn	Ga	As	Rb
KH/LP/004	Exhalite	11.37	59.42	5.31	773.04	39.05	21.54	19.07	139.05	81.47	86.66	9.42	0.48	6.82
KH/LP/017	Exhalite	5.36	157.16	4.82	748.26	30.05	18.54	0.87	7.34	6.95	17.85	3.88	2.63	0.28
KH/LP/023	Exhalite	4.01	1143.67	16.87	2471.59	171.65	168.63	11.94	90.58	87.90	62.55	18.19	7.71	1.70
KH/LP/02-015	Exhalite	37.67	104.20	5.63	569.29	16.42	9.57	11.91	135.01	18.46	25.19	4.41	1.16	0.38
KH/LP/02-035	Exhalite	11.54	179.18	9.91	4613.00	241.73	197.24	4.20	46.80	70.03	30.74	19.88	9.62	49.94
KH/LP/02-080	Exhalite	27.73	358.72	8.06	1198.49	80.30	15.81	75.88	66.39	154.59	63.26	9.50	0.79	2.48

ICP-MS geochemical data for the southern Goren belt exhalite units in ppm (Sr-Eu)

Sample number	Lithology	Sr	Y	Zr	Nb	Ba	Sn	Cs	La	Ce	Pr	Nd	Sm	Eu
KH/LP/004	Exhalite	12.37	18.23	50.25	1.55	72.65	0.99	0.34	6.58	15.65	1.76	7.50	1.99	0.89
KH/LP/017	Exhalite	3.67	5.07	37.21	1.86	31.59	0.66	0.02	2.13	4.81	0.68	2.92	0.68	0.17
KH/LP/023	Exhalite	658.05	53.41	126.99	6.73	163.97	1.89	0.06	31.16	62.72	7.89	33.70	7.97	2.03
KH/LP/02-015	Exhalite	14.69	25.60	27.51	2.32	35.16	0.44	0.03	8.67	15.37	2.28	10.47	2.55	0.63
KH/LP/02-035	Exhalite	8.28	13.97	215.76	12.85	434.03	1.83	1.66	12.56	31.36	3.49	13.69	2.98	0.78
KH/LP/02-080	Exhalite	108.23	38.71	55.97	1.41	686.32	1.26	0.15	29.39	56.67	7.83	32.24	7.92	2.47

ICP-MS geochemical data for the southern Goren belt exhalite units in ppm (Sr-Eu)

Sample number	Lithology	Gd	Tb	Dy	Ho	Er	Tm	Yb	Lu	Hf	Ta	W	Pb	Th	U
KH/LP/004	Exhalite	2.51	0.41	2.54	0.52	1.50	0.23	1.51	0.23	1.29	0.09	0.11	3.27	1.63	0.91
KH/LP/017	Exhalite	0.67	0.11	0.81	0.17	0.54	0.09	0.69	0.11	0.85	0.14	0.18	1.60	0.80	0.34
KH/LP/023	Exhalite	10.37	1.64	10.05	2.01	5.24	0.79	4.86	0.69	2.79	0.35	9.26	10.21	1.54	2.47
KH/LP/02-015	Exhalite	3.08	0.52	3.35	0.73	2.05	0.30	1.89	0.27	0.66	0.08	71.01	5.27	0.53	0.51
KH/LP/02-035	Exhalite	2.83	0.37	2.15	0.46	1.29	0.20	1.41	0.21	5.04	0.79	2.53	3.35	1.53	4.04
KH/LP/02-080	Exhalite	9.01	1.44	8.66	1.76	4.74	0.71	4.65	0.67	1.52	0.14	1.33	5.87	0.68	0.81

Major element XRF geochemical data for the southern Goren belt basalts in wt% (SiO₂-CaO)

Sample number	Lithology	SiO ₂	Al ₂ O ₃	Fe ₂ O ₃	FeO	MnO	MgO	CaO
KH/LP/009	Basalt	59.86	10.65	1.57	12.75	0.13	3.31	4.45
KH/LP/012	Basalt	53.96	13.87	1.51	12.24	0.17	6.82	7.04
KH/LP/018	Basalt	55.48	12.82	1.63	13.18	0.16	5.91	8.22
KH/LP/025	Basalt	58.69	12.06	1.39	11.24	0.15	4.14	5.29
KH/LP/02-003	Basalt	50.94	13.23	1.66	13.46	0.21	6.25	10.73
KH/LP/02-007	Basalt	56.93	13.49	1.32	10.72	0.16	4.14	9.40
KH/LP/02-011	Basalt	50.99	12.83	1.80	14.57	0.21	5.28	9.22
KH/LP/02-021	Basalt	58.81	11.64	1.32	10.68	0.19	3.71	10.23
KH/LP/02-026	Basalt	53.47	14.71	1.45	11.77	0.18	5.37	8.19
KH/LP/02-030	Basalt	48.92	15.59	1.33	10.75	0.20	8.16	12.11
KH/LP/02-047	Basalt	51.80	14.85	1.26	10.24	0.22	6.95	11.34
KH/LP/02-053	Basalt	50.55	14.05	1.56	12.60	0.22	6.61	10.08
KH/LP/02-057	Basalt	54.15	14.60	1.49	12.08	0.19	5.01	7.93
KH/LP/02-062	Basalt	51.15	14.70	1.38	11.14	0.19	7.37	10.62
KH/LP/02-095	Basalt	52.76	14.58	1.82	14.71	0.25	5.66	6.05
KH/LP/02-096	Basalt	53.17	13.92	1.40	11.30	0.23	6.51	9.83
KH/LP/02-097	Basalt	54.89	13.55	1.41	11.45	0.16	6.03	8.20
KH/LP/02-098	Basalt	51.23	13.92	1.51	12.19	0.21	7.42	10.03
KH/LP/02-099	Basalt	53.47	14.26	1.55	12.53	0.20	6.00	7.50
KH/LP/02-108	Basalt	51.43	13.50	1.67	13.55	0.22	6.51	9.26
KH/LP/02-126	Pyroclastic breccia	56.48	13.30	0.97	7.87	0.13	9.17	6.96

Major element XRF geochemical data for the southern Goren belt basalts in wt% (Na₂O-LOI)

Sample number	Lithology	Na ₂ O	K ₂ O	TiO ₂	P ₂ O ₅	Cr ₂ O ₃	NiO	LOI	TOTAL
KH/LP/009	Basalt	4.25	0.45	2.05	0.21	0.01	0.01	1.27	99.71
KH/LP/012	Basalt	2.73	0.21	1.37	0.13	0.01	0.01	3.65	100.08
KH/LP/018	Basalt	1.11	0.06	1.32	0.14	0.01	0.01	3.41	100.04
KH/LP/025	Basalt	3.92	0.66	2.20	0.21	0.02	0.01	1.75	100.00
KH/LP/02-003	Basalt	1.82	0.17	1.48	0.14	0.02	0.01	2.28	100.13
KH/LP/02-007	Basalt	2.23	0.24	1.31	0.16	0.02	0.01	3.05	100.14
KH/LP/02-011	Basalt	3.08	0.20	1.79	0.19	0.02	0.01	1.92	100.21
KH/LP/02-021	Basalt	1.98	0.18	1.00	0.12	0.01	0.01	0.92	99.89
KH/LP/02-026	Basalt	2.99	0.37	1.25	0.12	0.01	0.01	2.25	99.91
KH/LP/02-030	Basalt	1.87	0.09	0.86	0.08	0.05	0.02	2.51	100.03
KH/LP/02-047	Basalt	2.17	0.09	0.91	0.07	0.05	0.02	2.88	99.99
KH/LP/02-053	Basalt	2.67	0.10	1.45	0.12	0.02	0.01	2.22	100.03
KH/LP/02-057	Basalt	2.69	0.23	1.32	0.11	0.01	0.01	2.31	99.82
KH/LP/02-062	Basalt	2.00	0.32	1.04	0.09	0.04	0.02	2.68	100.06
KH/LP/02-095	Basalt	2.18	0.20	1.76	0.18	0.02	0.01	3.77	100.17
KH/LP/02-096	Basalt	2.13	0.30	1.17	0.10	0.01	0.01	2.61	100.08
KH/LP/02-097	Basalt	2.07	0.59	1.40	0.14	0.01	0.01	2.65	99.92
KH/LP/02-098	Basalt	2.16	0.20	1.29	0.12	0.02	0.01	2.94	100.30
KH/LP/02-099	Basalt	2.57	0.26	1.33	0.19	0.01	0.01	2.72	99.87
KH/LP/02-108	Basalt Pyroclastic breccia	2.09	0.13	1.52	0.14	0.03	0.01	2.78	100.05
KH/LP/02-126		2.61	1.05	0.78	0.23	0.08	0.04	2.02	99.67

Major element XRF geochemical data for the southern Goren belt exhalite units in wt% (SiO₂-CaO)

Sample number	Lithology	SiO ₂	Al ₂ O ₃	Fe ₂ O ₃	FeO	MnO	MgO	CaO
KH/LP/004	Exhalite	79.99	6.85	0.22	1.77	8.44	0.2	0.84
KH/LP/017	Exhalite	93.69	2.3	0.38	3.05	0.01	0.04	0.11
KH/LP/023	Exhalite	75.77	9.84	0.56	4.55	6.77	0.32	0.49
KH/LP/02-015	Exhalite	93.42	3.66	0.23	1.87	0.15	0.03	0.07
KH/LP/02-035	Exhalite	73.62	14.95	0.69	5.59	0.02	0.54	0.09
KH/LP/02-080	Exhalite	76.29	10.29	0.45	3.66	7.5	0.05	0.12

Major element XRF geochemical data for the southern Goren belt exhalite units in wt% (Na₂O-LOI)

Sample number	Lithology	Na ₂ O	K ₂ O	TiO ₂	P ₂ O ₅	Cr ₂ O ₃	NiO	LOI	TOTAL
KH/LP/004	Exhalite	-0.03	0.21	0.15	0.03	0.00	0.02	1.75	98.68
KH/LP/017	Exhalite	-0.05	0.01	0.12	0.04	0.01	0.00	1.52	99.72
KH/LP/023	Exhalite	-0.05	0.17	0.43	0.26	0.03	0.01	7.14	99.15
KH/LP/02-015	Exhalite	-0.03	0.03	0.12	0.04	0.00	0.02	9.15	99.60
KH/LP/02-035	Exhalite	0.09	3.16	0.90	0.05	0.04	0.01	8.14	99.74
KH/LP/02-080	Exhalite	-0.03	0.27	0.17	0.09	0.00	0.01	6.51	98.87

Trace element XRF geochemical data for the southern Goren belt basalts in ppm (Sc-Rb)

Sample number	Lithology	Sc	V	Cr	Co	Ni	Cu	Zn	Ga	Rb
KH/LP/009	Basalt	39.74	321.19	26.33	31.72	29.83	84.82	123.64	9.22	7.39
KH/LP/012	Basalt	44.11	343.16	22.39	46.23	49.23	172.86	112.97	17.52	4.85
KH/LP/018	Basalt	43.54	351.73	29.67	39.41	42.33	99.29	113.98	19.3	1.71
KH/LP/025	Basalt	40.57	400.37	26.88	75.19	53.4	90.3	153.03	12.22	10.82
KH/LP/02-003	Basalt	44.31	369.53	99.83	53.13	99.42	166.36	132.18	17.41	4.18
KH/LP/02-007	Basalt	37.73	309.46	26.98	40.69	71.25	107.89	91.43	18.37	5.46
KH/LP/02-011	Basalt	44.15	393.26	38.32	46.97	73.33	163.83	146.57	18.67	2.56
KH/LP/02-021	Basalt	40.94	341.59	9.65	33.49	45.43	104.61	83.34	15.03	0.92
KH/LP/02-026	Basalt	47.63	247.35	29.56	40.42	69.94	63.42	104.71	14.85	9.2
KH/LP/02-030	Basalt	47.72	280.28	279.55	50.21	151.57	106.71	88.14	14.51	2.5
KH/LP/02-047	Basalt	46.95	287.66	255.48	44.29	141.99	135.66	91.25	13.31	1.43
KH/LP/02-053	Basalt	39.53	330.66	67.96	55.7	98.81	166.57	121.88	17.21	0.54
KH/LP/02-057	Basalt	46.65	318.68	8.79	45.38	46.8	179	117.72	17.03	3.56
KH/LP/02-062	Basalt	40.47	328.16	188.42	48.03	132.43	156.68	95.2	15	8.15
KH/LP/02-095	Basalt	39.08	414.95	28.93	36.77	48.59	149.72	146.66	20.38	5.06
KH/LP/02-096	Basalt	44.98	317.26	19.68	48.81	53.01	138.92	97.06	16.13	7.96
KH/LP/02-097	Basalt	35.59	313.96	20.84	47.63	74.76	138.88	102.93	18.64	19.7
KH/LP/02-098	Basalt	47.17	352.05	30.97	58.14	68.24	163.87	114.38	16.97	4.08
KH/LP/02-099	Basalt	46.15	360.87	25.18	44.96	39.97	194.22	112.67	17.05	4.81
KH/LP/02-108	Basalt Pyroclastic breccia	38.54	390.26	106.92	51.04	89.19	169.89	131.79	18.16	2.57
KH/LP/02-126	Pyroclastic breccia	23.903	175.133	481.934	42.549	319.224	36.953	96.434	17.926	28.383

Trace element XRF geochemical data for the southern Goren belt basalts in ppm (Sr-U)

Sample number	Lithology	Sr	Y	Zr	Nb	Mo	Ba	Pb	Th	U
KH/LP/009	Basalt	65.74	36.46	122.04	5.63	0.6	128.95	2.17	0.42	4.69
KH/LP/012	Basalt	82.01	28.93	82.67	1.25	0.67	52.31	0.41	1.81	5.48
KH/LP/018	Basalt	145.91	29.69	80.06	4.97	0.53	78.44	1.44	8.59	6.76
KH/LP/025	Basalt	97.92	34.99	130.2	10.18	1.09	174.42	1.29	4.49	6.28
KH/LP/02-003	Basalt	171.53	30.47	89.6	4.47	0.25	17	1.92	0.83	4.98
KH/LP/02-007	Basalt	220.21	27.09	94.72	3.85	0.34	57.96	1.87	0.07	4.62
KH/LP/02-011	Basalt	110.25	39.6	131.88	4.88	0.73	43.86	2.77	0.09	6
KH/LP/02-021	Basalt	70.92	21.64	58.02	4.04	0.16	9.66	2.05	8.55	5.41
KH/LP/02-026	Basalt	164.06	24.74	82.49	6.77	1.09	115.77	0.59	5.32	6.1
KH/LP/02-030	Basalt	81.58	17.46	43.46	1.59	0.06	20.14	2.02	7.7	3.31
KH/LP/02-047	Basalt	98.11	17.37	48.59	2.84	1.84	14.22	1.41	3.92	2.39
KH/LP/02-053	Basalt	94.83	20.96	83.11	3.95	0.58	38.99	0.36	5.71	3.56
KH/LP/02-057	Basalt	141.65	23.75	78.53	3.84	1.13	48.29	1.18	3.23	3.92
KH/LP/02-062	Basalt	185.47	22.07	59.16	3.5	0.16	40.74	1.51	5.88	7.52
KH/LP/02-095	Basalt	153.68	31.46	105.43	4.58	0.06	98.79	2.02	8.07	8.54
KH/LP/02-096	Basalt	122.88	21.02	75.4	3.94	0.3	33.58	0.85	7.6	7.18
KH/LP/02-097	Basalt	139.11	24.46	102.87	5.14	0.04	82.12	0.66	5.88	9.26
KH/LP/02-098	Basalt	83.72	28.72	76.13	4.11	0.05	35.35	1.01	4.19	2.78
KH/LP/02-099	Basalt	102.08	27.94	82.03	3.74	0.12	69.38	0.13	1.66	1.58
KH/LP/02-108	Basalt	114.33	31.82	87.79	4.63	0.69	39.54	1.61	2.39	1.63
KH/LP/02-126	Pyroclastic breccia	448.812	21.798	101.187	2.164	0.095	184.659	3.937	2.902	0.303

Trace element XRF geochemical data for the southern Goren belt exhalite units in ppm (Sc-Rb)

Sample number	Lithology	Sc	V	Cr	Co	Ni	Cu	Zn	Ga	Rb
KH/LP/004	Exhalite	5.06	87.23	14.01	21.19	127.55	72.24	91.07	4.58	7.67
KH/LP/017	Exhalite	2.87	26.46	22.86	4.2	1.92	4.65	2.86	4.62	0.17
KH/LP/023	Exhalite	17.27	221.21	181.99	5.15	73.81	69.85	50.86	11.58	2.82
KH/LP/02-015	Exhalite	2.46	15.2	2.43	14.4	112.53	2.83	21.73	4.18	0.48
KH/LP/02-035	Exhalite	20.45	253.69	181.62	2.18	38.74	62.53	24.56	18.59	78.6
KH/LP/02-080	Exhalite	14.58	126.35	20	106.72	58.37	151.1	82.62	5.42	3.32

Trace element XRF geochemical data for the southern Goren belt exhalite units in ppm (Sr-U)

Sample number	Lithology	Sr	Y	Zr	Nb	Mo	Ba	Pb	Th	U
KH/LP/004	Exhalite	11.23	13.99	49.26	1.62	0.86	115.54	3.92	1.63	4.17
KH/LP/017	Exhalite	3.55	4.5	35.48	1.01	0.44	25.77	1.38	0.79	1.81
KH/LP/023	Exhalite	583.38	40.93	126.64	7.73	14.13	197.85	10.55	2.21	1.01
KH/LP/02-015	Exhalite	13.31	19.42	27.08	1.25	1.58	34.79	3.45	0.69	1.84
KH/LP/02-035	Exhalite	16.74	45.83	210.1	11.69	1.51	666.02	4.8	3.42	4.82
KH/LP/02-080	Exhalite	116.34	42.03	54.4	1.14	0.93	1155.96	4.55	5.95	5.33

Geochemical Data from the Boromo and Houndé belts

Major element ICP-AES analysis of the volcanic rocks

Sample number	Lithology	SiO ₂	Al ₂ O ₃	Fe ₂ O ₃	MnO	MgO	CaO	Na ₂ O	K ₂ O	TiO ₂	P ₂ O ₅	LOI	Total
HO14-Houndé	Tholeiitic basalt	51.9	13.15	13.35	0.19	6.88	10.4	2.1	0.12	0.99	0.07	0.89	21.64
HO23-Houndé	Tholeiitic basalt	48.5	13.45	16.85	0.28	4.94	10.75	2.63	0.21	2	0.19	0.3	21.3
HO33-Houndé	Tholeiitic basalt	49	15.1	11.9	0.16	6.85	11.1	2.11	0.14	0.77	0.06	3.51	24.7
HO118-Houndé	Tholeiitic basalt	49.4	14.25	11.8	0.18	7.57	11.55	1.86	0.39	1.01	0.11	2.17	24.84
HO52-Boromo	Tholeiitic basalt	51.8	13.55	12.75	0.2	6.01	11.45	1.68	0.11	0.74	0.01	0.99	21.19
H0592-Boromo	Tholeiitic basalt	52.4	12.2	16.75	0.24	5.04	8.83	1.85	0.12	1.32	0.12	0.1	17.62
HO521-Boromo	Tholeiitic basalt	47.64	13.13	12.79	0.19	7.08	11.41	1.89	0.14	0.83	0.04	1.75	23.33
HO12-Houndé	Calc-Alkaline basalt	59.3	14.45	8.11	0.1	4.61	5.46	3.04	1.13	0.71	0.15	2.65	17.85
HO71-Houndé	Calc-Alkaline basalt	58.2	14.85	7.36	0.11	3.92	6.52	2.86	1.9	0.69	0.17	3.74	19.91
HO345-Houndé	Calc-Alkaline basalt	50.7	13	12.15	0.19	7.5	8.09	2.77	1.82	1.08	0.28	2.27	24
HO3-Houndé	Calc-Alkaline basalt	54.2	13.7	10.2	0.16	5.15	7.88	1.51	3.18	0.96	0.38	2.56	21.78
HO9-Houndé	Calc-Alkaline basalt	62.1	14.8	8.33	0.08	2.21	4.56	3.47	2.11	1.16	0.36	0.77	14.72
H0294-Boromo	Calc-Alkaline basalt	59	14.55	7.4	0.12	3.68	5.31	4.09	0.31	0.52	0.12	3.39	17.54

Trace element ICP-AES geochemical data in ppm (Rb-Zr)

Sample number	Lithology	Rb	Ba	Sr	U	Th	Ta	Nb	Hf	Zr
HO14-Houndé	Tholeiitic basalt	2.50	15.30	108.00	0.06	0.19	0.20	2.10	1.60	55.00
HO23-Houndé	Tholeiitic basalt	4.20	47.00	223.00	0.25	0.53	0.10	4.50	3.70	138.00
HO33-Houndé	Tholeiitic basalt	2.50	63.30	92.20	0.13	0.34		1.90	1.50	49.00
HO118-Houndé	Tholeiitic basalt	5.70	81.20	220.00	0.07	0.21		2.30	1.30	40.00
HO52-Boromo	Tholeiitic basalt	0.60	25.40	94.20	0.08	0.18		1.80	1.90	67.00
H0592-Boromo	Tholeiitic basalt	2.10	205.00	98.60	0.13	0.41	0.20	2.10	2.30	82.00
HO521-Boromo	Tholeiitic basalt	2.31	31.29	85.51	0.06	0.20	0.57	2.01	1.02	31.47
HO12-Houndé	Calc-Alkaline basalt	36.5	338	449	0.75	2.48	0.5	5.6	3.2	120
HO71-Houndé	Calc-Alkaline basalt	40.8	1045	500	0.93	2.96	0.3	5.9	3.1	121
HO345-Houndé	Calc-Alkaline basalt	52.7	577	354	0.59	1.86	0.2	5.1	2.8	100
HO3-Houndé	Calc-Alkaline basalt	125.5	1830	743	2.24	6.73	0.6	9.1	3.3	125
HO9-Houndé	Calc-Alkaline basalt	83.2	367	147.5	1.34	4.9	0.9	11.2	4.9	188
H0294-Boromo	Calc-Alkaline basalt	4.8	168.5	125	0.54	1.23	0.3	3.6	2.4	89

Trace element ICP-AES geochemical data in ppm (Sm-Lu)

Sample number	Lithology	Sm	Eu	Gd	Tb	Dy	Ho	Er	Tm	Yb	Lu
HO14-Houndé	Tholeiitic basalt	2.12	0.87	2.89	0.55	3.83	0.84	2.46	0.40	2.35	0.38
HO23-Houndé	Tholeiitic basalt	4.05	1.50	4.75	0.86	5.72	1.18	3.58	0.53	3.54	0.51
HO33-Houndé	Tholeiitic basalt	1.82	0.68	2.38	0.40	3.03	0.61	2.00	0.31	1.92	0.30
HO118-Houndé	Tholeiitic basalt	2.06	0.84	2.52	0.42	3.00	0.60	1.78	0.27	1.66	0.27
HO52-Boromo	Tholeiitic basalt	1.69	0.69	2.41	0.43	3.10	0.67	2.06	0.30	2.00	0.34
H0592-Boromo	Tholeiitic basalt	3.04	1.17	4.00	0.87	5.77	1.20	3.78	0.40	3.59	0.57
HO521-Boromo	Tholeiitic basalt	1.91	0.73	2.79	0.48	3.41	0.74	2.26	0.33	2.22	0.34
HO12-Houndé	Calc-Alkaline basalt	2.93	0.97	3.07	0.45	2.78	0.54	1.61	0.24	1.53	0.24
HO71-Houndé	Calc-Alkaline basalt	3.47	1.04	3.44	0.49	3.02	0.59	1.79	0.26	1.76	0.25
HO345-Houndé	Calc-Alkaline basalt	3.9	1.29	4.35	0.7	4.27	0.85	2.64	0.34	2.57	0.36
HO3-Houndé	Calc-Alkaline basalt	6.62	1.65	6.55	0.96	5.23	1.04	3	0.43	2.71	0.41
HO9-Houndé	Calc-Alkaline basalt	5.3	1.31	5.81	0.91	5.48	1.18	3.47	0.54	3.45	0.51
H0294-Boromo	Calc-Alkaline basalt	2.25	0.72	2.26	0.35	2.01	0.41	1.24	0.15	1.15	0.18

Trace element ICP-AES geochemical data in ppm (Y-Nd)

Sample number	Lithology	Y	Ni	Cr	Co	V	La	Ce	Pr	Nd
HO14-Houndé	Tholeiitic basalt	21.70	119.00	170.00	86.60	296.00	3.00	7.40	1.25	6.50
HO23-Houndé	Tholeiitic basalt	30.60	47.00	50.00	63.60	395.00	6.20	16.00	2.60	12.70
HO33-Houndé	Tholeiitic basalt	16.30	66.00	90.00	65.70	257.00	2.80	8.90	1.31	6.40
HO118-Houndé	Tholeiitic basalt	15.40	98.00	300.00	68.10	249.00	2.80	8.70	1.31	6.70
HO52-Boromo	Tholeiitic basalt	16.70	95.00	110.00	113.50	266.00	2.70	6.20	0.98	5.10
HO592-Boromo	Tholeiitic basalt	32.20	47.00	30.00	52.90	334.00	3.70	9.80	1.55	8.30
HO521-Boromo	Tholeiitic basalt	18.74	97.68	327.58	87.83		2.46	6.75	1.08	5.66
HO12-Houndé	Calc-Alkaline basalt	14.9	114	240	63.7	150	13.7	27.6	3.46	13.6
HO71-Houndé	Calc-Alkaline basalt	15.5	59	150	68.5	138	14.9	30	3.85	15
HO345-Houndé	Calc-Alkaline basalt	21.5	63	270	64.9	254	11.3	24.3	3.4	15
HO3-Houndé	Calc-Alkaline basalt	29.3	57	220	53.5	199	25.7	53.8	7.3	30.3
HO9-Houndé	Calc-Alkaline basalt	32.3			54.6	110	25.1	51.7	6.44	24.8
HO294-Boromo	Calc-Alkaline basalt	10.9	41	110	24.1	141	9.2	19.4	2.43	10

Geochemical analysis of the Tiebélé region

Major element analysis in wt%

Sample number	Lithology	SiO ₂	Al ₂ O ₃	Fe ₂ O ₃	MnO	MgO	CaO	Na ₂ O	K ₂ O	TiO ₂	P ₂ O ₅	Cr ₂ O ₃	Ba	Ni	Sc	LOI	TOTAL
N2	Basalt	51.43	14.43	11.82	0.17	6.16	7.25	2.52	0.34	1.49	0.18	0.03	147.00	155.00	25.00	4.00	99.82
N4	Basalt	49.16	12.24	12.36	0.17	5.11	7.69	2.48	0.16	1.79	0.25	0.01	102.00	49.00	28.00	8.30	99.75
N6	Basalt	50.43	13.41	11.82	0.16	5.62	8.04	4.43	0.43	1.43	0.25	0.02	104.00	79.00	33.00	3.80	99.83
N10	Basalt	51.91	12.78	14.43	0.17	5.21	6.39	3.48	0.55	1.84	0.20	0.01	198.00	63.00	35.00	2.80	99.80
A1	Basalt	47.10	11.97	11.65	1.10	7.78	7.10	1.31	0.12	1.12	0.20	0.01	53.00	27.00	36.00	10.30	99.77
A5	Basalt	45.57	18.29	11.13	0.34	5.51	7.54	3.93	0.80	1.04	0.17	0.04	324.00	177.00	30.00	5.50	99.93
G4	Basalt	47.56	17.74	14.80	0.29	0.88	7.70	1.70	1.69	3.44	1.50				2.50	100.35	
HT50	Basalt	47.69	16.98	15.15	0.25	0.75	8.29	1.50	2.27	1.34	1.69				3.50	99.55	
HTBA	Basalt	54.45	17.23	17.23	0.04	4.60	4.21	8.66	1.20	5.22	0.02				4.00	100.00	
HTGOGO	Basalt	53.90	16.41	4.91	0.11	6.34	9.27	1.00	4.58	0.46	0.14				2.50	99.86	
HTPILL	Basalt	47.19	17.79	15.15	0.31	1.40	7.00	3.00	3.49	1.44	0.21				2.80	100.08	

Trace element data in ppm (Co-Ta)

Sample number	Lithology	Co	Cs	Ga	Hf	Nb	Rb	Sn	Sr	Ta
N2	Basalt	40.20	0.50	18.70	2.90	4.80	7.90	1.00	359.90	0.40
N4	Basalt	38.20	0.20	17.10	2.60	4.70	3.70	1.00	212.90	0.40
N6	Basalt	34.10	0.10	15.80	2.10	4.00	5.20	0.90	165.90	0.40
N10	Basalt	36.20	0.20	15.10	2.30	3.60	8.80	1.00	173.40	0.30
A1	Basalt	41.90	0.40	17.00	2.50	4.10	3.50	1.00	108.70	0.30
A5	Basalt	47.70	0.80	16.20	1.00	1.80	22.20	1.00	299.70	0.10

Trace element data in ppm (Th-Cd)

Sample number	Lithology	Th	Tl	U	V	W	Zr	Y	La	Ce	Cd
N2	Basalt	1.40	0.09	0.50	246.00	4.00	107.00	23.30	10.70	25.00	0.20
N4	Basalt	0.60	0.20	0.20	280.00	1.00	97.30	26.60	8.20	20.80	0.20
N6	Basalt	0.60	0.09	0.20	258.00	2.00	83.20	22.60	8.50	21.70	0.50
N10	Basalt	0.60	0.09	0.30	327.00	0.90	81.40	27.20	8.00	20.50	0.30
A1	Basalt	1.00	0.09	0.40	250.00	2.00	89.30	26.20	8.20	20.70	0.20
A5	Basalt	0.50	0.10	0.30	228.00	2.00	38.10	14.00	4.70	12.20	0.20

Trace element data in ppm (Pr-Sb)

Sample number	Lithology	Pr	Nd	Sm	Eu	Gd	Tb	Dy	Ho	Er	Sb
N2	Basalt	3.32	15.40	3.90	1.34	3.93	0.62	4.43	0.91	2.74	1.00
N4	Basalt	3.00	15.00	3.80	1.61	4.55	0.74	5.09	1.06	3.04	1.00
N6	Basalt	2.82	14.10	3.50	1.28	3.74	0.61	4.28	0.93	2.65	2.00
N10	Basalt	2.77	13.40	3.60	1.35	4.28	0.73	4.91	1.07	3.16	0.90
A1	Basalt	2.72	13.50	3.50	1.13	3.89	0.65	4.56	0.99	3.14	1.00
A5	Basalt	1.61	8.00	1.90	0.73	2.12	0.36	2.43	0.52	1.58	2.00

Trace element data in ppm (Tm-Bi)

Sample number	Lithology	Tm	Yb	Lu	Mo	Cu	Pb	Zn	Ni	As	Bi
N2	Basalt	0.35	2.56	0.38	3.30	70.00	3.00	112.00	132.00	2.00	0.90
N4	Basalt	0.41	2.79	0.39	1.70	68.00	2.00	121.00	64.00	1.00	1.00
N6	Basalt	0.35	2.45	0.38	2.40	81.00	5.00	192.00	52.00	1.00	0.90
N10	Basalt	0.42	2.99	0.43	1.80	77.00	2.00	125.00	51.00	1.00	1.00
A1	Basalt	0.42	3.04	0.45	0.70	20.00	4.00	178.00	25.00	1.00	0.90
A5	Basalt	0.22	1.55	0.23	0.60	96.00	2.00	86.00	172.00	1.00	0.90

Calculation for phosphorus retention in garnet-clinopyroxene in the magma source region:

1 rock = 0.15 Liquid + 0.85 Residue

0.85 Residue = 0.1 garnet and clinopyroxene + 0.75 olivine and orthopyroxene

$$1 \times 0.02 = (0.05 \times 0.15) + [(0.1x) + (0.75 \times 0)]$$

$$0.02 = 0.0075 + 0.1x$$

Where x is the concentration of P in garnet and clinopyroxene.

$$0.0125 = 0.1x$$

$$0.125 = x$$

Therefore, $x = 0.125 \text{ P}_2\text{O}_5 \text{ wt\%}$

Atomic weight of oxygen = 16

Atomic weight of phosphorus = 31

Therefore the atomic weight of $\text{P}_2\text{O}_5 = 142$

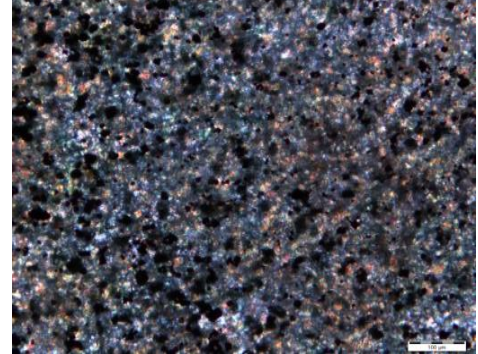
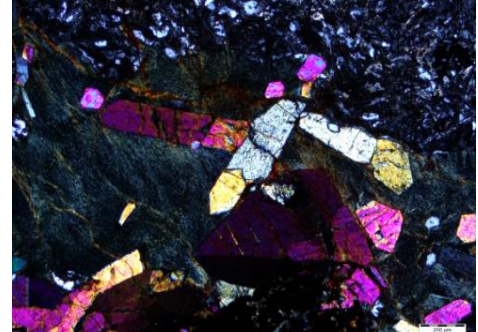
P: $\text{P}_2\text{O}_5 = 31:142 = 1:4.58$

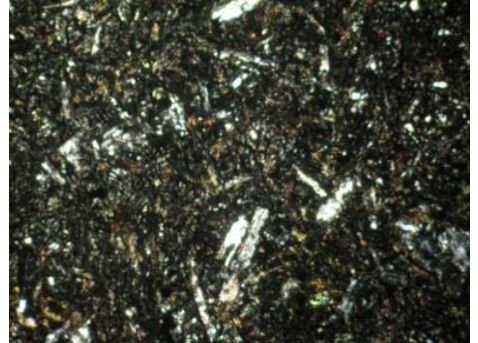
Therefore, in weight percent

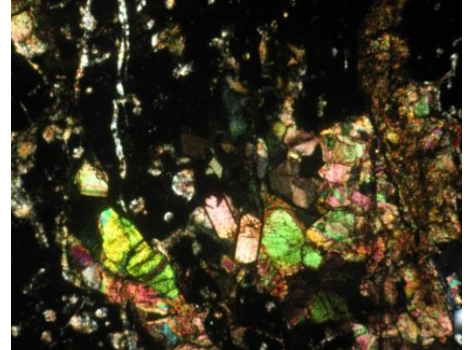
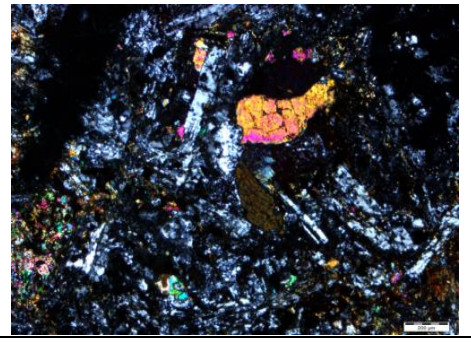
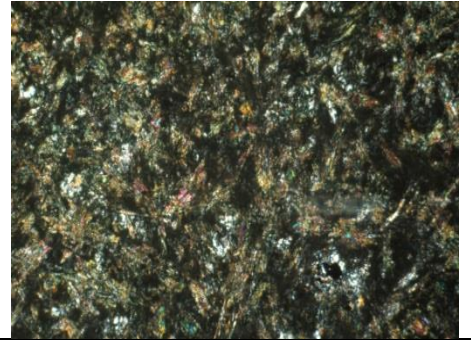
$$\text{P} = \frac{0.125}{4.58} = 0.0273 \text{ wt\%}$$

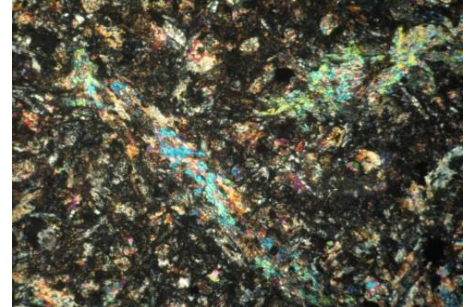
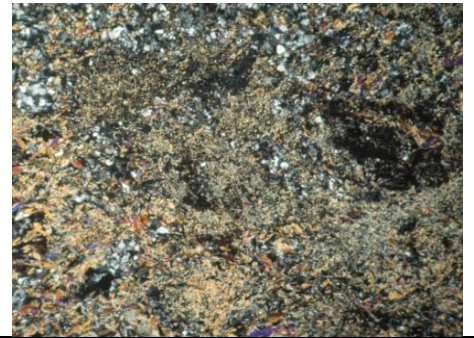
$0.0273 \times 10\,000 = 273 \text{ ppm}$ of phosphorus is concentrated in clinopyroxene and garnet.

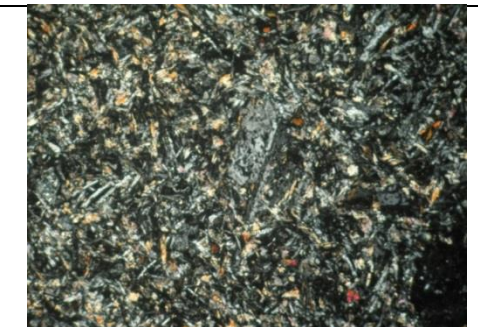
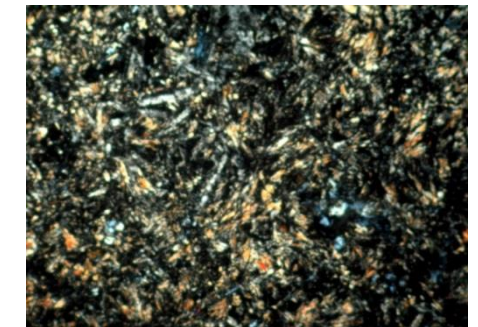
Appendix D
Petrographic description

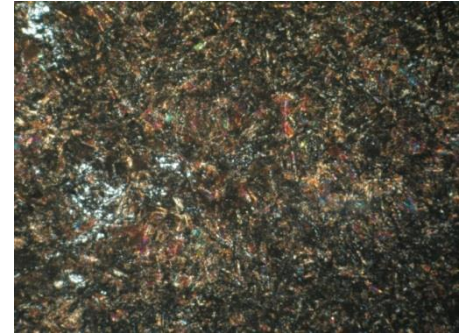
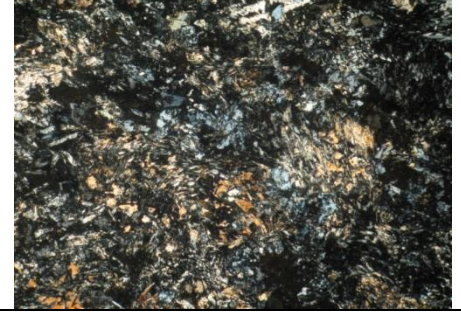
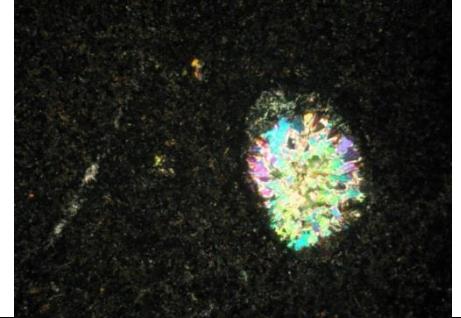
Sample number	Location (UTM)			Petrographic description	Photomicrograph
Basalts					
G12-001	30P	703502	1446724	Fine-grained basalt; epidote-chlorite-actinolite rich. Euhedral ilmenite and magnetite (40 %). Sample is deformed and shows no primary mineralogy. Secondary quartz and minor hornblende present.	
G12-003	30P	702832	1446448	Fine-grained basalt; epidote and chlorite rich as well as a higher quartz content (secondary). Also deformed.	

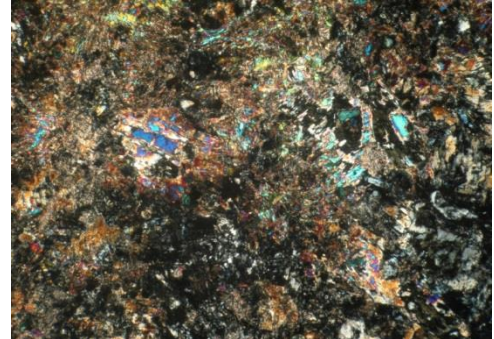
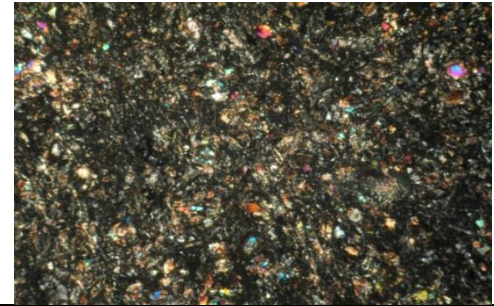
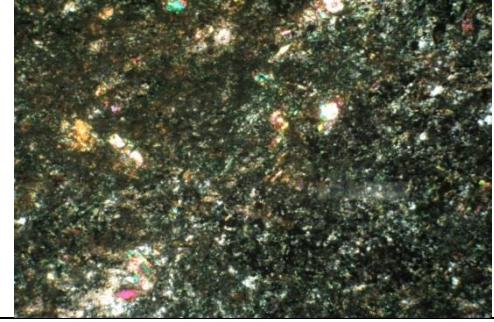
G12-009					
	30P	693302	1444147	Amygdaloidal, fine-grained basalt with 20 % plagioclase (> 0.5 mm), 7- 10 % clinopyroxene. Amygdales contain epidote and zeolite group minerals. Chloritised glass also present.	
G12-011					
	30P	693247	1444459	Amygdaloidal, hyaloclastic, fine-grained basalt with chlorite and epidote dominating the groundmass, 2-5 % plagioclase crystals (0.2 mm) (Scale = 11mm)	
G12-012					
	30P	678993	1467130	Fine-grained, plagioclase-phyric (10%) basalt, clinopyroxene (5 %) with chlorite-epidote groundmass and minor secondary quartz.	

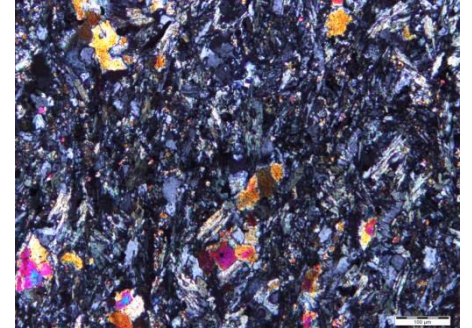
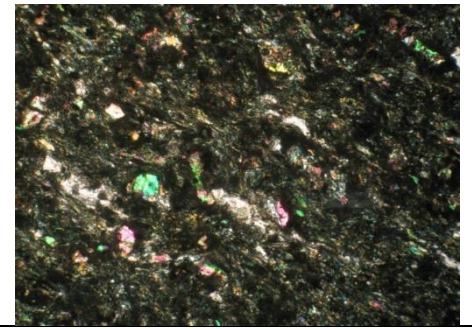
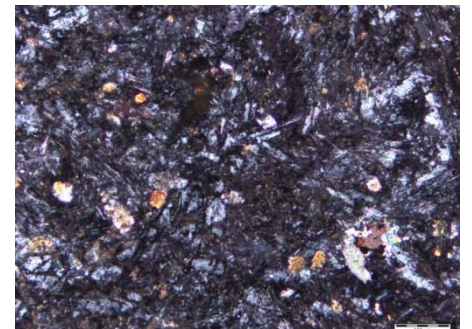
G12-013					
	30P	678818	1467063	Fine-grained basalt with 5 % subhedral plagioclase (0.1-0.4 mm), 5 % altered clinopyroxene (0.2 mm), chlorite-epidote groundmass, amygdales filled with zeolite crystals.	
G12-018					
	30P	675652	1466804	Amygdaloidal, plagioclase-phyric (10%), clinopyroxene-poor, fine-grained basalt with chlorite-epidote groundmass and minor secondary quartz.	
G12-021					
	30P	695837	1459138	Amygdaloidal, fine-grained, aphyric with chlorite-epidote groundmass and plagioclase microlites.	

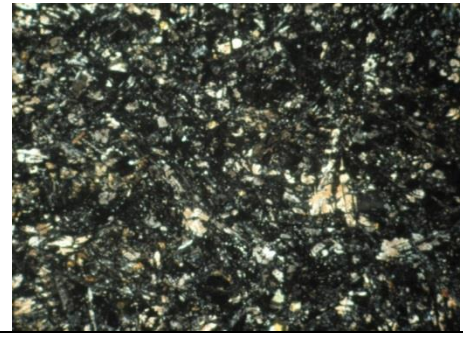
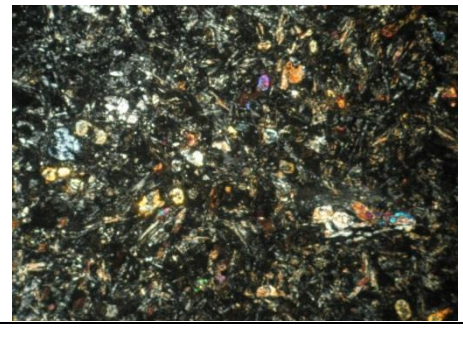
G12-02-003					
	30P	703585	1426248	Amygdaloidal, very fine-grained basalt with aphyric and aphanitic textures.	
G12-02-018					
	30P	712352	1431991	Very fine-grained, aphyric basalt with epidote and chlorite rich groundmass, and clinopyroxene microlites (fibrous texture).	
G12-02-020					
	30P	712916	1431713		

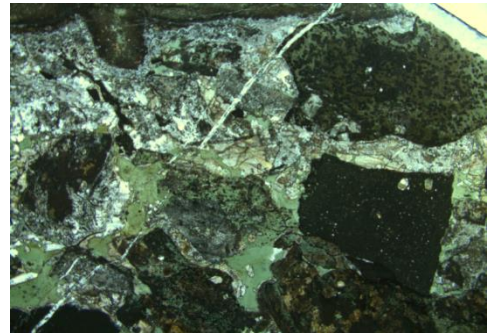
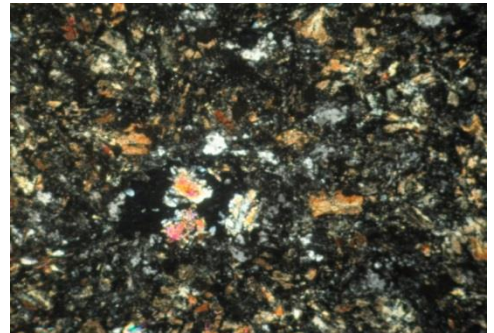
G12-02-022					
	30P	713245	1431519	Amygdaloidal, fine-grained basalt with 1-2 % clinopyroxene (<0.3 mm) dominated by chlorite and epidote.	
G12-02-026					
	30P	706792	1423420	Fine-grained basalt; 0.1 - 0.4 mm plagioclase-phyric (<5%), fibrous (altered) clinopyroxene microlites.	
G12-02-030					
	30P	702957	1423554	Amygdaloidal, hyaloclastic, porphyritic basalt with subhedral-euhedral plagioclase up to 1 mm, groundmass very fine-grained.	

G12-02-047					
	30P	700412	1430174	Amygdaloidal, hyaloclastic textures present in fine-grained basalt. Aphyric and aphanitic textures with chlorite-epidote as groundmass also evident.	
G12-02-053					
	30P	699504	1430061	Plagioclase microlite (~5 %), chlorite-filled amygdales, chlorite-epidote dominant, epidote occurs as crystal laths.	
G12-02-057					
	30P	699990	1435556	Hyaloclastic brecciation (jig-saw fit), amygdaloidal (infilled with epidote and zeolites), aphyric basalt with fine-grained epidote-chlorite as groundmass.	

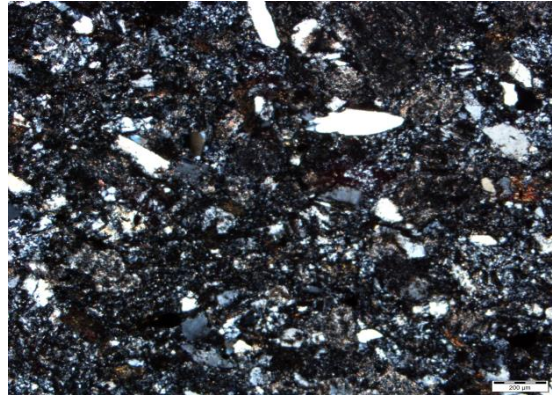
G12-02-060					
	30P	699558	1435266	Amygdaloidal basalt, heavily altered, epidote-chlorite dominant, amygdales filled with epidote, zeolite and quartz, quartz veins cross-cutting.	
G12-02-062					
	30P	698384	1434809	Plagioclase-phyric (< 5%), fine-grained basalt with a groundmass dominated by chlorite-epidote, clinopyroxene and plagioclase microlites.	
G12-02-068					
	30P	705632	1442485	Fine-grained, aphyric and aphanitic basalt, calcite-epidote-quartz filled amygdales, 30 % oxides.	

G12-02-085					
	30P	703421	1445760	Amygdaloidal, fine-grained basalt with plagioclase and clinopyroxene microlites, aphyric and aphanitic texture, chlorite-epidote in groundmass.	
G12-02-090					
	30P	702641	1445482	Chlorite-epidote crystal laths, secondary calcite veins and minor actinolite, foliated, no primary mineralogy visible.	
G12-02-095					
	30P	695421	1443258	Fine-grained, plagioclase-phyric (0.1-0.3 mm) basalt, chloritised glass, amygdaloidal, chlorite-epidote groundmass.	

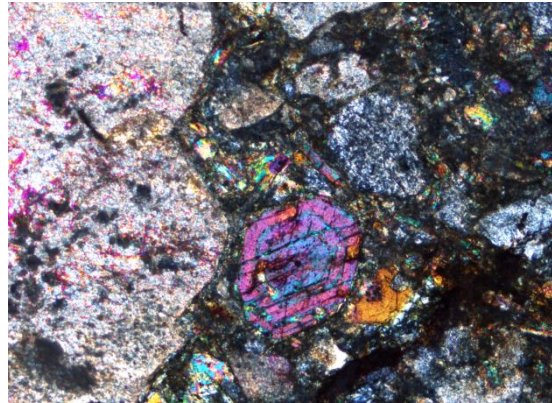
G12-02-096					
	30P	694686	1443104	Fine-grained, clinopyroxene-phyric (< 5 %) amygdaloidal basalt with chloritised glass and plagioclase, epidote and chlorite in the groundmass.	
G12-02-097					
	30P	694393	1442727	Fine-grained basalt with aphyric and aphanitic textures and plagioclase-clinopyroxene-epidote-chlorite making up groundmass.	
G12-02-098					
	30P	693240	1443462	Very fine-grained basalt with chloritised groundmass. Sample contains < 6 % plagioclase and clinopyroxene phenocrysts (<0.5 mm).	

G12-02-099					
	30P	696917	1441719	Basalt that is fine-grained, aphyric, amygdaloidal and contains hyaloclastic textures (jig-saw fit) with chloritised glass and chlorite, actinolite, epidote, calcite and quartz infilling vesicles and hyaloclastic fractures (Scale = 11 mm)	
G12-02-104				Fine-grained basalt with aphyric and aphanitic textures. Chlorite-epidote groundmass. Chloritised glass and amygdales.	
	30P	695831	1441613		

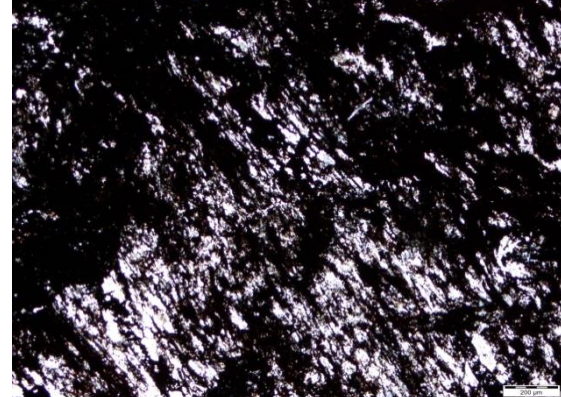
**Volcaniclastic
deposits**

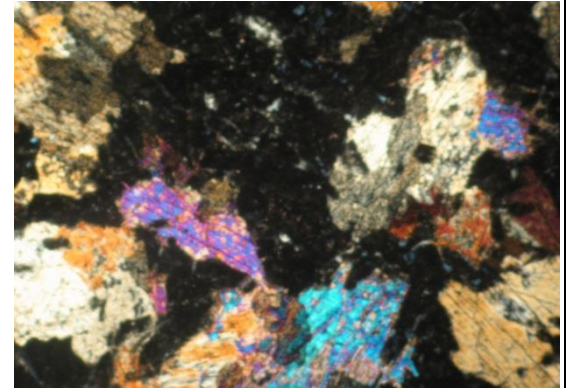
G12-007				Poorly sorted, contains quartz, subhedral plagioclase, chlorite, clinopyroxene, chert, clinopyroxene, muscovite. The matrix is composed of polycrystalline quartz, chert and chlorite and most grains are sub-angular --> sub-rounded (0.1 - 4 mm). There is greater than 20 % matrix.	 A photomicrograph showing a dark, granular matrix with numerous light-colored, angular mineral grains. A scale bar in the bottom right corner indicates 200 micrometers.
	30P	696828	1443986		

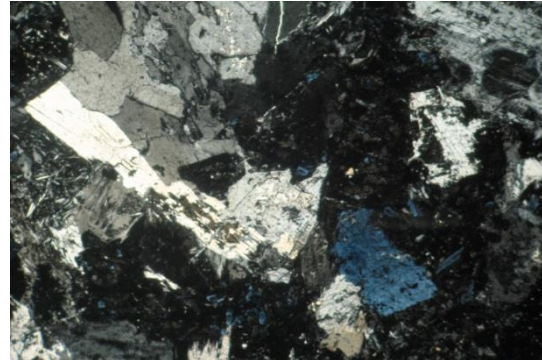
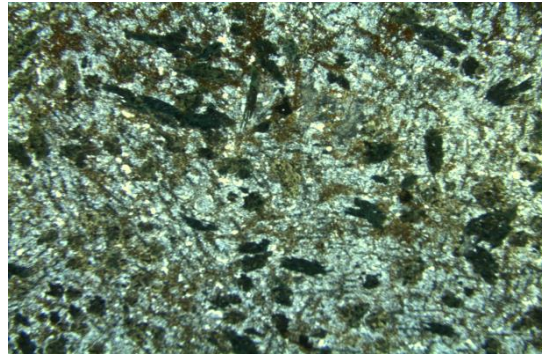
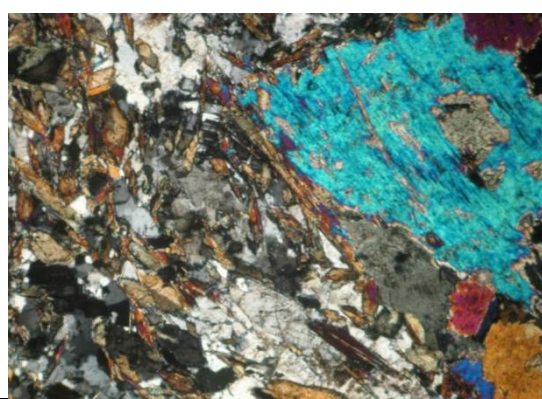
**Pyroclastic
agglomerate**

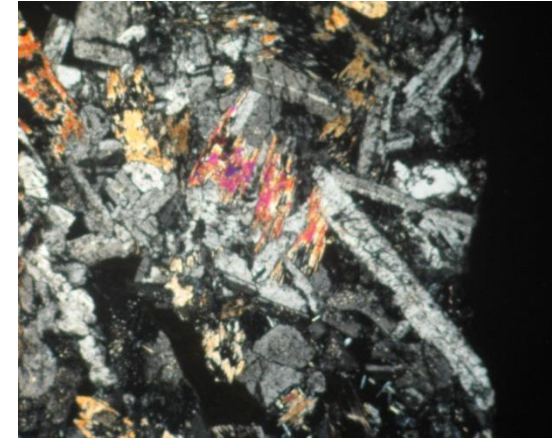
G12-02-126				Poorly sorted array of minerals including zoned, euhedral volcanic hornblende, 2-6 mm euhedral plagioclase, subangular-subrounded quartz grains, chert grains, chlorite, epidote, and matrix consists of fine-grained, angular minerals.	 A photomicrograph showing a variety of mineral grains, including a prominent pinkish-purple hornblende crystal with internal zoning. Other visible minerals include plagioclase, quartz, chert, and chlorite, set against a dark, fine-grained matrix.
	30P	709365	1424791		

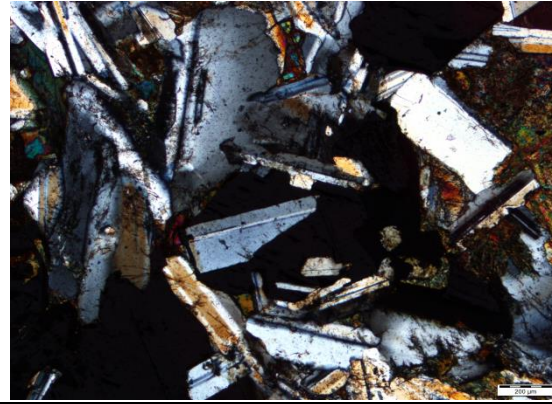
Exhalite units

G12-006	30P	702344	1446021	Fine-grained, with polycrystalline quartz and haematite (Fe-rich) with secondary hematisation. Deformed.	
G12-017	30P	677996	146647	Fine-grained, with quartz stockwork veins-brecciated. Ilmenite and hematite veins present.	

G12-02-015					
	30P	711629	1431822	Fine-grained haematite and secondary quartz; Fe-rich sample	
Dykes					
G12-02-008				Large clinopyroxene, orthopyroxene (2-4 mm) and less plagioclase (1-4 mm) crystals, exsolution within in pyroxenes (Scale = 1 mm)	
	30P	709181	1428595		

G12-02-009					
	30P	709452	1428840	Coarse-grained (1-4 mm) plagioclase-rich (40 %) rock with hornblende (5%), chlorite and orthopyroxene (4 %) (Scale = 1 mm)	
G12-02-011				1-2 mm, altered hornblende and subhedral plagioclase crystals, groundmass composed of fine-grained interstitial quartz , 0.1-0.3 mm blades of actinolite, 0.3 -0.7 mm epidote and chlorite crystals (Scale = 11 mm)	
G12-02-017				Coarse-grained rock with 30 % subhedral to euhedral plagioclase, 20 % clinopyroxene and 30% hornblende. Crystal sizes vary from 2-4 mm	
	30P	712130	1431987		

G12-02-036					
	30P	707539	1425072	Coarse-grained, plagioclase-clinopyroxene-hornblende-orthopyroxene bearing dyke with exsolution of K-feldspar in plagioclase crystals	
G12-02-048					
	30P	699650	1429026	Coarse-grained plagioclase-muscovite-hornblende-clinopyroxene dyke	

G12-02-114					
	30P	711540	1432977	Quartz, biotite plagioclase, microcline, muscovite, orthoclase- medium-grained. Has poikilitic and myrmekitic textures and exsolution in feldspars	
G12-02-122				Coarse-grained, plagioclase-clinopyroxene-orthopyroxene-biotite bearing dyke and 3-5% disseminated sulfides.	

G12-02-130				
30P	709295	1427484	Muscovite-hornblende-chlorite-sericite bearing, coarsely crystalline rock. High level of alteration.	